A mechanistic dynamic simulation for predicting the bottom of the line corrosion rate of mild steel in metal mine effluent and synthetic seawater flow

---

(full dissertation)

by

Matsobane Phillip Mothiba (200826157)

A dissertation submitted in fulfilment of the requirements for the
Magister Technologiae Degree

in

Engineering Metallurgy

Faculty of Engineering and the Built Environment

at the

UNIVERSITY OF JOHANNESBURG

SUPERVISOR: Mr GA Combrink
CO-SUPERVISORS: Prof ME Makhatha
Mr GM Tseounyane

June 2020

DISSERTATION GENERIC STRUCTURE

Prefatory parts

Chapter 1: Introduction to the study

Chapter 2: Literature Review

Chapter 3: Research Methodology

Chapter 4: Pre-and Post-Test Assessment

Chapter 5: Spectroscopic Characterization

Chapter 6: Electrochemical Evaluation

Chapter 7: Conclusions & Recommendations

Chapter 8: References

Appendix A

Appendix B

DEDICATION

I dedicate this dissertation in memory of the below heroes/heroines, whom I carry in my heart wherever I go:

- Lesiba Ernest Mothiba – My Father
- Renny Tlou Ledwaba - My Nanny
- Macula Sethoga – My Niece
- Freddy Tselani Modiba – A Friend

DECLARATION

I Matsobane Phillip Mothiba with this statement affirms that this research work is my own, and to my knowledge has not been submitted anywhere else for academic credit. I understand what plagiarism implies and declare that this proposal is my ideas, words, phrase, arguments, graphics, figures, results and organization except where reference is explicitly made to another's work. I understand further that any unethical academic behaviour, which includes plagiarism, is seen in a serious light by the University of Johannesburg and is punishable by disciplinary action.

Signed…… ……..... Date… 25/06/2020……

Table of Contents

ACKNOWLEDGEMENTS

Romans 11: 36 – "*For from Him and through Him and to Him are all things. To Him, be the glory forever! Amen*." Thank you, Lord, for surrounding me with greater minds for the accomplishment of my dissertation.

- To my supervisor, Mr G.A. Combrink, thank you for awarding me the opportunity to study under your guidance and for guiding me through the many obstacles during this study. Especially for affording me the freedom to run with this project.

- My gratitude goes to Mr M.C. Ramulongo for dedicating his time in helping me design and build the test-rig. Your enduring friendship means so much to me, and your support made this journey enjoyable.

- I would like to express my appreciation to my advisor Dr O. Ige, who laid the foundation for my study by handing me my first study material related to my master's topic, and for always availing himself for me to consult.

- My most sincere appreciation goes to (soon to be Dr) G.M Tsoeunyane, who has been a true mentor for me all these years. I certainly owe much of my professional and academic development to his guidance, unwavering encouragements and his inspiring examples.

- I am also grateful to Prof M.E. Makhatha and Prof P.A. Olubambi who always followed my progress with sincere interest and care and from whom I benefited greatly.

- Great thanks go to the Extraction Metallurgy Assay Laboratories team, namely Ms N. Baloyi, (and soon to be Dr.) E.M. Ntumba and K.J. Nyembwe from whom I also benefitted immensely from their outstanding qualities.

- I am very grateful to my parents M.M and L.E. Mothiba, my siblings L.P. and M.A. Mothiba for their firm support and keeping me resolute to complete the tasks entrusted to me.

- Finally, I would never have made it anywhere without the love and unconditional support of my life partner Z. Mdluli, and the joy of having such a beautiful family. To our boy: Take your time. Do it right. And enjoy. That is the best advice I can give you.

ABSTRACT

This study was structured on the uncertainty of events that comes with internal pipe corrosion. Hitherto, the study of corrosion was structured on the combined effect of electrochemical activities (chemical dissolution) and flow properties (hydrodynamics) being the main parameter controlling the physical characteristics by forming semi-permeability or partial protective corrosion product barrier between the steel surface and the flowing MME/SSW solution.

To disseminate the knowledge and raise the level of understanding, a multi specimen electrochemical test-rig prototype was developed to study the corrosion behaviour of mild steel in mine effluent (MME) and synthetic seawater (SSW). The electrochemical impedance spectroscopy (EIS) data showed the SSW corrosion-product charge transfer resistance (R_2) decreased from 18597 Ohm to 3.367 Ohm with flow rate. The lower the charge transfer resistance indicates a high mild steel dissolution rate. Hence, a decrease in charge transfer (R_3) with exposure time. The MME experiments were marked by a low charge transfer resistance (R_3), hence the high corrosion rate (CR). The (a) factor indicated the permeability of the multi-layered corrosion film, thus, whether or not the multi-layer film behaved like a capacitor. The behaviour was supported by the constant phase element (Q_3) which increased with CR.

The potentiodynamic polarization (PDP) results show that the corrosion current density (i_{corr}) increased with flow velocity which thickened the boundary layer, resulting in a high concentration of the reactant at the surface. The i_{corr} for mild steel in MME solution was higher than the limiting current density (i_{lim}) which indicates that the corrosion mechanism was controlled by diffusion. Such corrosion mechanism marked by a high corrosion potential (E_{corr}) which prevents scaling. Hence, the high corrosion rate (CR). For mild steel in SSW, the corrosion mechanism was controlled by activation of the reaction. Hence, the cathodic limiting current density β_c declined with exposure time and flow rate during flow accelerated corrosion (FAC). This behaviour resulted in a decrease in CR due to the ferrous ion (Fe^{2+}) quickly been saturated by the corrosive SSW solution, which leads to a pH decrease.

Both the PDP and EIS data showed that the SSW environment was conducive for a firm scale formation, as evidence of a decreasing CR from 13.397 mpy to 1.438 mpy with exposure time was observed. On the other hand, the effect of hydromechanics such as high hydrostatic pressure, flow rate and high axial stress (S_L) interrupted the development of corrosion product in some sampling sites, which lead to a high CR of 183.947 mpy. In conclusion, the study shows that the rate of metal loss inside a pipeline depends on the science and behaviour of corrosion product on the surface. With the presence of a multi-layered corrosion film reducing the corrosion rate (CR) by forming a barrier between the steel surface and electrolyte. The MME corrosion rate (CR) was catastrophic, which disintegrated the entry coupon samples sometimes after 24 hours. Hydromechanics and mass-transfer parameters were used to elucidate the behaviour of multi-layer film during this study.

List of Figures

List of Tables

List of Abbreviations

BLC	Bottom of the Line Corrosion
DO	Dissolved Oxygen
E/CRC	Erosion/Corrosion Research Center
EDX	Energy-Dispersive X-ray Spectroscopy
FAC	Flow Accelerated Corrosion
ICMT	Institute for Corrosion and Multiphase Flow Technology at Ohio University
MME	Metal Mine Effluent
MPY	Corrosion Rate Mils per year
CorrISA	Corrosion Institute of Southern Africa
PFL	Pipeline Flow Loop
PSS	Pseudo-Steady-State
SEM	Scanning Electron Microscope
SSW	Synthetic Seawater
TLC	Top of the Line Corrosion
XRD	X-Ray Diffractometer

CHAPTER ONE
INTRODUCTION TO THE STUDY

1.1. Introduction

This introductory chapter provides the motives for this study, together with an overview of the research. The section starts by presenting the context within which this study was conducted—then followed by the problem statement, the research goal and objectives established to achieve the experimental purpose.

This study presents a principal outcome from both qualitative and quantitative research when metal mine effluent (MME) and 36 ppt synthetic seawater (SSW) bulk solution was respectively recirculated inside a rectangular duct for 24-and 192-hours. Thus, the study uses a real-time approach to model flow-induced corrosion (FIC) and mechanically assisted degradation, including the prismatic crystal scale formation during flow loop. The work presented here discusses the efforts in the development of a mechanistic model, supported by experimental investigations.

Because of a potential difference, all metals behave uniquely when they are exposed to a corrosive environment. Considering that polarization curves are a popular technique used to study electrochemical behaviour. A multi specimen electrochemical test-rigs prototype (unit) was installed to the Bio-Logic ASA Potentiostat Electrochemical analyzer model SP-150 in the appropriate position(s) to monitor the electrochemical behaviour of the test specimen in a specific environment. Flow parameters (flow velocity, mass transfer control, hydromechanical load, erosion-corrosion synergy and flow configuration) and exposure time were used to substantiate the potentiodynamic polarization (PDP) and electrochemical impedance spectroscopy (EIS) behaviour during this study.

FIC is a multifaceted phenomenon governed by three simultaneous processes; charge-mass transport and electrochemistry (Wang, 2002; Nesic & Sun, 2009). Under the flow-non-sensitive condition, oxygen absorption activates a pseudo-passive scale film on the surface. The significance of scaling is that the corrosion film provides marginal

protection, which lowers CR by polarizing the surface. Thus, forming a capacitor (electrical resistant) between the electrolyte (cathode) and the steel coupon (anode) (Nešić, 2007). In contrast, scaling is controlled through hydrogen hydrolysis during flow-sensitive conditions. Therefore, the formation of the limited corrosion product layer is interrupted by the transfer rate of hydrogen ions ($H^+ -$ from the electrolyte) to the substrate, and the transfer rate of ferrous ions ($Fe^{2+} -$ from the substrate) to the electrolyte (Nesic, 2012). The limited corrosion film is further weakened by a rigorous kinetic interaction between $H^+ - Fe^{2+}$ on the steel-electrolyte interface, and hydrodynamic stresses (Shannon & Ross, 1964), that led to the formation of a weak porous corrosion film which can be eroded by bulk flow (Dugstad, 1998; Pienaar, 2004). Because corrosion mechanism is governed by high charge transfer, with little to no mass-transfer resistance, in a film-free condition, CR is expected to be proportional to flow velocity (Dugstad, et al., 1994).

1.2. Context of the Study

The context of the following section includes an academic rationale and gaps that exist in the open literature concerning flow-induced corrosion (FIC). The discussion of the educational context provides some insight into the work conducted by Institute for Corrosion and Multiphase Flow Technology at Ohio University (ICMT) and the Erosion/Corrosion Research Center (E/CRC) of the University of Tulsa, the world-leading expects in modelling flow-induced corrosion. In line with the research method and the experimental objectives, the academic rationale provides the motivation that led to the inception of this study.

1.2.1. Academic Rationale

Pipeline transmission and distribution systems are the most used method to transport a large volume of Newtonian and non-Newtonian fluids (NaturalGas.org, 2013). To fulfil market demands, the transmission spans from a few meters to thousands of kilometres, such as the (Husseini, 2018)…

- A west-East gas pipeline operated by PetroChina which traverses 8 7070 km to connect 66 cities in ten Chinese provinces form the Tarim Basin gas fields in Xianjing to Shanghai,

- The Gasbol pipeline which travels 4 989 km connecting Bolivia's reserves in Rio Grande to Mato Grosso do Sul in central Brazil, Maranhao in central Brazil and Porto Alegre on Brazil's south-east coast, or

- The 4 857 km Eastern Siberia-Pacific Ocean Oil Pipeline (ESPOOP) which transport crude oil from Taishet in Irkutsk (Siberia) through Kozmino to Skovorodino near the north Chinese border.

Looping to contend with thermal expansion/contractions and other mechanical forces that can affect pipelines. Using corrosion resistant alloys (CRAs) for the construction of such volume will be an expensive exercise. Whilst the usage of polyvinyl chloride (PVC) pipes are mostly limited by operational anomalies such as creep and hydrodynamic stresses. Carbon steels and stainless steel have over the years became the primary materials of choice in pipeline transmission construction (Martins & Freire, 2009; Mahmoodian, 2018). The behaviour of the stainless-steel corrosion mechanism is out of the scope of this study, and as such will not be discussed. The popularity of low carbon steel such as mild steel came from the materials ability to meet satisfactory mechanical specifications at an economical cost (DPI Plastics, 2013). However, the integrity of metallic pipeline transmissions is often damaged by internal corrosion attack.

Since the drilling and completion of the first mine shaft operations in South Africa, the mining industry had to battle with such corrosion attacks (Andrew, 2013). And considering the discrepancy of internal corrosion mechanism (such as general corrosion, localized corrosion, microbiologically influenced corrosion (MIC) and mechanically assisted corrosion), there is a physicochemical and mechanical need to understand and define the distinctive occurrence and mechanism; - to counteract the corrosion-related attacks. The bottom of the line corrosion (BLC) is progressively

recognized by (Li, et al., 2011; Addis, et al., 2008; Nesic & Sun, 2009) to be the most common aggressive internal corrosion form which results in pipe failure.

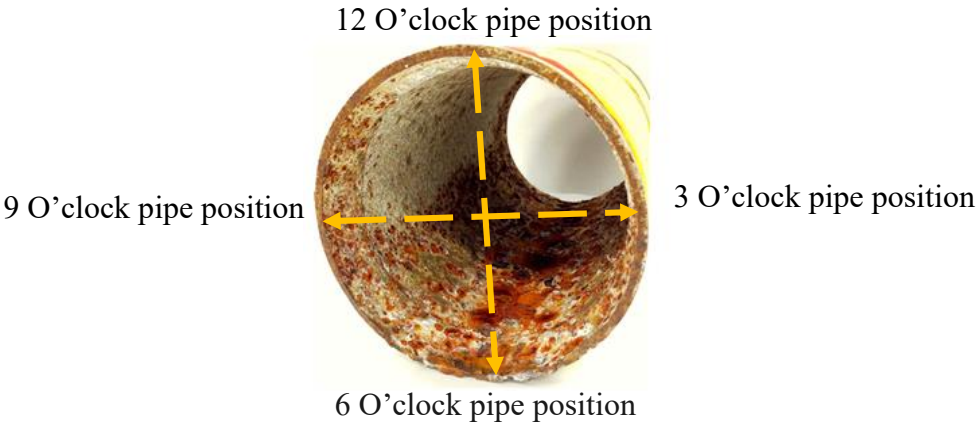

Figure 1: Pipe section showing the bottom of the line corrosion (BLC) at 6 o'clock pipe position, (United Fire Protection, 2020).

BLC is a slow piping degradation mechanism triggered by thinning or damaging of the corrosion product when MME/SSW bulk flow streams at 6 o'clock pipe position, the effects of such mechanism is demonstrated in Figure 1. FIC process at the bottom of the pipe occurs when the charge-mass transfer rate is sufficiently high enough to deplete the reactant concentration at the metal surface (Nesic, et al., 1995). With the mass-transfer controlling the flow-non-sensitive condition and charge transfer controlling the flow-sensitive conditions. According to Li, et al., (2011) and Brown, et al., (2013), BLC poses a significant stochastic threat, once initiated, pitting propagates at a much higher rate than uniform corrosion.

Because of the high charge-mass transfer, the corrosion product ($FeCO_3$, FeO(OH), Fe_2O_3, FeS, and FeS_2) experiences a pH build-up. This limiting effect generates a pseudo-passivation film (polarize the surface) and results in increased surface potential (depolarization). Conversely, lower potential leads to a high CR because the corrosion product film loses its ability to protect the steel, and thus, promoting a galvanic cell effect, between the multi-layer film and the bare surface. The growth of the corrosion film strongly depends on the rate at which ferrous ions (Fe^{2+}) are released from the steel surface, with, pits most-likely to propagate in a semi-permeable corrosion scale environment. Scaling (or corrosion product layer with weak adhesion properties) will

form on the steel surface when Fe^{2+} ion concentration and H_2S concentration in the MME and/or H_2CO_3 concentration in the SSW exceeds the super-saturation level at the surface. During scaling, there is an increase in the cathodic limiting current density to a critical current density where the corrosion current density is reduced (Scully, 2003).

The micromechanical component is termed as erosion, where the protective corrosion film may be mechanically eroded because of wear and chemical dissolution from the bulk flow (Sundar, 1987). Mitred bends are the most commonly used geometry for redirecting flow in piping systems (Mazumder, 2004). Erosion is often inevitable at mitred curves (curvature and deflection angle) because of secondary flow (distortion flow) which influences the formation of surface pipe vortices (separate stream) when fluids flow through the inner convex pipe (Jianfu & Gabriel, 2004). Metal loss because of erosion and corrosion is more significant because of the synergistic effect, a phenomenon that occurs when erosion and corrosion attack simultaneously (Neville, et al., 1995).

Ellison & Wen (1981) argued that erosion-corrosion is most severe in two or multiphase flow systems, as compared to single-phase flow, where the hydrodynamic stresses are not large enough to erode the surface mechanically. Because during multiphase flow, the liquid drop can be spontaneously be brought to rest when hitting the surface, and as such resulting in high localized stresses at a point of contact.

1.2.2. Research Gaps

Equipment failures because of corrosion is a significant problem in the South African mining industry, coastal belts communities, chemical and power-generation industries, with pipes, valves, and fittings accounting for one of the highest expenditures on equipment and spares (CorrISA, 2019). Listed below are some ambiguities and gaps in the open literature regarding flow-induced corrosion (FIC) during flow loop.

1) Most experiments carried out to quantify erosion-corrosion synergism are performed using an apparatus in which the flow physics or hydrodynamics differ from reality (Watson, et al., 1995; Hubner & Leitel, 1996; Zhou, et al., 1996; Malka, et al., 2005).

2) Akin to the inception of localized corrosion in MME (H_2S)/SSW (H_2CO_3) solution, the propagation of localized corrosion is also poorly understood.

3) There is a lack of high-resolution in situ strategies to demonstrate the corrosion mechanism, and because corrosion dependence on the environment (system), ex situ measurements may suppress critical corrosion data or may misrepresent the records.

4) Modelling of $FeCO_3$, FeO(OH), Fe_2O_3, FeS, and FeS_2 multi-layer corrosion film is ambiguous. And there is no universal approach which works for all in situ flow conditions (Meng & Ludema, 1995).

1.3. Problem Statement

Corrosion is an indispensable surface-related degradation process (Nešić, 2007), and during pipe fluid flow, internal pipeline corrosion rate (CR) could be increased or decreased by formation or erosion of the corrosion film (Efird, 2000). Listed below are the challenges addressed by this study:

1. Globally, there is a limitation of large-scale testing facilities for researchers to study FIC. This study forms the groundwork to build such a facility.

    a) There is academic pressure to develop a mechanism that interprets sour (MME) and sweet (SSW) localized corrosion accurately to provide more accurate predictions of the likelihood of occurrence and the severity of the attack. Accurate corrosion results will help prevent corrosion attack at a minimal cost.

    b) One way in which the effects of flow velocity can be studied on a laboratory scale (ex-situ) is to use a flow loop to simulate real-life conditions (in situ). Unfortunately, such a system is cumbersome to install and impracticable to operate, especially for the rapid determination of CR by electrochemical techniques.

2. Although accurate, most studies are limited to the stagnant setting, jet impingement and rotational motion, and, such corrosion monitor devices cannot produce the realistic flow physics to simulate corrosion during single or/and multiphase flow conditions.

3. Pipe flow, similar to other duct flow, is linear steady at all Reynolds numbers (Tatsumi & Yoshimura, 1990). Despite extensive research, laminar pipe flow is still a topic that needs investigation, especially during corrosion attack when laminar pipe flow experiences marginal turbulence.

4. There is an inconsistency in data and, most available flow loop literature does not agree with existing analytical and numerical studies.

1.4. Research Goal

The goal of this study, which is inclusive of the novelty is to develop a mechanistic model to study the evolution of corrosion film (to predict corrosion rate (CR)) during pipeline flow loop (PFL). The used model depends on the principles of fluid mechanics, single-and-multiphase flow theories, and physical mechanisms that cause FIC. Thus, the results obtained from the mechanistic model can test, predict and study the effect of multiple parameters that influence erosion-corrosion synergy, impingement corrosion (direct, random and shear) and flow accelerated corrosion (FAC).

1.5. The objectives of the study

The following objectives were outlined to explain the effect of the electrochemical parameter, dimensionless hydrodynamic parameters and charge-mass transfer dimensionless parameters governing the bottom-of-the-line corrosion rate (respectively, incepted by uniform and localized corrosion mechanism):

1. To fulfil the aim, electrochemical impedance spectroscopy (EIS) and potentiodynamic polarization curves (Tafel plot) will be used together with the

Eulerian technique and other corrosion model tactic to interpret and validate the CR during flow loop, Eulerian calculations are shown in Appendix A.

a) Model the competition between scale formation, scale growth, scale damage (scale porosity) and scale removal through a flow loop to predict charge-mass transfer rate as a function of flow parameter (including mass transfer constant, hydromechanical parameters and erosion-corrosion synergy) and exposure time.

b) Study the synergy between corrosion and erosion during loop flow under free pH (conditions were pH is not controlled); with an initial pH value of 1.920 for MME solution and 8.020 pH value for SSW solution.

2. Propose a new modelling approach that predicts localized corrosion attack at different positions (vertical and up -and -downslope inclination flow), akin, propose experimental set-ups for monitoring corrosion mechanism for Top-of-the-line corrosion (TLC) mechanism and sidewall corrosion phenomena.

CHAPTER TWO
LITERATURE REVIEW

2.1. Introduction

This chapter presents the literature survey relevant to this study. The following topic is based on previous reviews to support the experimental work aimed to develop a complete understanding of real-time events of flow-induced BLC mechanism under different hydrodynamics and mechanical (streamline) conditions. The topics exploring existing gaps are structured as follows:

- Corrosion Models
- Hydrodynamics (Newtonian fluid behaviour, flow regime, and flow patterns)
- Corrosion Science (inclusive to corrosion mechanism, erosion mechanism, and water chemistry)
- Background study concerning sour and sweet corrosion, (inclusive to the science of corrosion product layers)
- Electrochemistry (inclusive to electrochemical measurements and reactions, and charge-mass transfer characterization) with several titles and subtitles to further support the topics.

The first four topics (Section 2.2. to 2.5) are solemnly based on a technical point of view that corrosion cannot be characterized without classifying the material and the environment reacting with it (or the corrosive system). The last six topics (Section 2.6 to Section 2.11) is used to nudge pertinent literature to support this study.

2.2. Corrosion Models

Approximately all aqueous corrosion models in the literature are established on either the empirical, mechanistic or semi-empirical theoretical fundamentals (Nešić, et al., 1996). The following section describes the different method used to study the flow-

induced corrosion (FIC) mechanism, with Figure 2 demonstrating the different model approach.

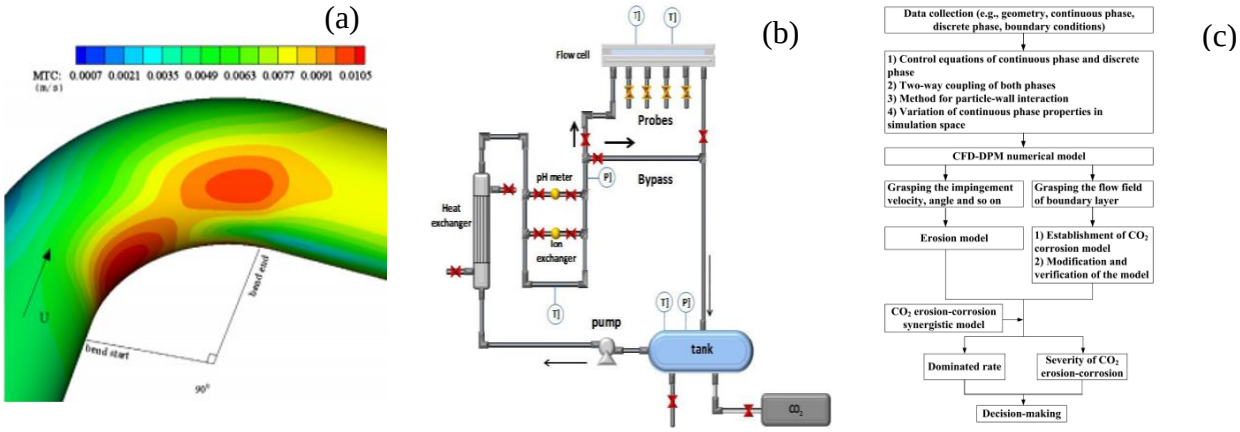

Figure 2: Schematic representation of (a) Empirical Model (Rani, et al., 2014), (b) Mechanistic Model (Farelas, et al., 2010), and (c) Semi-Empirical Model (Zhao, et al., 2020).

2.2.1. Empirical Models

An Empirical model is a simulation tool that does not follow the physicochemical rudiments. Such models are primarily founded on experimental curve-fitting data (Nešić, et al., 1996) or artificial neural network (ANN) proficient at generating basic non-linear multiple parameters governing FIC (Nesic & Vrhovac, 1999). Computational fluid dynamic (CFD) is a typical example of Empirical approach.

2.2.2. Mechanistic Models

The mechanistic approach is founded on the physicochemical interpretation of corrosion mechanism (which is inclusive to the corrosive system), water chemistry, electrochemistry and charge-mass transfer between the metal surface and solution (Nesic, et al., 1997). Where, the incorporated sub-model (migration due to the potential field, diffusion due to the concentration gradient, and convection by the flow) can independently be modified to accommodate corrosion evolution. The models exercises' Henry's law coefficient, Schmidt number (Sc) and mass-transfer coefficient to decipher and elucidate the physical corrosion mechanisms parameters. In this study, a parametric evaluation is developed to mimic the Helmholtz model for flow-induced

bottom-line corrosion (BLC), inside a rectangular duct tube, with coupon samples position at strategic locations. This approach deciphers and elucidates key influencing factor, together with the corrosion rate-determining step which governs both uniform and internal localized corrosion, including hydrostatic pressure, charge-mass transfer, electrochemical reactions, scale formation (depending on the electrolyte-MME/SSW) and pit evolution, by respectively streaming MME/SSW bulk solution over the test specimen for 24-and 192-hours at different velocities (0.062 m/s, 0.018 m/s, 0.116 m/s and 0.107 m/s).

- Henry's law coefficient is the proportional factor of dissolved gas and their partial pressure. Gaseous phase is out of the scope of this study.

- Sc is a shear component ratio of kinematic viscosity (momentum diffusivity) and mass diffusivity (density), used to characterize aqueous flow by associating the thick layers of the hydrodynamic and mass-transfer boundary.

- Helmholtz approach is a study of the charge build-up between the working electrode (steel) – and – MME/SSW electrolyte interface when they are in contact. In this study, the MME solution is used to study the micro-galvanic cell activities between the formed weak corrosion film islands and the bare surfaces. According to Eldik & Palme (1982), electrolyte with low pH value (acidic solutions) favours hydrogen hydrolysis, which becomes the driving force during corrosion. Solution with high pH value such as SSW solution favours oxidation absorption. And is the other electrolyte used in this study to investigate charge-transfer interaction suspected to activate cathodic charge density from the mass-transfer rate (Wang, 2002; Nesic & Sun, 2009). Such behaviour is triggered by the formation of a pseudo-passive film which acts as a capacitor by lessens E_{corr} and I_{corr} at the steel-electrolyte interface (Behpour, et al., 2009).

2.2.3. Semi-Empirical Model

The semi-empirical approach links-up the proficiencies of empirical - and mechanistic - models. The deteriorations of preliminary information or ANN approach are

interrelated to the mechanistic model when there is uncertainty regarding the erosion-corrosion mechanism.

2.3. Flow Pattern

"Since corrosion is a surface-related degradation process, flow can decrease or increase the corrosion rate (CR) by encouraging scaling or surface wear (Efird, 2000)". Under high flow rate and hydrostatic pressure, the flow will accelerate deterioration rate as flow erodes the corrosion film from the substrate (Nesic, et al., 1997). Under the flow-non-sensitivity condition, lengthy exposure time (immersion time) will trigger a build-up of an impermeable corrosion film which continues to lower CR as crevice and pitting corrosion propagates (Scully, 2003).

For a single-phase flow, there are two mechanisms by which flow increases the deterioration rate. Flow can accelerate the degree of mass-transport and/or erode the multi-layer film (Nesic & Sun, 2009). Quasi-steady flow, laminar flow and marginal turbulent flow are the three flow regimes investigated in this study.

2.3.1. Pseudo-Steady-State (PSS) Flow

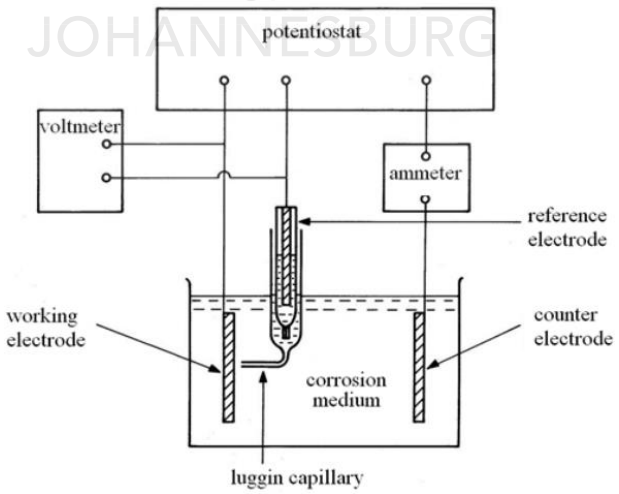

Figure 3: Schematic representation of Pseudo-steady-state (PSS) flow (Ogazi, et al., 2015)

"Pseudo-steady-state (PSS) flow or quasi-steady flow is a boundary-dominant flow regime observed when pressure waves spread to the boundary in a closed drainage area such as in a reservoir (Slider, 1966)". Thus, the pressure gradient during (PSS) flow regime becomes stable throughout the entire boundary system after a long period of drawdown dominated by transient flow (Collins, 1991). During this period, the declined pressure rate is approximately the same within the bounded system (Lu & Tiab, 2008 ; Lu & Tiab, 2009). Figure 3 demonstrate an example of PSS approach.

Based on Scully (2003), "Fick's first law for quasi-steady conditions outlines the flux (J) of the diffusion species ($\mathrm{mol/m^2 s}$) to be perpendicular to the boundary film in which the electrons diffusion through", as shown in Equation 1.

$$\mathrm{J} = \frac{\mathrm{i}}{\mathrm{nF}} = -\mathrm{D} \times \frac{\Delta \mathrm{C}}{\delta} \qquad \text{Equation 1}$$

Where, the symbol n signifies the magnitude of electrons exchanged in a reaction
F is the Faraday constant equalivent approximated to 96500 c/mol.
I is the current density ($\mathrm{A/m^2}$)
D is the transmission constant (diffusion coefficient) measured in $\mathrm{m^2/s}$
ΔC is the concentration gradient (driving force) between the substrate and the electrode measured in $\mathrm{mol/m^3}$, and,
δ is the transmission barrier layer measured in m.

The minus symbol indicates that the charge-mass transfer transmission occurs from a high to low concentration. Equation 2 below shows the concentration gradient between the substrate and the electrode:

$$\Delta \mathrm{C} = \mathrm{C_b} - \mathrm{C_S} \qquad \text{Equation 2}$$

Where, symbol $\mathrm{C_b}$, indicates the bulk concentration measured in $\mathrm{mol/m^3}$
$\mathrm{C_s}$ is the substrate concentration measured in $\mathrm{mol/m^3}$

2.3.2. Single-Phase Flow (Laminar Flow)

The laminar flow regime is characterized by well-defined linear paths of fluid particles smoothly glide in a streamlined manner without mixing (Gavrilakis, 1992; Van Sittert, 1999). In this flow regime, "the viscous force dominates, and shear stress is proportional to the change in flow resistance" (Haldenwang, et al., 2010; Chhabra & Richardson, 1999; Shoham, 2006). Figure 4 shows a schematic representation of a laminar flow regime. And by applying a boundary condition where velocity is zero at the substrate surface, one can integrate into the Hagen-Poiseuille equation to obtain speed at any point in the duct (Hewitt, 2005), as shown in Equation 3.

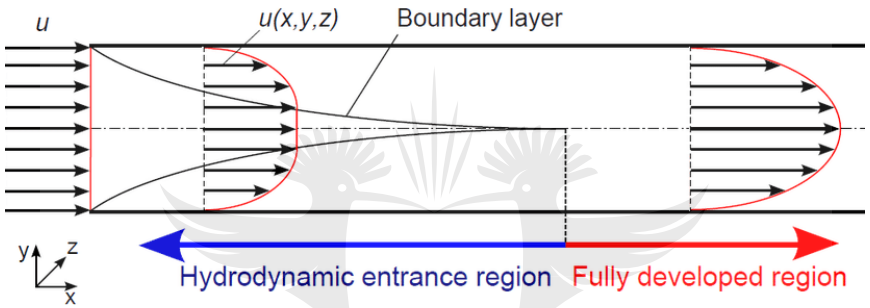

Figure 4: "Development of laminar flow regime in a duct (Briano, et al., 2012)", as cited from (Ruthemann, 2011).

$$Q = \frac{\pi R^4}{32\mu}\left(\frac{\Delta p}{L}\right) \qquad \text{Equation 3}$$

Where, Q is the volumetric flow rate having a SI unit of m^3/s

R is the pipe radius measured in m

μ is the dynamic viscosity measured in g/ms

ΔP is the pressure difference between the two ends, with a SI unit of g/ms^2

L is the pipe length measured in m

Moreover, the average velocity (v) can be expressed using a volumetric flow rate (Q) and area (A) as shown in Equation 4.

$$V = \frac{Q}{A} \qquad \text{Equation 4}$$

The velocity profile (u) is represented by Equation 5 and Equation 6:

$$u = u_{max}\left(1 - \left(\frac{r}{R}\right)^2\right) \qquad \text{Equation 5}$$

$$\therefore \quad U_{max} = \frac{\Delta P R^2}{4\eta \Delta X} \qquad \text{Equation 6}$$

Where, $\boldsymbol{\eta}$ is the viscosity measured in m^2/s

ΔX is the change in distance measured in m

U_{max} is the maximum velocity having SI unit of m^2/s

r is the diameter measured in m

2.4. Corrosion Mechanism Associated with Flow Loop

The corrosion is defined as the process by which electrochemical (or chemical) actions deteriorate the material facet (Combrink, 1995). Benabdellah, et al., (2010) has deciphered the corrosion reaction to be the overall atomic interaction of anodic oxidation and cathodic reduction. For anodic reaction, the dissociation of the substrate (steel) releases ions into the SSW electrolyte. Whilst the cathodic site discharges hydroxyl ions (OH^-) and dissolved oxygen (DO) from SSW solution (Misawa, et al., 1974). Consequently, the oxidation-reduction reaction from the electrochemical mechanism changes with the flow, and results in the formation of oxides, sulphide and carbonate corrosion film (Ts'oeuntane, et al., 2017; Krivenko, et al., November 2018; Xu, et al., 2016).

In a dynamic system like the one presented in this study, the corrosion rate (CR) depends on the charge-mass transfer processes, thus, both the electrochemical reaction and flow parameters. According to Ellison & Wen (1981) the mass transfer processes (convective-mass-transfer-control corrosion (CMTCC) and the phase-transfer-control corrosion (PTCC)) governs the CR. The CMTCC substantiates cases where CR is limited to the charge-mass transfer rate of the cathodic reactant, and the anodic products from the metallic substrate whereas PTCC refers to corrosion products caused by a dissolved corrosive solution.

2.4.1. Localized Corrosion

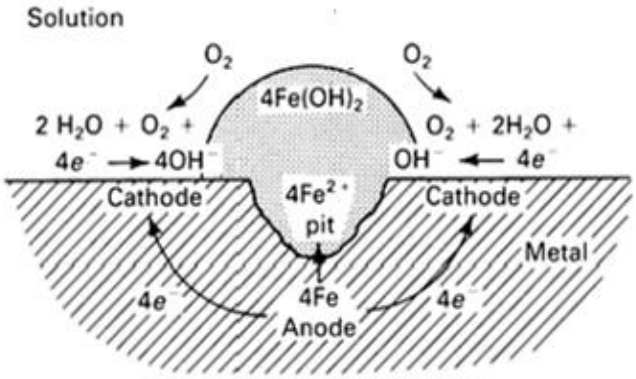

Figure 5: Schematic of pit initiation (Dexter, et al., 1991)

Localized corrosion usually results from a galvanic effect associated with a selective breakdown of a thin protective corrosion film; which makes certain areas corrode quicker than other regions, with pitting corrosion documented by Roberge (2008) as a typical localized corrosion mode. Pitting corrosion is a segregated mode of corrosion marked by rapid deterioration of the substrate in a restricted or local location. The inception of pitting emerges when there is a defect (weakness) within the protective corrosion product layer, permitting marginal regions on the bare surface to transfer ions such as Cl^- and SO_4^{2-} ions which lower the electrical resistivity of the corrosion cell (Gray, et al., 1990; Nešić, et al., 1996; Nešić, et al., 2001). The presence of a thin protective scale film is another parameter which increases the prospect of localized corrosion through a galvanic approach. The formation of a pit corrosion circuit is demonstrated in Figure 5 and described using Equation 7 to Equation 9.

As the pit propagates, the dissolution of iron (Fe) agrees with anodic reaction

$$Fe \rightarrow Fe^{2+} + 2e^- \qquad \text{Equation 7}$$

And the oxidation reaction is characterized by OH^- adjacent to the pit

$$O_2 + 2H_2O + 4e^- \rightarrow 4OH^- \qquad \text{Equation 8}$$

Equation 9 shows the insolubility of ferrous hydroxide ($Fe(OH)_2$) film

$$3Fe^{2+} + 6OH^- \rightarrow 3Fe(OH)_2 \qquad \text{Equation 9}$$

2.4.2. Flow Accelerated Corrosion (FAC)

Flow accelerated corrosion (FAC) often triggers wall thinning (metal thickness loss) of carbon steel pipelines. FAC is the predominant mode of pipe failure (Cubicciotti, 1988). With the propagation or coverage of oxidation film on the surfaces as the main factor used to characterize FAC mechanism (Villien, et al., 2001). The manner in which the material interacts with its environment (hydrodynamic conditions and environmental parameters) is another significant factor used to describe FAC mechanism. Figure 6 demonstrates the FAC mechanism in position 1. And to some ideological extend the impingement corrosion at position 3 and 4.

Where, the symbol V_1/V_2 represents the velocity (measured in m/s) at position 1, flowing toward position 2

P_1/P_2 represents the hydrostatic pressure measured in g/ms^2 and,

A_1/A_2 is the area measured in m^2 of the pipe at position 1 and toward position 2

An in-depth explanation of the test rig (including the derivation of hydrodynamics) and testing methodology are shown in Chapter Three. During FAC, ferrous ions (Fe^{2+}) are discharged into the bulk solution at the metal-electrolyte interface where some supersaturated Fe^{2+} ions react with other chemical species such as hydroxyl ions or dissolved oxygen to form that protective corrosion product film.

The thickness of the semi-passive corrosion product film is further affected by dissolved oxygen concentration (O_2) in the electrolyte-substrate boundary layer and is vital for oxidizing magnetite (Fe_3O_4) to hematite (Fe_2O_3), which has higher corrosion resistance (Lee, 2003; Wallis, 1969).

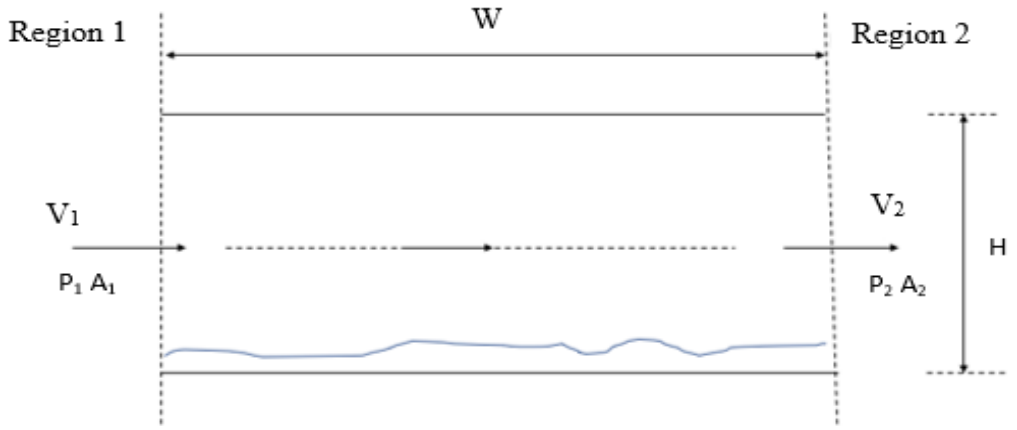

Figure 6: Random Impingement in a duct related to corrosion occurrence observed in position 1, 3 and position 4, source author

2.4.3. Erosion-Corrosion

As mentioned earlier erosion is defined as the mechanism through which materials are removed from a substrate through applied external mechanical forces. Tubing is found to be the primary sufferer of erosion related attack, especially in the vicinity involving high flow rate (Withers & Bhadeshia, 2001a). Erosion-corrosion is the corrosion mechanism studied in this work at position 2. This corrosion mechanism was also observed at all positions for MME studies and position 4 for 192H SSW studies, an explanation for such an occurrence is later given in detail in Chapter Six.

Erosion-corrosion is the interactive process involving erosion and corrosion during pipe flow. It occurs when the hydrodynamic stress mechanically erodes the metallic substrate (usually the protective corrosion product layer) in a corrosive environment, exposing the unprotected substrate vulnerable to accelerated electrochemical attack. Figure 7 shows a schematic of direct liquid impingement (DLI) at position 2.

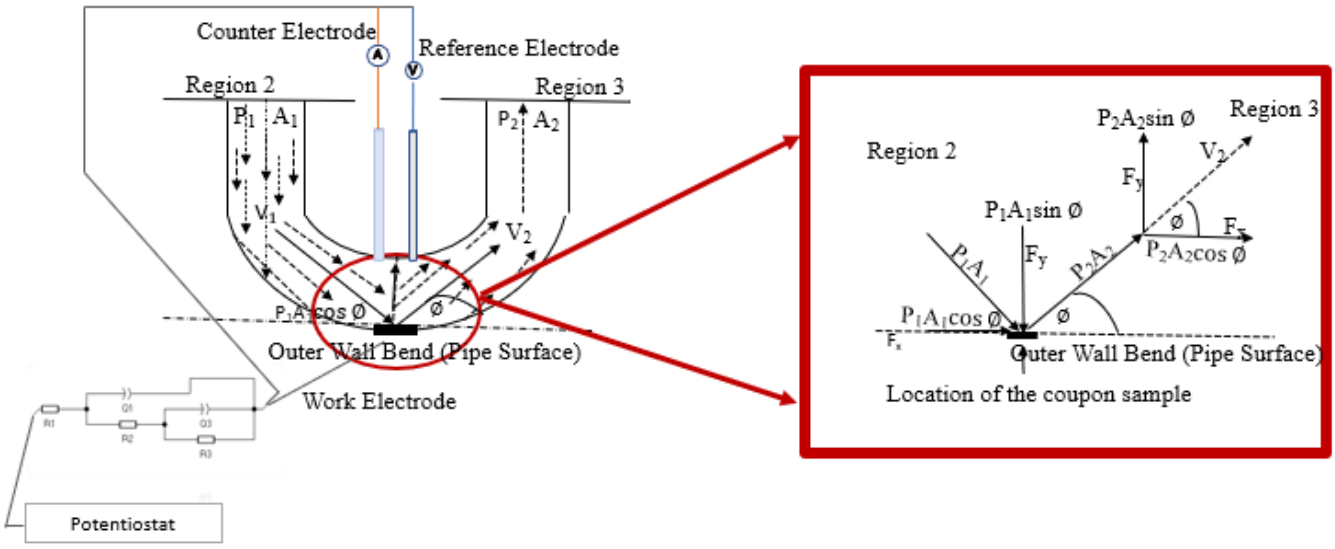

Figure 7: Schematic showing Direct Liquid Impingement at a **180**° return bend, source author.

2.4.4. Impingement Corrosion

Impingement corrosion is a weak form of erosion-corrosion which occurs when flowing liquid is above critical velocity and results in disruptive shear forces and abrupt pressure change on the pipe surface (Fontana & Green, 1978). Impingement corrosion thus, damages and wear away the corrosion product film on the surface, to produce a localized attack pattern i.e. deep grooves gullies, mesa, and material detachment (Copson, 1960). Because of the permeability of the corrosion film, the mechanism of impingement corrosion is more aggressive than that of FAC. Yet, less susceptible than erosion-corrosion mechanism (tribocorrosion) – as a result of little to no corrosion film. Impingement can occur directly (associated with impact) or through shear as the liquid moves through the pipe in the longitudinal direction.

2.5. Water Chemistry Model

An electro-neutrality equation needs to be considered, during modelling of the pH and corrosive species concentrations; in a manner that the number of chemical species in an aqueous environment fulfils both charge balance and inter-related equilibria (Nesic,

1994). Shown in Equation 10 and 11 is the electro-neutrality for sulphide and carbonic concentration (C) species, respectively:

$$\text{Sulphide species: } C_{H^+} = C_{OH^-} + C_{HS^-} + C_{S^{2-}} \quad \text{Equation 10}$$

$$\text{Carbonic species: } C_{H^+} = C_{OH^-} + C_{HCO_3^-} + C_{CO_3^{2-}} \quad \text{Equation 11}$$

The pH model is pertinent for an open mechanism in which the corrosive species are established and remain unchanged. Thus, preserving the quantity of the overall destructive species. Consequently, the chemical expression imitating the amount of the overall corrosive species conservation is added to account for the concentration change of the destructive species (Nordsveen, et al., 2003), as in the expression in Equation 12 and 13.

$$n_{H_2S_{(g)}} = m_{H_2S_{(g)}} + m_{H_2S_{(aq)}} + m_{HS^-} + m_{S^{2-}} + m_{FeS_{(s)}} \quad \text{Equation 12}$$

$$n_{CO_{2(g)}} = m_{CO_{2(aq)}} + m_{H_2CO_3} + m_{HCO_3^-} + m_{CO_3^{2-}} + m_{CO_{2(s)}} \quad \text{Equation 13}$$

Where the icon n signifies the uniform molar magnitude of $H_2S_{(g)}$ and $CO_{2(g)}$. The low concentration can be calculated using the ideal gas state equation as mathematically expressed in Equation 14:

$$n = \frac{pCO_2V}{RT} \quad \text{Equation 14}$$

"The chemical equilibrium that satisfies the Gibbs free energy equation will be disturbed once the carbon steel is introduced into the solution due to electrochemical reaction between the reducible species and the steel surface (Trethewey & Chamberlain, 1988)", as shown in Equation 15.

$$\Delta G^0 = -RTlnK \quad \text{Equation 15}$$

Where, the sign ΔG^0 represents the change in Gibbs free energy at standard conditions, having a SI unit of kJ/mol

K is the equilibrium coefficient

R is the gas coefficient (8.310 J/K mol), and,

T is the temperature measured in Kelvin.

2.6. Pseudo-Passive Product Layers in a Sweet Corrosive Environment

According to Dugstad (2006), Farelas, et al., (2010), Nesic (2011) and Sun, et al., (2012) iron carbonate (siderite, $FeCO_3$), cementite (Fe_3C), and magnetite (Fe_3O_4) are some of the corrosion film expected during SSW studies. Of these films, $FeCO_3$ corrosion film is usually dominants the substrate (Jasinski, 1987; de Moraes, et al., 2000). Malik (1995) studied the behaviour of corrosion product for carbon steel in H_2CO_3-environment and found that a pH quantity of 6.500 is essential for producing the pseudo-passive iron carbonates film. The semi-passive film is, however, characterized by weak adhesion properties and low corrosion rate.

General corrosion is another corrosion mode triggered by a galvanic mechanism of the formation of this semi-passive iron carbonate film (Dugstad & Lunde, 1994). In sync, there is a surge in Fe^{2+} ion concentration in solution which leads to a pH increase. Aqueous solutions with low resistivity have an aggressive CR. In SSW-environment (H_2CO_3 – solution), with time, the dissolution of ferrite phase morphs into a thick porous Fe_3C with traces of $FeCO_3$ and Fe_3O_4 film. These findings are supported by Marc Singer (2013) who demonstrated that the precipitate of $FeCO_3$ occurs when the saturation level is above the value of one (such observation is out of the scope of this work) or when carbon steel is left to react in H_2CO_3 environment for a longer period, as discussed in Section 2.9. The formation of protective $FeCO_3$ film lessen deterioration rate by a polarizing substrate (Nešić, 2007).

The pH gradient between the bulk solution and that beneath $FeCO_3$ film generates a galvanic cell because of H^+ ions reduction (from the electrolyte) and Fe^{2+} ions (from subtract). These findings are demonstrated to instigate localized corrosion by Moiseeva & Rashevskaya (2002) and Lin, et al., (2006). As a result of high E_{corr}, a thin magnetite

(Fe_3O_4) layer occur between $FeCO_3$ scale and the substrate (Han, et al., 2008). Equation 16 shows the chemical reaction in which the thin magnetite layer is formed.

$$3Fe + 4H_2O \rightarrow Fe_3O_4 + 4H_2 \qquad \text{Equation 16}$$

As already covered the iron carbonate layer can partially be eroded mechanically or/and dissolved electrochemically during flow (Ruzic, et al., 2006). A reaction is vital for re-polarize as the pH changes (Han, et al., 2008). Consequentially leaving the bare substrate to become anodic as the potential moves toward the more negative side. "When localized corrosion occurs from a partially removed corrosion film, the FIC attack is known as mesa (Han, et al., 2008)".

2.7. Sour Corrosion Product Layers

A polymorphs FeS is usually supplemented by a cubic iron sulfide (FeS), amorphous iron sulfide (FeS), mackinawite (FeS), pyrite (FeS_2), and (Fe_3S_4). And because of fast-kinetic reactions, the unstable mackinawite (FeS) is an initial corrosion film (Fekry & Ameer, 2011). The transformation of mackinawite to other iron sulphide types depends on the environmental conditions, where stable FeS_2 forms above room temperature in H_2S – environment (Smith, 2001). Moreover, dissolved Fe^{2+} concentration has no impact on the deterioration rate and iron sulphide retention degree in pure H_2S corrosion (Sun & Nesic, 2007).

A weak mackinawite film formed instantly as a result of H_2S and Fe reaction (Yaakob, 2015). Compared to that of $FeCO_3$, the mackinawite (FeS) film forms swiftly, due to mackinawite layers comprising of coherent Fe atom. Thus, the topotaxy does not exhibit any atomic rearrangement (Shannon & Ross, 1964), which provides an optional α-Fe surface, for nucleation and growth of mackinawite (Lotgering, 1959).

Nonetheless, Zheng (2015) argues that a thin mackinawite layer is characterized by an inner FeS layer produced from a direct chemical reaction, and an outer film formed by H_2S - environment and Fe precipitation.

2.8. Electrochemical Measurements

Electrochemical measurements are based on Faraday's law were the weight of the reactant consumption at an electrode surface is proportional to the quantity of the charge passing through the cell. The corrosion rate (CR) is, therefore calculated by measuring the current. Electrochemistry measurements, thus, deal with the production and interpretation of polarization curves (potential vs current density) and the information leads to CR, surface film formation, pitting tendencies, and pseudo-passivation measurements.

When a metal is exposed to a corrosive medium, both reduction and oxidation processes occur on the specimen's surface. The coupon sample oxidizes (corrodes), and the medium reduces—the specimen functions as both anode (oxidation) and the cathode (reduction). The anodic and cathodic sites occur due to the presence of surface impurities (defects), which enables the metal to easily corrode (Sluyters-Rembach & Sluyters, 1970).

When the specimen is in service and not connected to any instrument, the specimen assumes a potential (relative to a standard reference). The potential is referred to as the corrosion potential (E_{corr}). A metal specimen at E_{corr} has both an anodic and cathodic site on its surface, and no net current can be measured. If a potential is applied to the specimen, then the sample is said to be polarized, creating a net current flow. The anode current dominates over the cathodic present when the applied potential is more favourable than corrosion potential and is referred to as anodic polarization (Stuckey, et al., 2012). The opposite of this is known as cathodic polarization, which occurs when cathodic current domination. The polarization diagrams of corroding metals are illustrated and explained in Section 3.5.

2.8.1. An Electrochemical Impedance Spectroscopy EIS Theory

EIS determinations were carried out an OCP on a broad frequency range of 100 kHz to 0.100 Hz to study the metallic substrate. An amplitude saline wave of 5 mV was applied

to the electrochemical technique to observe how the coupon sample responds to flow rate and flow geometry. Moreover, to interpret the results, Nyquist curves were used.

An EIS technique (alternative current (AC) Impedance method) is a semi-destructive testing electrochemical substrate procedure that qualitatively unearths reliable data concerning the electrochemical activities taking part on the specimen surface. Where the circuit is completed through an electrical current connection termed resistance, as expressed in Equation 17.

$$R = \frac{E}{I} \qquad \text{Equation 17}$$

Where, the icon R signifies the resistance of the circuit measured in Ohms
E is the voltage measured in V
I is the current (A)

Akin to resistance, impedance is a complex mechanism that measures the ability to resist electrical flow. The electrochemical impedance is measured through an AC potential (current signal) of the different frequencies and quantifying the reaction of the circuit. Thus, the discrepancy of the applied frequency allows the study of different electrochemical reactions occurring on the metallic substrate at different rates. Because voltage cell (galvanic cell) is chaotic during the electrochemical reaction, the electrochemical impedance is quantified through low AC frequency in a manner that the electrochemical reaction is quasi-linear within an applied voltage signal range.

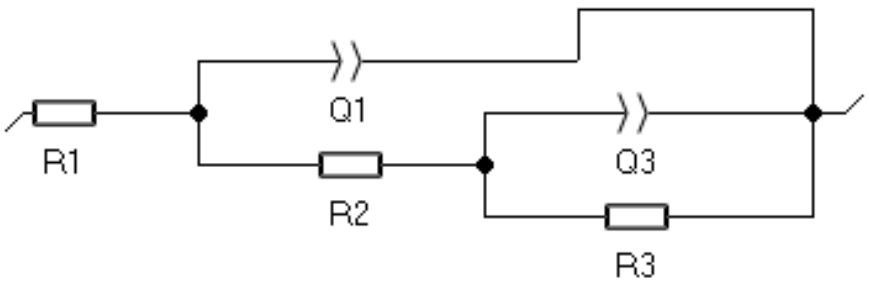

Figure 8: An equivalent circuit for a Randles circuit modified with two times constant.

Data from the EIS model was generated with an electrical circuit to model a voltage cell (galvanic cell) (Darowicki, 1995; Kinsella, et al., 1998; Ma, et al., 2000). The resulting equivalent circuit in Figure 8 was used in the study to gather electrochemical data during flow loop.

Where, the icon R_1 is the charge resistance of the solution (Ohm)
R_2 is the charge resistance of the working electrode (Ohm)
R_3 is the charge resistance of the corrosion product (Ohm)
Q_2 is the constant phase element of the working electrode (F)
Q_3 is the constant phase element of the corrosion product (F)

The Randle circuit incorporates the resistance of the solution, a dual capacitance film and the charge-transfer resistance where the dual capacitance film coincides with EIS for charge-transfer interaction. The constant phase element has a fixed phase shift angle, and its impedance describes by the following relation: $ZCpe = 1/Y0(j\omega)n$, where according to Behpour, et al., (2009) and Brytan, et al., (2016), Y0 and n are the parameters related to the phase shift angle. Döner, et al., (2011) characterized the n value as a parameter which describes the corrosion product charge transfer, where the n factor ranges from -1 to 1. With the value of -1 characterizes the inductance, 1 corresponds to a capacitor and 0 a resistor. The mapping of total impedance is called a Nyquist plot.

2.8.2. Tafel Plots (Potentiodynamic Curves)

The electrochemical parameter (corrosion potential (E_{corr}) and current density (i_{corr})) were obtained from the Tafel plots calculated directly from the EC-Lab software. The limiting current density (i_{lim}) is the PDP gradient between the activation and concentration boundary conditions which occurs when the electrode is polarized. The Tafel gradient transformation is a consequence of;

- Kinetics reaction, which is a function of the MME/SSW reactant,
- Overpotential (Butler-Vollmer equation), and

- Mass transport, which is a function of the boundary layer thickness (Fick's diffusion equation).

Without overpotential, the net current of the reversible reactions is zero. At this zero-current point, the logarithmic scale trends toward negative infinity. With both the forward and reverse reaction (at low overpotential) contributing to the net current because of the somewhat polarized electrode. The polarized area is defined as the nonlinear region between the zero overpotential condition and the so-called "Tafel region". In the Tafel region, either the forward or reverse reaction dominates. The observed current follows a linear trend of logarithmic current with increasing overpotential. The slope of this linear trend is the Tafel slope, which describes the kinetic losses due to polarization.

2.9. Electrochemical Reactions

The reducible species involved in the electrochemical reactions leads to corrosion of carbon steel. The general reaction of the dissolution of mild steel in H_2CO_3/H_2S-saturated aqueous condition and H_2CO_3-saturated aqueous environment, are respectively presented in Equation 18 and Equation 19 (Nesic, 2011):

$$Fe_{(s)} + H_2S_{(aq)} \leftrightarrow FeS_{(s)} + H_{2(g)} \qquad \text{Equation 18}$$

$$Fe_{(s)} + CO_{2(aq)} + H_2O_{(l)} \leftrightarrow FeCO_{3(s)} + H_{2(g)} \qquad \text{Equation 19}$$

The overall mild steel dissolution reaction consists of anodic and cathodic electrochemical reactions, simultaneous reacting on the steel surface:

2.9.1. Cathodic Reaction

The assumption made concerning the cathodic reaction is that hydrogen evaluation is the governing reaction parameter. Thus, when hydrogen ions (H^+) diffuse through a corrosion product film such as a diffusion boundary layer to the substrate, hydrogen evolution relating an intermediate adsorbed hydrogen atom is observed (Gerischer &

Mehl, 1959). The H^+ ions generated in the chemical reactions contribute to the reduction of electrochemical interaction at the cathodic sites, according to the following steps:

$$H^+ + e^- \leftrightarrow H_{ads} \quad \text{Equation 20}$$

$$2H^+_{(ads)} + 2e^- \leftrightarrow H_{2(ads)} \quad \text{Equation 21}$$

$$H_{(ads)} + H_{(ads)} \leftrightarrow H_{2(ads)} \quad \text{Equation 22}$$

"The electrochemical reactions at the steel substrate consist of anodic iron dissolution being oxidized at the substrate (Bockris, et al., 1961)". The dissociation of H_2S is a source of H^+, which is absorbed on the steel surface (Schmitt & Hörstemeier, 2006). The same process applies to H_2CO_3 corrosion mechanism. Therefore, carbonic acid (H_2CO_3) diffuses through the substrate; heterogenous dissociation and reduction then follow (Nesic & Sun, 2009). Because diffusion of H^+ ions through the corrosion film involve a neutral hydrogen atom absorption. H_2CO_3 serves as an additional H^+ source, where the H^+ ion first adsorb at the steel surface and is then reduces according to Equation 20. Alternatively, the adsorbed H_2CO_3 (at the surface) follows a direct reduction of carbonic acid, therefore heterogeneous dissociation, and H^+ reduction as shown in Equation 23. Similarly, the direct reduction of hydrogen sulfide is shown in Equation 24.

$$2H_2CO_{3(aq)} + 2e^- \leftrightarrow H_{2(g)} + 2HCO^-_{3(aq)} \quad \text{Equation 23}$$

$$2H_2S_{(aq)} + 2e^- \leftrightarrow H_{2(g)} + 2HS^-_{(aq)} \quad \text{Equation 24}$$

Rate-determining steps (RDS) is another functional approach used to comprehend the corrosion mechanism. Generally, electrochemical interaction, chemical reduction-oxidation reaction and charge-mass transport are regarded as the RDS. The discharge of H^+ ions from the adsorbed H_2S and H_2CO_3 can be used as the RDS (de Waard & Milliams, 1975). The adsorption hydrogen ions combine with bisulfide (HS^-) and bicarbonate (HCO^{3-}) to reproduce H_2S in MME and H_2CO_3 in SSW. According to

Schmitt & Rothmann (1977), the RDS is a gradual hydration reaction of the adsorbed aqueous solution. Shown below is the respective hydration of adsorbed sour (MME) corrosion – Equation 25 and sweet (SSW) corrosion environment – Equation 26:

$$S^{2-}_{(aq)} + H_2O \leftrightarrow H_2S_{(aq)} \quad \text{Equation 25}$$

$$CO_{2(aq)} + H_2O_{(aq)} \leftrightarrow H_2CO_{3(aq)} \quad \text{Equation 26}$$

Different metals generate similar cathodic controlling charge densities. The sweet corrosive environment has a binary cathodic reduction, which results in sweet corrosion being rigorous as compared to other robust acids with similar pH (de Waard & Milliams, 1975). The buffering of the reducible species depresses and stabilizes the pH on the substrate by generating more H^+ ions at the substrate-electrolyte interface (Remita, et al., 2008). Thus, the buffering effect enriches the H^+ ions concentration adjacent to the metallic substrate, creating a boundary layer (Pots, 1995), as shown in Equation 27 to Equation 30.

$$H_2O_{(l)} + CO_{2(aq)} \leftrightarrow HCO^-_{3(aq)} + H^+_{(aq)} \quad \text{Equation 27}$$

$$HCO^-_{3(aq)} \leftrightarrow CO^{2-}_{3(aq)} + H^+_{(aq)} \quad \text{Equation 28}$$

$$H_2S_{(aq)} \leftrightarrow H^+_{(aq)} + HS^-_{(aq)} \quad \text{Equation 29}$$

$$HS^-_{(aq)} \leftrightarrow H^+_{(aq)} + S^{2-}_{(aq)} \quad \text{Equation 30}$$

While chemical reaction controls the corrosion current density, "direct reduction mechanism comes into effect at pH values higher than 5 (Nesic & Sun, 2009)". Whilst the deceleration of hydration of the acid solution symbolizes a direct reduction mechanism, as shown in Equation 31.

$$2HCO^-_{3(aq)} + 2e^- \leftrightarrow H_{2(g)} + 2CO^{2-}_{3(aq)} \quad \text{Equation 31}$$

Zhang, et al., (2006) indicated that the direct reduction of HCO_3^- ion reaction decelerates CR as the ion increases the pH of the solution. Nesic & Sun (2009) however, disputed that direct reduction of HCO_3^- ion reaction has little effect on CR.

Depending on the charge-mass transfer rate, the cathodic species can generate I_{corr} which governs if the overall cathodic charge density is controlled by a charge-transport limit, mass-transport limit or a combination of mass-charge transfer reaction. Therefore, excessive charge-transport interaction triggers the overall cathodic charge density to be generated from the mass-transport rate (Eldik & Palme, 1982).

2.9.2. Anodic Reactions

Consistently, at the anodic site, the iron will oxidize according to Equation 32.

$$Fe_{(s)} \rightarrow Fe^{2+}_{(aq)} + 2e^- \qquad \text{Equation 32}$$

Equation 33 describes the anodic reaction rate as follows (Nesic, et al., 1996)

$$i_a = K(C_{OH^-})^{a1}(pCO_2)^{a2}10^{\frac{E}{b_a}} \qquad \text{Equation 33}$$

Where, i_a is anodic current density (A/cm^2)
K represents the equilibrium constant for CO_2 hydration reaction
C_{OH^-} is the hydroxyl ion concentration (mol/cm^3)
pCO_2 is the partial pressure (g/cms^2)
a1 and a2 are the reaction stages (reaction order)
E is the potential (V)
b_a is the anodic Tafel slope (V)

The behaviour of anodic reaction depends on pH or concentration range. For an electrolyte with $pH \leq 4$, the reaction order is equivalent to two and the anodic current density is inversely proportional to pH (Videm, 1993). The anodic charge density of a $pH > 4$ electrolytes, would show similar behaviour despite the aggressive corrosive

conditions. Therefore, sour corrosion environment and sweet corrosion environment at the same pH will experience the same anodic current density behaviour (Videm, 1993). This statement is supported through a study conducted by Linter & Burstein (1999), who suggested that the anodic types do not make an essential difference in the anodic charge density. However, between pH 4 and 5, the anodic reaction becomes less dependent on the pH, as the reaction order (a1) fall between the reaction range one and two. Above pH 5, the anodic reaction is no longer dependant on the pH because the reaction order is zero.

Thus, above pH 5, the hydroxyl ions (OH^-) serves as a catalytic agent that dissolute the iron (Fe) through the following mechanisms (Nesic, et al., 1996):

$$Fe_L + H_2O \leftrightarrow Fe_LOH_{ad} + H^+ + e^- \quad \text{Equation 34}$$

$$Fe_LOH_{ad} \leftrightarrow Fe_LOH^+_{ad} + e^- \quad \text{Equation 35}$$

$$Fe_LOH^+_{ad} + H_2O \leftrightarrow Fe_L(OH)_{2(ad} + H^+ \quad \text{Equation 36}$$

$$Fe_L(OH)_{2\,ad} \leftrightarrow Fe_L(OH)_{2\,sol} + H^+ \quad \text{Equation 37}$$

Where the net anodic reaction is given by Equation 38:

$$Fe_L(OH)_{2\,sol} + H^+ \leftrightarrow Fe^{2+} + CO_2 + 2H_2O \quad \text{Equation 38}$$

The symbol Fe_L is characterized as the surface adsorption for H_2S and H_2CO_3 solution.

Above pH value 5, the OH^- concentration adsorbed on the substrate intensifies as the steel corrode. Primarily, Fe dissolution increases until saturated, at which the pH further increases without escalating anodic reaction rate (Anderko, et al., 2000). At pH lower than 4, the desorption process can be used to determine the reaction rate due to higher charge-transfer rate (Dugstad, 2006; Nesic, et al., 1996). In contrast, when the pH >5, the charge-transfer becomes the rate-determining step (Nešić, et al., 1996).

Moreover, the carbonic anodic reaction governed by the charge transfer limit has a E_{corr} up to 200 mV (Schmitt & Hörstemeier, 2006; Nesic & Sun, 2009). Further anodic polarization on the mild steel substrate in H_2CO_3-saturated conditions would escalate the anodic dissolution due to interruption of scale formation, which acts as a thin-oxide pseudo-passive film (Linter & Burstein, 1999).

2.10. Mass Transport

Mass-transfer is an essential parameter in deterioration mechanism as many corrosion modes (including their corrosion rate) are to same extend controlled by transport to or from the substrate. FAC rate ensues when the charge-transfer rate is enough to deplete the concentration of the reactant at the substrate (Nesic, et al., 1995). In anticipation of the charge-transfer reaction becoming the RDS, the flow rate is proportional to the mass-transport rate (Chen, et al., 1992). The effect could be observed in a film-free condition where their charge-transfer controls corrosion mechanism; thus CR is proportional to flow rate (Dugstad, et al., 1994). According to Nor, et al., (2013) convection will boost the mass-transport rate on the substrate where the dimensionless hydrodynamic parameters characterize the flow effect on the mass-transport rate to a mass-transport dimensionless setting (Chen, et al., 1992).

Adjacent to the substrate exists a concentration gradient which drives ions to diffuse from a high into a low concentration region (Nor, et al., 2013). Assuming that the electromigration is negligible, the molecular diffusion will be the driving force for the mass-transport of reacting species, as a result of highly conductive electrolyte within the diffusion boundary layer (Chen, et al., 1992; Heitz, 1991).

The high flow rate, on the other hand, is related to a high mass-transfer rate that accelerates corrosion as a result of increased mass transfer. The CR will be under mass transfer control should the transported corrosive species not assist the electrochemical reactions at the substrate.

Because of secondary flow and flow separation, significant metal losses are evident in the pipe bends (curvature and deflection angle) as compared to a straight pipe of equal

length (Jeong, et al., 1997). The separation flow is caused by the inner convex surface which results in distortion flow (secondary flow) in the form of vortices convex (Liu, et al., 1994), produced by a pressure increase in the opposite flow direction (Tony, et al., 2006). Separation flow is therefore geometrically sensitive and propagates until the start of flow reattachment because distortion flow (transverse movement) streams in regions where an adverse pressure exists (Jimenez & Moin, 1991; Shoham, 2006). Awake which is a structure depending on both the Reynolds number and the geometry of the shape will form swirls (vortex) when a flow convex reaches a separation point (Jawarneh & Vatistas, 2006). Brodkey (1967) described the separate flow at a bend (convex surface) as follows:

- The stream will experience a deceleration when moving to the rear portion from the forward part of the curved surface. The forward portion brings about an increase in velocity $^{dU}/_{dx} > 0$, and a favourable pressure gradient which is a decrease in pressure $^{dp}/_{dx} < 0$. An adverse pressure exists on the rear, which describes the pressure increase in the direction opposing the flow path $^{dp}/_{dx} > 0$ where velocity decreases $^{dU}/_{dx} < 0$.

- The fluid particles on the rear portion decelerate due to interactions of the pressure gradient and the shear forces that exist near the wall. The hydrostatic stress (viscous forces) and the velocity will in time reach zero due to the deceleration of the fluid particles momentarily coming to rest.

- In the interim, the adverse pressure will continue to act and cause the fluid in that region to have a backward flow to a point where the boundary layer separates, and the flow continues in the direction of increasing pressure.

"The ratio between molecular momentum transport and molecular diffusion mass transport is denoted by Schmidt number (Sc)" (Heitz, 1991), which indicate the depth of the diffusion boundary layer (Scully, 2003). A high Sc number signifies a fine transmission limit layer (Nešić, et al., 1996) and that the convective mass-transport is preponderating as compared to molecular transmission mass-transport (Rahmani &

Strutt, 1992). The non-slip state adjacent to the substrate immobilizes flow, thus, resulting in a velocity gradient; with the fluid flow velocity reaching zero at the wall (Davies, 1972). The Sherwood number (Sh) and the Schmidt number (Sc) in mass transfer are analogous respectively to the Nusselt number (Nu) and the Prandtl number (Pr) in heat transfer when the dimensionless form of the governing equations is considered (Chilton & Colburn, 1934).

The electrochemical reaction rate is reliant on the mass-transfer rate of the reducible species interchanging between the substrate and the electrolyte (aqueous solution). For H_2CO_3-saturated environment, the mass-transport generally happens through molecular transmission and convection. The mass-transport governed by electromigration is trivial during corrosion because of an identical anodic charge and cathodic charge on the substrate (Nordsveen, et al., 2003), moreover, there is a high presence of secondary conductive electrolytes such as NaCl (Rahmani & Strutt, 1992). Molecular transmission happens within a diffusion boundary layer due to the concentration gradient, while convective mass-transfer occurs due to flow throughout the substrate. The H^+ ion reduction is controlled by hydrogen ions mass-transfer through the metallic substrate (Schmitt & Rothmann, 1977). The evidence is pronounced in strong acids such as reducible species found in H_2S – saturated environment in that hydrogen evolution rate is controlled by the rate of H^+ ion transfer to the substrate (Stern, 1955). Studies conducted by Schmitt & Rothmann (1977) and Nesic & Sun (2009) indicates that a direct H_2CO_3 reduction also has a transmission-controlling charge constituent.

Compared to the diffusion rate, the dissolution rate of hydrated H_2CO_3 are gradual because the charge-transfer reaction is the RDS. The presence of transmission-controlling charge in H_2CO_3-saturated environment indicates that the condition is slightly sensitive to flow (Nesic, et al., 1995). With hydration of H_2CO_3 being the slowest step in the reduction, and flow-sensitivity resulting from H^+ mass-transfer (Nešić, et al., 1996). The flow-sensitivity to flow-induced corrosion (FIC) can be identified where the $pH < 4$ and the H^+ ion level is significantly large (Dugstad, et al., 1994; Pots, 1995). The increase in pH reduces the H^+ concentration, resulting in corrosion being less flow-sensitive (Dugstad, et al., 1994).

2.11. Pourbaix Diagram (E-pH Diagram)

Although the corrosion mechanism is systematic, the corrosive environment remains a key factor in any corrosion condition. With E-pH diagrams as the most used method to map out the thermodynamical behaviour of the metal, with its environment. In this regard the E—pH diagrams use the potential of the aqueous solution to predict the three states a metal partakes during corrosion phenomena i.e. corrosion occurrence, passivity, and thermodynamic stability of the metal as a function of pH and potential (Videm & Dugstad, 1989). Figure 9 (a) and (b) shows an example of an E-pH diagram, with Equation 39 to 41 used to elucidate the behaviour of the E-pH diagrams when mild steel reacts with the aqueous solution.

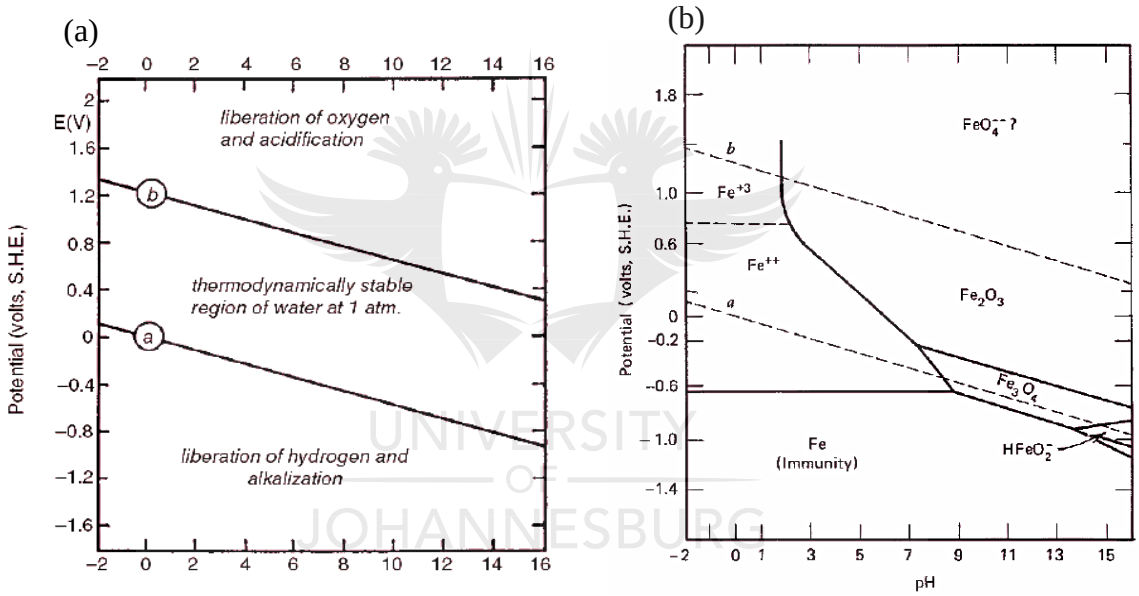

Figure 9: E-pH diagrams of (a) only water, and (b) steel in water (Pourbaix diagram (stability diagram), n.d.)

The thermodynamical conditions of the reaction are represented by each line on the E-pH diagrams. Above line (b), oxygen propagates at the steel surface according to the reaction given in Equation 39. Thus, water (H_2O) to be stable between lines – (a) and- (b).

$$\frac{1}{2}O_2 + 2H^+ + 2e^- \rightarrow H_2O \qquad \text{Equation 39}$$

Therefore, below the (a) – line, hydrogen gas propagates from the electrode surface according to the reactions given in Equation 40.

$$2H^+ + 2e^- \rightarrow H_2 \qquad \text{Equation 40}$$

The relationship between E and pH is established through the Nernst equation, as shown in Equation 41.

$$E = E^\circ - 2.303\frac{RT}{zF}\log\frac{1}{[H^+]^2} \qquad \text{Equation 41}$$

Where, E° refers to the standard redox potential of ferrous iron (V)
E is the cell potential under specific conditions (V)
R is the ideal gas constant (8.314 J/mol-K)
T is the temperature (kelvin)
F is the Faraday's constant (95484.560 C/mol)
z is the number of electrons transferred in the reaction
H^+ is the hydrogen ion concentration (mol/m^3)

On the E-pH diagrams, the horizontal line represents the potential (or electron involvement) when the steel reacts with its environment, such as the dissolution reaction shown in Equation 7 and 18. The vertical line represents the pH and shows the involvement of H^+ or OH^-, such as oxidation reaction in Equation 16 and 19 (Davies & Scott, 2006). The sloping line demonstrations the net reaction, linking the pH and potential (E). From Figure 9 (b) it can be observed that for mild steel in aqueous solution, is immune where the potential (E) is lower than - 0.500 V, regardless of pH value. Above - 0.600 V potential, Fe is reduced to Fe^{2+} or Fe^{3+} ion, depending on the pH of the solution, with the possibility of the steel being passivated with a pseudo-passive Fe_2O_3 or Fe_3O_4 corrosion film.

CHAPTER THREE

RESEARCH METHODOLOGY

3.1. Introduction

This chapter provides an outline of the research procedures followed during this study. Thus, the information regarding the research approach; the equipment used and the reasons for the researcher's choices. The section characterizes the ensuing topics into rig characterization, gravimetric analysis, electrochemical studies, and the description of the apparatus.

3.2. Background of the Study

The following section covers the miscellaneous description of the multi specimen electrochemical test-rigs prototype, as it is designed, constructed and experimentally tested by the researcher. The apparatus accounts for both the "single - and - multiphase flow" behaviour, predicting flow-sensitive corrosion and flow-non-sensitive corrosion. The section is categorized into operational parameters, the hydrodynamics and physical characterization of the test-rig consequent to flow.

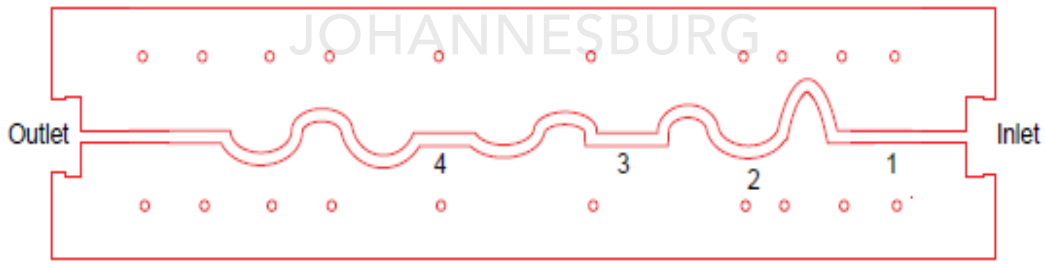

Figure 10: Side view of the prototype showing the positions of the working electrode, source author.

3.2.1. A brief background of the prototype apparatus

Although, there is no experimental laboratory setup (ex-situ) that can faultlessly duplicate the field conditions (in situ). The multi specimen electrochemical test-rigs prototype uses several small-scale flow loop mechanisms to mimic fieldwork as

realistic as possible, i.e. monitoring corrosion during disturbance flow. Electrochemical kinetics, water chemistry, hydrodynamics, charge-mass transfer parameters, FeS and $FeCO_3$ scale layer (scale formation, growth and erosion), reaction kinetics and pit perforation are all simulated inside the test-rigs according to physicochemical laws.

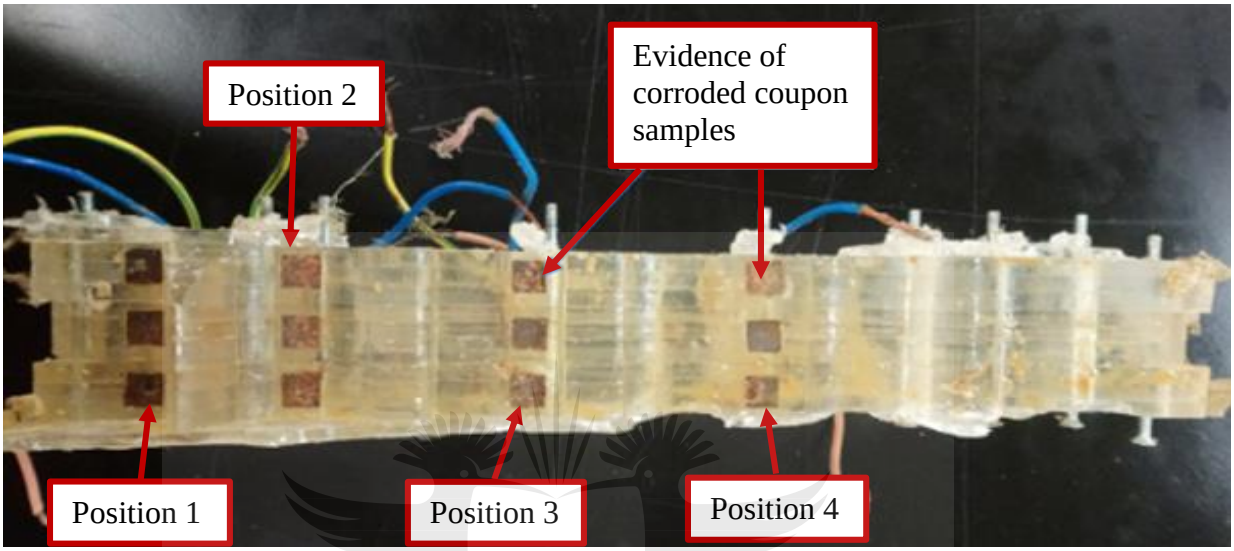

Figure 11: Top view showing evidence of corrosion product on the steel surface after 192 hours of continuous SSW flow, source author.

The spatial distribution of the bubble and liquid are diverse, and corrosion mechanism in such condition corresponds to flow velocity. The configuration of the test rig used in this study comprises of four series of the flat terrain, having the length of 4.560 cm, 4.451 cm, 4.451 cm and 4.560 cm. Four dissimilar ridges having the depth of 6.588 cm, 5.568 cm, 5.290 cm and 4.516 cm, and furrows of a height of 3.951 cm, 3.982 cm, 3.575 cm, and 3.677 cm which facilitates flow loop effect, as shown in Figure 10 and Figure 11. Thus, allowing for the physicochemical characterization during FIC as a function of hydrodynamics.

As discussed, this research aims to connect the prototype with the Bio-Logic ASA Potentiostat Electrochemical analyser model SP-150 in a manner that the open circuit potential (OCP), potentiodynamic polarization (PDP), and electrochemical impedance spectroscopy (EIS) are studied during pipeline flow loop (PFL). However, the multi specimen electrochemical test-rigs prototype was also successfully connected to the

Hanna pH HI 8424 meter, and other supportive devices (such as electrical conductivity meter and Hanna HI2400 Dissolved Oxygen Benchtop Meter) to investigate the mass transfer flow intensity, dissolved oxygen, redox potential, conductivity, and oxidation-reduction process during PFL.

3.2.2. Description and physical characterization of the prototype apparatus

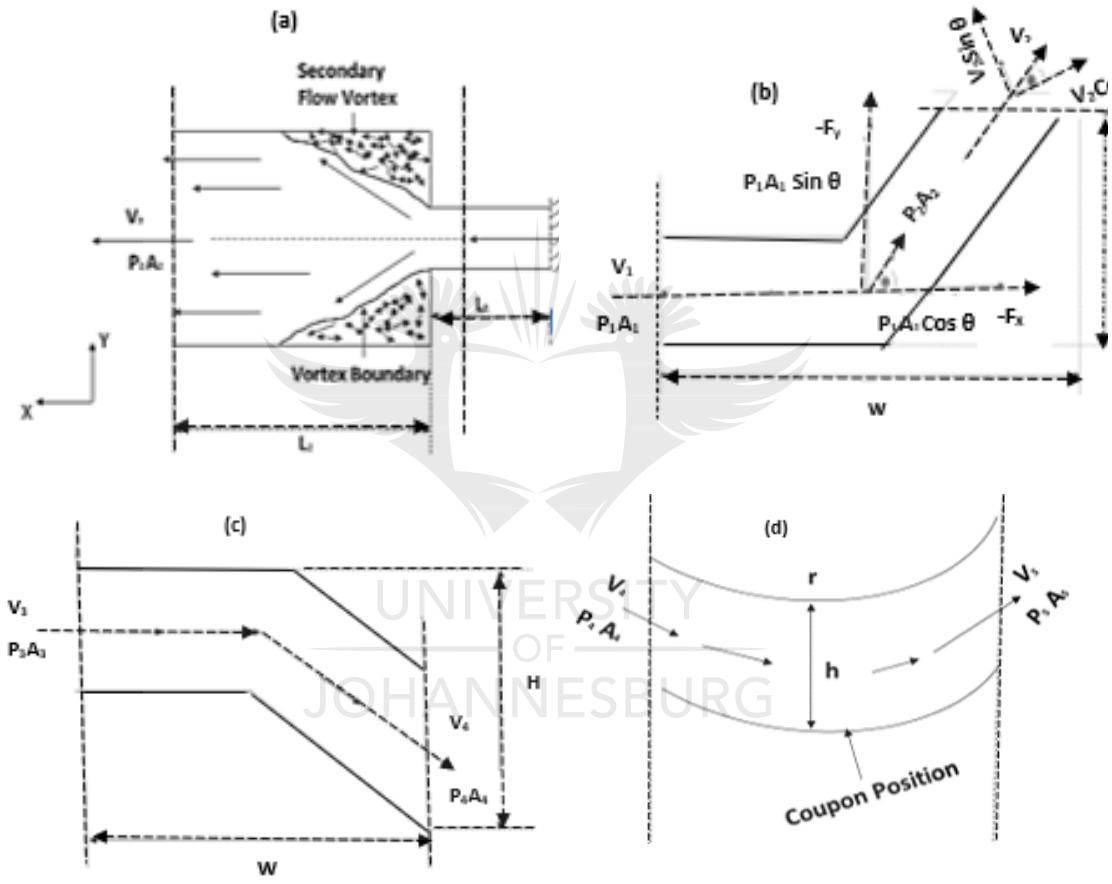

Figure 12: Schematic of the prototype test rig showing (a) Sudden pipe expansion from the inlet toward coupon sample placed at position 1, (b) Forces exerted by flowing MME/SSW solution on a pipe bend away from position 1 toward the coupon sample placed at position 2, (c) Momentum balance of a pipe bend away from coupon sample placed at position 4, and (d) indicating forces exerted by the fluid at the 180° elbow bend, position of the second set of samples.

The dimensions of the multi specimen electrochemical test-rigs prototype are $43.819 \times 6.000 \times 9.940\ cm^3$ (rectangular duct) with an average equivalent diameter of

0.912 cm. Small recess insertions designed to embed the working electrode on the same horizon as the rig floor was made inside the test-rigs to study BLC. The recess entrenched twelve sets of $1 \times 1 \times 0.008\ \text{cm}^3$ working electrode (mild steel coupon specimens), allocated in a set of three at four different locations (position $1, 2, 3$ and 4) within the test-rig, as shown in Figure 10 and Figure 11. The mild steel coupon samples were located 0.400 cm apart from each other within the set. The four coupon positions were categorized by how the test rig's configuration influenced impingement corrosion FAC and erosion-corrosion during flow loop.

The first coupon sets were placed 2.200 cm away from the test rig's inlet, in a $25.700\ \text{cm}^2$ flat terrain, as shown in Figure 12 (a). Position 1 is in the vicinity of a sudden pipe expansion, having 0.062 m/s MME/SSW bulk flow rate, with a hydrostatic pressure of 0.027 bar. The continuity law (conservation of mass) was used to determine the flow dynamics from a circular pipe to a rectangular test-rig duct. The expression of the continuity equation is shown in Equation 42:

$$\rho_1 A_1 V_1 = \rho_2 A_2 V_2 \qquad \text{Equation 42}$$

Where, the symbol ρ represents the fluid density (g/m^3)
V is the average flow rate (m/s)
A is the average pipe area (m^2)

For incompressible fluids such as MME and SSW; $\rho_1 = \rho_2$.

By integrating "Euler's equation of motion" ($\frac{dp}{\rho} = gdz + vdv = 0$), the researcher could derive Bernoulli's equation from characterizing pressure energy per unit weight ($\frac{P}{\rho g}$), kinetic energy per unit weight ($v^2/2g$) and potential energy unit weight (z) of the fluid. Thus, for the real fluid between cross-section 1 and 2, Bernoulli's equation is given by Equation 43:

$$\frac{P_1}{\rho g} + \frac{v_1^2}{2g} + z_1 = \frac{P_2}{\rho g} + \frac{v_2^2}{2g} + z_2 + h_L \qquad \text{Equation 43}$$

Where, the icon g represents the gravitational acceleration (m/s^2)

ρ represents the fluid density (g/m^3)

P is the hydrostatic pressure (g/ms^2)

h_L is the energy loss between the two cross-sections (m)

z is the pipe length or distance the fluid covers inside a pipe (m)

"As already mentioned, flow speeds up CR through an increase in mass-transfer rate or by removing (or damaging) the protective corrosion product film (Nešić, 2007; Nesic & Sun, 2009)". When a fluid flows through a sudden pipe expansion such as the one shown in Figure 12 (a), the development of the fluid flow entirely depends on the downstream contraction to an upstream expansion at a distance (L_1) (Boger, 1987). Thus, the original flow from a contracted tube no longer traces the rectangular duct expansion boundary. Hence, there are eddies current at the corner of the rectangular duct where the contraction plane detaches from the wall at a distance (L_2). Since these limits the flow range, the flow rate will increase. Thus, developing a specific velocity profile at the entrance of the circular pipe. After the contraction plane, the centre-line velocity continues to develop until it reaches 99% of its fully developed value. At low Reynolds number, the "loss coefficient is inversely proportional to the Reynolds number", as shown by Fester & Slatter (2009) using Equation 40.

$$k_{con} = \frac{C_{con}}{Re} \qquad \text{Equation 44}$$

Where, the symbol Re represents the Newtonian Reynolds number for incompressible fluids

k_{con} is the loss coefficient

C_{con} is the laminar flow loss constant

The vortex size decreases as the fluid velocity increases and the velocity profile changes from being partially developed to being uniform (flat) at the entrance of the downstream tube (Ramamurthy & Boger, 1971).

According to Boger (1987), creep flow exists at $Re \leq 1$, where the velocity profile is distorted slightly from being fully developed as the fluid enters the larger rectangular

duct from the smaller pipe and the profile (including vortex reattachment length) is independent on the Reynolds number. The inertial flow will only dominate at Re > 50 (Freund, et al., 2012). The stationary vortex and shear thinning decreases in size as the Reynold number increases (Bazhenova & Semenov, 2013).

A concavity (or velocity overshoots or off-centre maxima) exists in the entrance velocity profile at Reynolds number between 50 and 200 (Qu, et al., 2013). The concavity depth increases with Reynolds number (Re) and contraction ratio (β_{con}) (Rahman & Biswas, 2009).

The sudden change in the area will cause the flow to contract gradually from a smaller pipe into a larger rectangular duct. At a low Reynolds number above 200, a sudden change in the area will cause the flow to enter the pipe jet-like and inertia forces (Pienaar, 2004).

The second coupon sets were placed within an ($87\ cm^2$) 180° Elbow furrow segment (signifying stagnation zone), $8\ cm$ away from the first set of working electrodes, as shown in Figure 7 and Figure 12 (d). A set of coupon samples were embedded at bottom of the 180° Elbow furrow (where the rig encourages directional change) to study the effect of direct impingement at 0.018 m/s flow rate (under 0.026 bar hydrostatic pressure). The law of conservation of momentum states that "the net force acting on the mass fluid is equal to the change in momentum of the flow per unit time in that direction", - such concept was used to determine the momentum balance through the bend. Erosion-corrosion which depends on erosional velocity, breakaway velocity, threshold velocity or critical velocity describes the velocity beyond which the rate of metal removal is proportional to velocity. The critical velocity represents the point at which inhibitors (or corrosion protective film) can no longer be maintained, which impedes corrosion on the facet (Duncan, n.d.). Erosion rate (or penetration rate) is defined as the rate in which fluid flow reduces the wall thickness (metal loss) because of impact or shear stress.

A stagnation length model was used in this study to predict erosion in bend geometry (Mohyaldinn, et al., 2016). The equivalent stagnation length (L) is a function of pipe diameter (D) and can be calculated using Equation 45:

$$\text{Bend: } L = L_0(1 - 1.270\tan^{-1}(1.010D^{-1.890}) + D^{0.129}) \quad \text{Equation 45}$$

The erosion model in this study assumes a one-dimensional flow field in the stagnation zone that has a linear velocity profile toward particle motion. The initial particle velocity (V_o), can be assumed to be the same as the stream flow rate, in single-phase flow. An assumption that cannot be associated with the multiphase flow, when there is a slip between the bubble and transient fluid particles. The erosion severity in such a region relies on duct geometries, fluid properties and fluid parameters, Figure 7 and Figure 12 (b) demonstrate evidence of such effects.

The third coupon sets were placed inside a 13.700 cm^2 flat terrain, were MME/SSW bulk solution streams over the coupon samples at position 3 at 0.116 m/s, under a hydrostatic pressure of 0.028 bar. The fourth and final sets of mild steel coupon sample were placed inside a 14.800 cm^2 horizontal terrain, were MME/SSW bulk solution streamed at 0.107 m/s over the coupon sample, under a hydrostatic pressure of 0.029 bar.

The final CR were recorded from an average PDP data of the three mild steel coupons (working electrode) per region. Similar to Featherstone & Nalluri (1995) findings, the effects of dissimilar protrusion of the test-rig used in this study is predicted to enhance the corrosion mechanism in each region differently. This is as a result of erratic flow behaviour caused by fluctuating flow rate, increased hydrodynamic stress and momentum changes.

3.2.3. Delimitation of the prototype during operational

The pipeline flow loop (PFL) experiments were performed inside a multi specimen electrochemical apparatus, having four distinct positions and flow parameters. MME bulk solution (H_2S −dominant environment) were respectively streamed for 24-hours

and 192-hours at ambient temperature, under conditions cited in Section 3.2.2. to study the corrosion mechanism of a single-phase flow (uniform flow) and marginal turbulent flow during flow-sensitive conditions (pH 1.920). Then after, SSW bulk solution (H_2CO_3 −dominant environment) was used to understand and compare the corrosion mechanism of the same system (under the same conditions) during a flow-non-sensitive condition (pH 8.020).

3.3. Experimental setup and test procedure

3.3.1. Specimen Preparation

A set of specimens cut from the same light plate were respectively sectioned into a $1 \times 1 \times 0.008\ \text{cm}^3$ for electrochemical studies and $5 \times 8 \times 0.008\ cm^3$ for gravimetric purposes. After sectioning, the as-received bare samples are clean in Clarke's solution (ASTM G1-03, 2017). Rinsed in distilled water, carefully dried with a lint-free towel before respectively being used for experimental purposes.

3.4. Baseline Test

The gravimetric study was performed as a baseline test to demonstrate the corrosivity of mild steel in MME and SSW solution. This test was done to identify the susceptibility of carbon steel in MME and SSW solution. The gravimetric study will further supplement and assist interpret the electrochemical results gathered from PFL study.

3.4.1. Weight Loss Measurements (Gravimetric Test)

Weight loss determination is a commercial, conservative manner for investigating metallic corrosion parameters. Since gravimetric experiments procedure does not require any assumption regarding the actual identity of corrosion species. In this regards the $5 \times 8 \times 0.008\ \text{cm}^3$ as-received mild steel coupon samples are weighed before and after being submerged into the MME/SSW corrosive environment. The coupon samples were subjected to a 24 hours immersion test for 8 days, in a manner

that a 24, 48, 72, 96, 120, 144, 168 and 192 hours corrosion rate (CR) profile was generated at ambient temperature. The coupon samples used in this study approximately weighted 23.215 g, where the samples weights were measured to the nearest 0.001 g using an analytical balance with four decimal place digits. The CR was determined using Equation 46.

$$C.R._{(m/yr)} = \frac{534\,W}{tAd} \qquad \text{Equation 46}$$

Where, the symbol $C.R.$ represents the corrosion rate measured in m/yr

t is the time the coupon samples spent in the corrosive environment (electrolyte) measured in hours

A is the total area in contact with the electrolyte measured in m^2

d is the density of the coupon sample (g/m^3)

W is the mass difference, i.e. before corrosive environment exposure after exposure (g)

After each immersion period, the coupons were taken out of the aqueous solution, pickled at ($\pm$ 60 $^{\circ}$C) in Clarke's solution (ASTM G 1-03) and rinsed with acetone before allowing the coupon samples to dry. After drying, the coupons were weighed. The information depicts the mechanism in which the two aqueous solution favours or hinders corrosion product formation, as a function of CR.

3.5. Electrochemical Studies

Corrosion mechanism can be elucidated in terms of electrochemical interaction, where applied voltage yield information on corrosion rates (CR), such as potentiodynamic anodic polarization (PDAP) of a metallic specimen (ASTM G73 - 98, 1998). A ($1 \times 1 \times 0.008$ cm^3) coupon samples (mild steel) were sectioned from an as-received sheet and placed inside the bottom recess within the test-rigs for electrochemical studies. In a manner in which the recess exposes only 1 cm^2 of the coupon surface for PDP, and EIS studies. The density of the specimen used in this study was 7.860 gcm^{-3}, while the equivalent weight, according to the (ASTM G102, 1994) was 28.200. The equivalent weight is calculated through Equation 47:

$$\mathrm{Fe}_{(\mathrm{equivalent})} = \frac{\text{weight \%} \times \text{valency number}}{\text{atomic weight}} \qquad \text{Equation 47}$$

Electrochemical techniques are experiencing popularity in corrosion studies for the rapid nature in that electrochemical data can be examined. Thus, "long term corrosion studies" (gravimetric investigation), can now be performed within several minutes (depending on the metal and corrosive environment) to hours, with an option to investigate for days and months. The popularity growth is also owed to the accuracy that techniques (electrochemical) provide as compared to other corrosion evaluation methods. In this work, OCP, PDP, and EIS were carried out to test mild steel coupon samples, corroding during disturbance flow at different velocities. The electrochemical experiments were performed using the Bio-Logic ASA Potentiostat Electrochemical analyzer model SP-150, as shown in Figure 13. The analyzer (equipped with EC- Lab software) has a three-electrode corrosion cell (working electrode-mild steel, the counter electrode - graphite and reference electrode – saturated calomel electrode). Thus, the researcher took advantage of the Bio - Logic ASA Potentiostat Electrochemical analyzer model SP-150 capabilities of loading multiple experiments simultaneously; without affecting the results of the other specimen.

The working electrode (mild steel) freely corrode under OCP conditions for roughly about $\frac{1}{3}$ hours (after 24 hours and 198 hours of corrosive condition exposure, respectively) to attain a steady-state corrosion potential before PDP and EIS experiments were conducted.

PDP is widely used to gather data concerning corrosion parameters (especially electrochemical deterioration mechanisms and rates) and the materials susceptibility to disintegrate in specific conditions. "Polarization methods involve changing the potential of the working electrode and monitoring the current, which is produced as the function of time or potential" (Mofu, et al., 2017). The polarization studies were carried out with a scan rate of $0.125\ \mathrm{mVs}^{-1}$. The PDP determination was conducted from cathodic to anodic direction range concerning Saturated Calomel electrode (SCE) in an OCP range of $-250\ \mathrm{mV}$ to $+\ 250\ \mathrm{mV}$. The Tafel plot (potentiodynamic curves) were

concurrently developed, and PDP parameters were obtained and interpreted to characterize the mild steel corrosion behaviour during loop flow.

Figure 13: Electrochemical experiment during SSW flow loop, source author

3.5.1. Open Circuit Potential (OCP)

In electrochemistry, OCP is the corrosion potential (E_{corr}) of a disintegrating electrode in an aqueous solution. For the reason that the anodic and cathodic reactions occur at an equivalent rate. Open circuit potential is referred to as free E_{corr} because the net current in the external circuit is zero. The efficacy of electrochemical techniques such as PDP and EIS depends on the stability of the OCP. The resistance gradient of the OCP is usually maintained below 5 (Am), and any OCP changes above this range raise doubt on the generated electrochemical results.

3.6. Local and Average Mass Transfer Coefficient

Because corrosion involves the interaction between the mild steel and the MME/SSW solution, Equation 48 was used to determine the local mass-transfer constant between MME/SSW bulk flow and the duct wall. The approach is based on the average limiting current density (i_{lim}) which drives the electrochemical reaction to its maximum rate, and it is controlled by an ionic reaction from the MME/SSW electrolyte to the steel surface. Thus, allowing the ionic flux to be expressed as a function of concentration gradient, and convection diffusing at the substrate.

$$K = \frac{i}{nF(C_b - C_o)} = \frac{i_{lim}}{nFC_b} \qquad \text{Equation 48}$$

Where, the symbol K represents the average mass-transfer coefficient measured in m/s

i is the current density measured in amp/m^2

n is the number of electron transfer

F is the Faraday's number (96500 c/mol)

C_b is the concentration of the ion in the MME/SSW solution measured in mol/m^3

C_o is the concentration of the ion at the steel surface measured in mol/m^3

i_{lim} is the limiting current density amp/m^2

3.7. Physicochemical Characteristics

The physicochemical characterization mainly focuses on the dynamic concerning mild steel corrosion during this study. The following characterization techniques were used in this study, and the coupon samples were safely stored in a desiccator:

3.7.1. Optical Microscopy

The as-polished specimen was analysed for metallographic features to obtain optical micrographs using Leica DM6000M fitted with Leica DFC 490 camera.

3.7.2. Chemical Analyses of Mild Steel

The Bruker Q4TASMAN arc spark OES connected via a computerized Arc Spark Optical Emission Spectroscopy (ASOES) was used to study the elemental composition (chemical composition) of the mild steel coupon sample. Before analysis, the surface of the coupon sample was mechanically grinded with a silicon carbide paper (progressively up to 150 grit), and a spark profile was performed across the substrate where the elemental analysis was deduced from the average number of sparked sites.

The chemical analysis through the Bruker Q4TASMAN arc spark OES comprises of an applied electrical spark produced between the electrode and the coupon specimen. The high energy within the plasma discharge vaporizes the atoms. The distinctive discharge spectrum is then produced by vibrant atoms and ions within the discharge plasma. A single element produces many characteristics of spectral emission lines (Light); thus, this light is split by a deflection strident to generate the emission spectrum for the element of interest. Hence, the intensity magnitude of each emission spectrum is proportional to the elemental concentration. The photomultiplier tubes control the extracted spectrum for individual elements, and the spectrum intensity governs quantitative and qualitative examination of the target element.

3.7.3. Scanning Electron Microscope (SEM)

A surface morphology study was performed on the mild steel coupon samples before and after corrosion exposure using an SEM, where the results were assessed through the SEM TESCAN with Energy-Dispersive X-ray Spectroscopy (EDX) analysis software (performance in Nano space). The examination was conducted at high magnification (JSM - 5800LV) with the assistance of a “computer-controlled field emission” SEM equipped with an “energy dispersive X-ray” system. Data was gathered over the specimens’ selected surface area, where the 2-dimensional image demonstrations spatial differences of the sample’s properties.

3.7.4. Inductively Coupled Plasma Atomic Emission Spectroscopy (ICP AES)

ICP-AES was used to measure the concentration of the cations in MME and SSW solution before and after corrosion exposure. The emission spectrophotometric technique ultimately degenerates the specimen into essential elements and ions. The technique takes advantage of the fact that vibrant electrons discharges energy at a specified wavelength as they revert to the original state (subsequent excitation by high-temperature Argon Plasma). The unique mechanism of this system is that the apiece element discharges energy at unique wavelengths to their atomic nature. The original electron energy transfer is unique to an individual element due to its dependence on the orbital electronic configuration where energy transfer is inversely relative to the wavelength of electromagnetic radiation.

The energy intensity discharged at a preferred wavelength is relative to the concentration of the examined element. Thus, by controlling the intensity of the discharged wavelengths on a sample, one can quantitatively and qualitatively discover the elements from the specimen proportional to a reference standard.

3.7.5. Ion Chromatography (IC)

IC was respectively used to quantify the concentration of the anions in MME and SSW solution before corrosion exposure. IC measures ionic species concentrations by splitting the ions on the bases of their interaction with the resin. Ionic species separation depends on species concentration and magnitude. The aqueous solution flows through a pressurized chromatographic column where the column constituent absorbs the ions. The absorbed iron splits from the column as soon as the liquid solution flows through the column where the “retention time” of unique species measures the samples ionic concentrations.

3.7.6. X-ray Fluorescence (XRF)

An "XRF Rigaku ZSX Primus II with SQX analysis software" using the scatter method was used to determine the bulk and elemental chemistry of the corrosion product. The high-frequency inverter with a maximum rating of 4 kW, working at 60 kV and 150 mA using a (Rhodium) tube helps generate a high X-ray voltage. The technique relies on the sample's atomic behaviour, which excites the samples when it interacts with the X-ray voltage. The vibrant specimen, sequentially, discharges X-rays along the spectrum wavelengths, thus, characterizing the specimen's atoms.

In this study, 50 (diameter) $\times$ 30 mm^2 (height) corrosion product samples, resulting from exposure of MME and SSW solution were respectively loaded into the equipment to detect heavy and light elements from uranium (U) to fluorine (F).

3.7.7. X-ray Diffraction (XRD)

The collected MME/SSW corrosion product was analyzed using Rigaku Ultima IV X-ray Diffraction (XRD) with PDXL analysis software, where the mineralogy of the multi-layer film was studied by a scattered slit method. The technique relies on a reproduction X-ray beam generated by a copper tube. The tube produces high voltage X-rays with a maximum rating of 3 kW, working at 45 kV and 60 mA which determines the identity of the specimen's crystalline phase by generating the unit cell dimension data through the D/teX Ultra scintillator.

RESULTS AND DISCUSSION:

The findings obtained from this study are divided into the following three chapters.

- Chapter Four provides the chemical characterization of the as-received mild steel coupon samples before corrosion exposure, together with the characterization and discussion of the pre-and post-test evaluation of the as-received MME/SSW electrolyte before and after corrosion exposure.

- Chapter Five characterizes and discusses the evaluation of Metallography of the as-received mild steel sample during this study, together with the characterisation of their corrosion product using Optical micrography, SEM, EDX, XRF and XRD.

- Chapter Six includes the comparison of corrosion evaluation during pseudo-steady state (PSS) and pipeline flow loop (PFL) conditions. The description of the gravimetric and electrochemical results are also provided.

CHAPTER FOUR

PRE-AND POST-TEST ASSESSMENT

4.1. Introduction

The following chapter provides the pre-and post-test evaluation which characterizes the physicochemical properties of mild steel and the chemical properties of the electrolyte (metal mine effluent - MME and synthetic seawater - SSW) used in this study.

Water chemistry is paramount to electrochemical deterioration as aqueous solution serves as an electrolyte pathway, allowing electrochemical transfer amid the anode and cathode to fulfil an electrical circuit (Trethewey & Chamberlain, 1988); which affects the pH, and pseudo-passive films formation through dissolved species.

To comprehend the corrosion mechanism of mild steel in MME and SSW solution, the elemental composition of the electrolytes (MME/SSW solutions) was respectively sampled before and after corrosion exposure. The thermodynamic and kinetic reaction was studied using Medunsa Aqua software and leachate behaviour. All experiments were performed under free pH (pH was not controlled) at ambient temperature.

4.2. Pre-Test Evaluation

The pre-test evaluation was performed to characterize the elemental components of the mild steel and the electrolyte(s) used in this study.

- The Chemical Analysis was carried out on the as-received mild steel coupon samples using a computerized Arc Spark Optical Emission Spectroscopy (ASOES) according to the sample preparation specification highlighted in Section 3.7.2, results are shown in Table 1.

- Chemical characterization of the as-received MME and SSW solutions were determined through both the ICP-AES and (IC) as highlighted in Section 3.7.4. and 3.7.5. Only the bulk elemental composition of the MME/SSW solution are

respectively shown in Table 2 and Table 3. Moreover, only the sulphate and chlorides ions are prioritized in the discussion because of the corrosivity aggressiveness order ranges from sulfate > chloride > bromide > perchlorate > iodide superior to nitrate (Brett & Melo, 1997).

4.2.1. Chemical Analysis

Table 1: Elemental composition of the as-received mild steel, with iron forming the weight percentage balance element, ~ 99.480 Wt%.

Element	**C**	**Mn**	**P**	**S**	**Si**	**Cr**	**Ni**	**Mo & V**	**Al**	**Cu**
Weight (%)	0.081	0.231	0.022	0.012	0.010	0.007	0.008	<0.001	0.053	0.010

The elemental composition results confirmed that the steel sheet used in this study was low carbon steel. The mild steel used in this study has a limited alloy content of less than 1 Wt%. Such levels of alloy additions are not expected to have a consequential effect on corrosion mechanism (Climax Molybdenum Company, 1953; Jahn, 1954; Larrabee & Coburn, 1962; Larrabee, 1953). However, the entrapment of such level of alloy element can facilitate non-metallic inclusions.

4.2.2. MME Bulk Chemical Composition Results

A 1.920 pH solution of MME samples, with a density of 1015.300 kg/m^3 were collected from an open pits voids of Sibanye-Stillwater Cooke operations to perform electrochemical corrosion study. The as-received MME solution was then tested for elemental composition before corrosion exposure.

Table 2: Bulk elemental composition of MME bulk solution collected from the open pit voids at Sibanye-Stillwater Cooke Operations

Elemental Composition	Al	Si	S	P	Cl	Ni	K	Ca	Mg	Na	Fe
Concentration (ppm)	32	95	7684	1110	61	455	38	264	192	257	1260

Table 2 shows that MME bulk solution had high sulfur (S) concentration (7684 ppm) and phosphorous (P) concentration (1110 ppm) which is markedly expected to increases the CR by lowering solution resistance and thus, promotes hydrogen evolution. The high electron affinity of S for Fe (steel) than P, together with the high sub potential value of SO_4^{2-} ions will facilitate the dominance of FeS corrosion film, characterized by weak adhesion properties which intern encourages pitting.

4.2.3. SSW Bulk Chemical Composition Results

For SSW electrolyte, an artificial red salt solution of 3.6% (36 ppt) is made by weighing 36 gram of Coral Pro salt in a beaker and topping it up with 1L of deionized water. The solvent is then homogeneously mixed with a magnetic stirrer (set at 200 rpm) at room temperature to produce SSW solution (ASTM D1141-98, 2013). The solution was then tested for elemental composition before corrosion exposure.

Table 3: Bulk elemental composition of SSW, produced using "Coral Pro Salt"

Elemental Composition	Sr	Cl	Br	K	Ca	S	Mg	Na	C	Fe
Concentration (ppm)	9.3	19748	67	394	474	876	1357	10783	45	0.093

The presented synthetic seawater elemental composition does not exist on their own but are attracted to preferential ions of opposite charge, results shown in Table 3. Thus, sodium (Na^+), chloride (Cl^-), magnesium (Mg), sulfate (SO_4^{2-}) and calcium (Ca^{2+}) as abundant dissolved ions. The ion-substrate interaction (together with the concentration of the dissolved oxygen) increases the corrosion rate. Na^+ and Cl^- ions are the most

abundant constituents of sea salt, respectively read at a concentration of 151 ppm and 19748 ppm in SSW solution.

According to the adsorption theory (Marcus & Maurice, 2004), once in contact with the metal surface, Cl^- ions favour hydration of metal ions and increase the metal ions migration from the metal surface to the bulk solution. However, the effect of adsorbed oxygen decreases the rate of metal dissolution (Revie, 2008). Cl^- ions do not chemically react with the metals but rather assume a role as a catalyst in the electrochemical process. The chloride ions (Cl^-) in the solution helps remove the metal cations accumulated on the anode by forming soluble compounds, and this contributes to an accelerated anodic reaction and thus faster rusting of the metals (Xi & Xie, 2002). Moreover, the high concentration of chloride and the low oxygen concentration may also enhance the corrosion rates and initiate the pit. Thus, Cl^- ions act as a cathodic reactant.

4.3. Post-Test Evaluation

The post-test evaluation was performed to predict the thermodynamic behaviour and understand the kinetics of the reaction when mild steel respectively reacts with MME/SSW bulk solution.

4.3.1. Redox Potential behaviour with immersion time

The pH and the potential of the MME/SSW bulk solution were observed throughout the experiments, were the Oxidation Reduction Potential (ORP) was adjusted to fit the Standard Hydrogen Electrode (SHE) as prescribed by Stringgow (2013). The corrected ORP value was used to determine pe value using Equation 49.

$$pe = Eh/0.059 \qquad \text{Equation 49}$$

pe donates the negative logarithm of the electron activity.

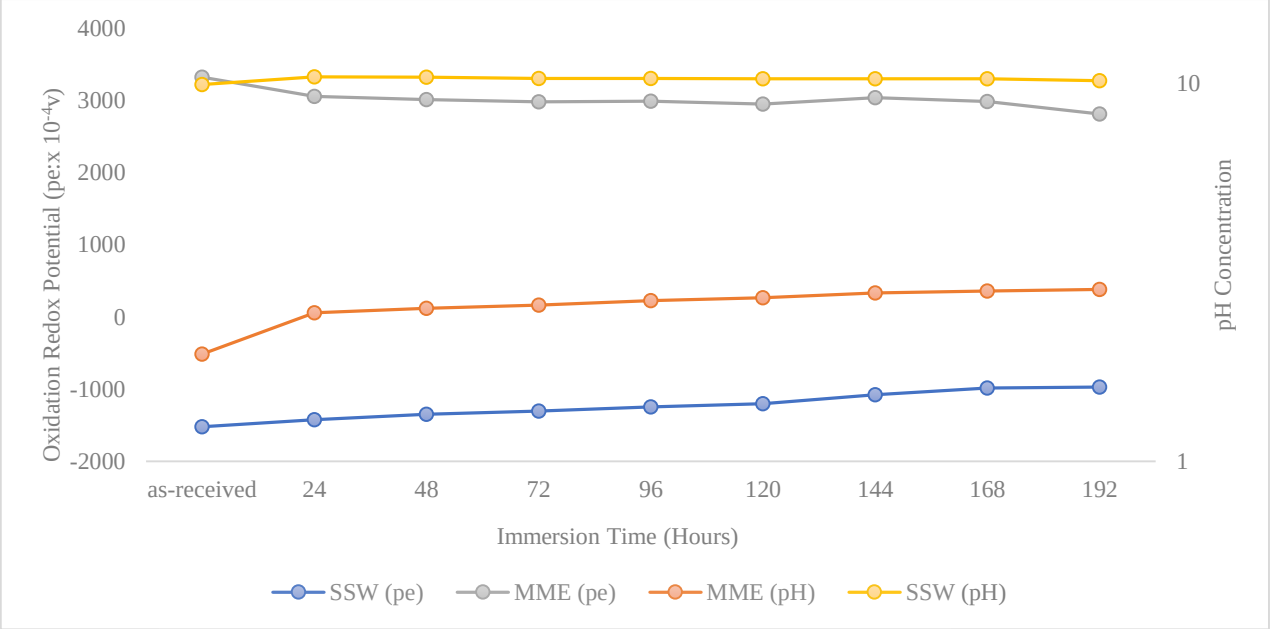

Figure 14: The dynamic behaviour of redox potential and pH in MME and SSW solution, respectively during PSS condition.

Figure 14 and Figure 15 respectively showed that MME solution had a higher redox potential than SSW solution, which decreases with immersion time (exposure time). The decrease in electron activity was attributed to the increase in the solution's conductivity with immersion time. Thus, metal loss increases the ions in solution, which intern increased conductivity due to an increase in solution resistance (R_1).

The increase in MME pH is caused by various ions such as ferrous ions, sodium ions, chloride ions, manganese ions, sulphate carbonate ions and bicarbonate ions in solutions which decreases the reduction of hydrogen ions (Davies & Scott, 2006). Whilst the decrease in SSW pH was attributed to the reduction of hydroxyl ions by corrosion process.

The decrease in potential (E) during PSS condition indicate scale formation of corrosion film. Thus, ions were taken from the solution. The increase in potential (E) under PLF indicates a significant gain of metal in solution. Such high metal concentrations are usually experienced under flow-sensitive corrosion.

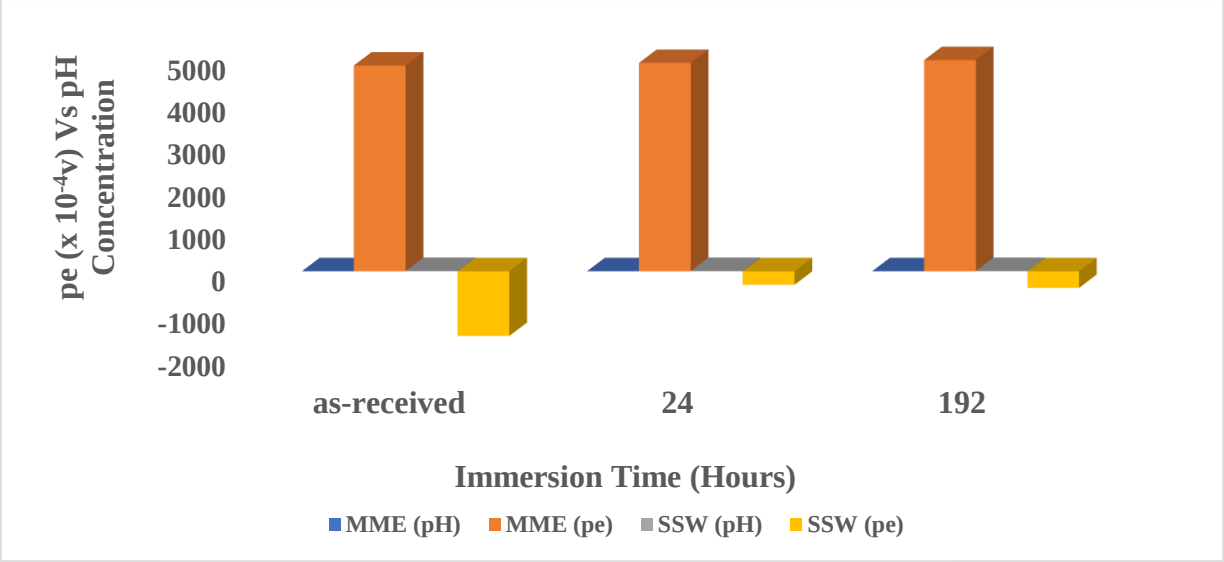

Figure 15: The dynamic behaviour of redox potential and pH in MME and SSW solution, respectively during PLF condition.

4.3.2. Effect of dissolved oxygen (DO) and ionic conductivity on the iron (Fe) dissolution behaviour of mild steel in MME and SSW solution.

Metallic corrosion attack in MME and SSW solution is primarily dependent on the salt content (which increase the electrical conductivity) and its oxygen content. The electrochemical transfer (from the conductive metal) and ions (through the electrolyte) are the two primary corrosion mechanism participating in an aqueous solution. During anodic oxidation, the metallic surface dissociates, releasing ions into the electrolyte solution while the cathodic reaction site discharges hydroxyl ions (OH^-) and dissolved oxygen (DO) from the solution (Misawa, et al., 1974).

Figure 16 and Figure 17 respectively dissolved oxygen (DO) and ionic conductivity results of MME/SSW during PSS and PLF. The DO results showed that the oxygen reduction reaction of mild steel is controlled by mass - charge transfer. At high Cl^- ion concentration (such as that found in the SSW solution), the cathodic current is predominantly mass-transfer controlled and steadily decreases with the flow. At low Cl^- ion concentrations (such as that found in the MME solution), the current is predominantly charge-transfer controlled and increases with the flow. Hence, the

driving force of O_2 reduction reaction was significant (ranging from 8.600 ppm for the as-received MME solution to 20.600 ppm after 192 hours in a corrosive environment), which resulted in dissolved oxygen (DO) gradually accelerates Fe dissolution by increasing the cathodic process.

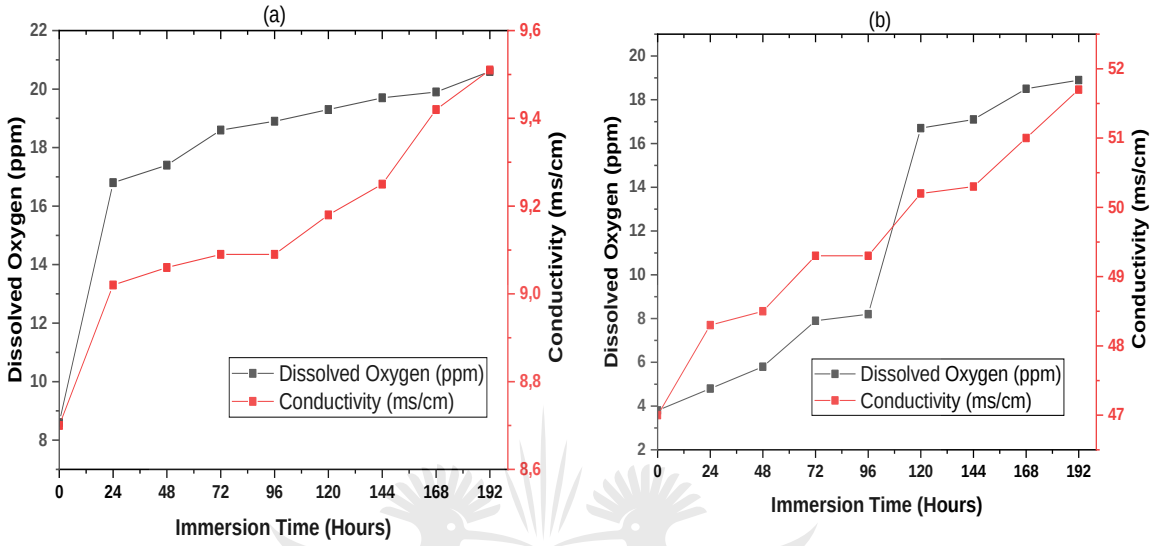

Figure 16: The kinetic behaviour of DO and conductivity under pseudo-steady state (PSS): (a) MME; and (b) SSW

However, under the pipeline flow loop (PFL), DO is consumed by the corrosion reaction, especially for the 192H MME studies were corrosion depleted coupon sample. Therefore, the DO concentration in the PFL decreased from 8.400 ppm to 7.900 ppm for MME study and 3.200 ppm to 9.900 ppm for SSW study. Because oxygen depletion follows the first-order kinetic law during pipe corrosion, DO concentration required to suppress flow-induced corrosion (FIC) was not affected by the velocity.

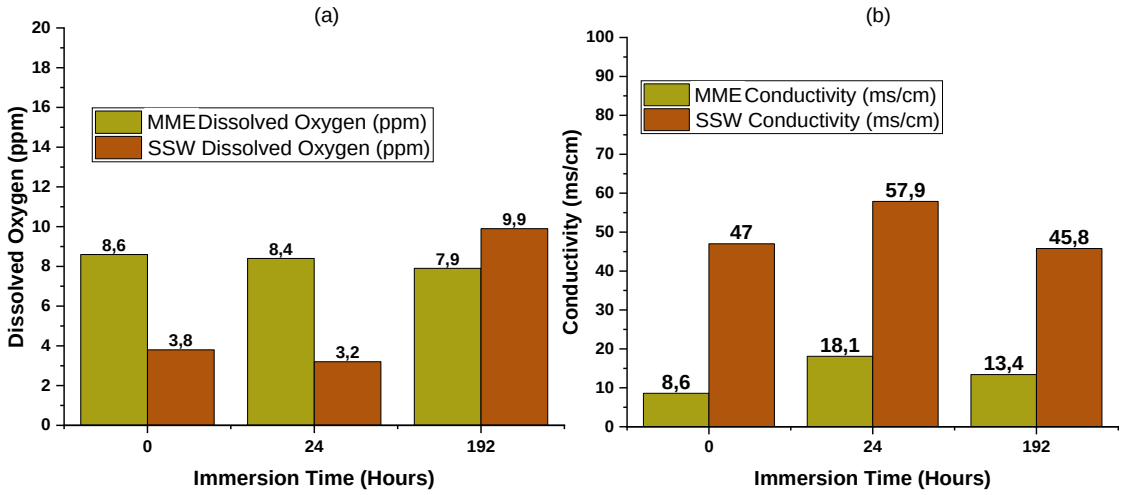

Figure 17: The dynamic behaviour of MME and SSW under pipeline flow loop (PFL): (a) DO; and (b) conductivity.

The low DO (3.200 ppm to 9.900 ppm) indicates that the transfer rate of oxygen could not satisfy the needs of the cathodic process. Thus, inhibiting the oxygen reduction, and the electronics formed by the Fe dissolution. Due to a lengthier oxygen diffusion path. The weakened depolarized O_2 reaction slows down the anodic reaction, i.e. decreasing the charge transfer reaction (R_1) and corrosion current density (i_{corr}). Figure 17 (a) indicated that the oxygen solubility in MME and SSW solutions respectively decreased with concentration of dissolved salts (ionic conductivity) irrespective of the flow conditions (PSS or PFL).

Conductivity, on the other hand, is a quantification of the aquatic solution to pass electrical flow, which is proportional to the ionic concentration in solution. These conductive ions originate from alkalis (chlorides (Cl^-), sulphides (SO_4^{2-}), and carbonate (CO_3^{2-}) compounds) and dissolved salts (chloride (Cl^-), sodium (Na), magnesium (Mg), calcium (Ca), potassium (K), iron (Fe), and bromine (Br)). The ion concentration facilitates corrosion current, i.e. cathodic reaction (oxygen reduction) and anodic reaction (iron dissolution).

4.3.2. Pourbaix Diagram

The reducible species of the MME and SSW solution were used to study the electrochemical stability for different redox states of mild steel as a function of potential and pH. Medunsa Aqua software together with electrochemical series were used to study and interpret the thermodynamic reaction during this study. The generated electrochemical redox states will help predict the corrosion occurrence by estimating the composition of the corrosion product.

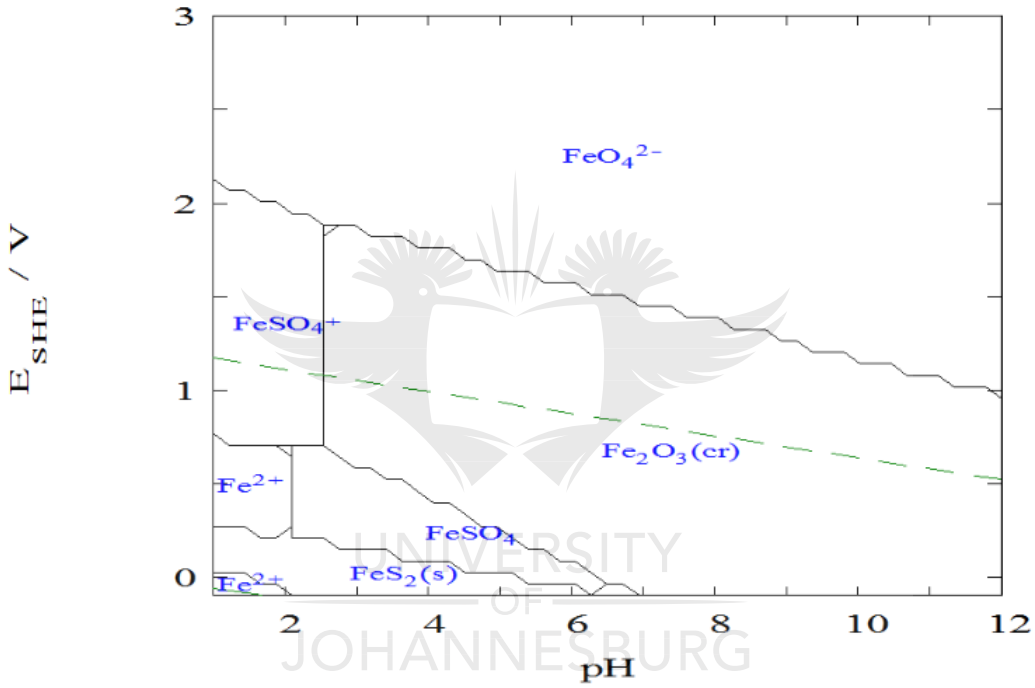

Figure 18: Pourbaix diagram showing the behaviour of mild steel in MME bulk solution

Figure 18 and Figure 19 shows the thermodynamical behaviour of mild steel in MME/SSW solution. The E-pH diagram results for MME PSS studies showed that without any surface protection, the Fe on the steel surface will passivate as FeS_2 corrosion film, which reduces CR. This steel-MME electrolyte reaction is caused by an oxidation redox potential ranging from 0.485 V (24 hours) to 0.379 V (after 192 hours), at 1.920 pH value. Underflow condition the oxidation potential increased to 0.497 V, which reduced the surface Fe to Fe^{2+} ions. Thus, the CR is high and there is no corrosion product film to reduce the effects.

The E-pH diagram results for mild steel in SSW bulk solution show oxidation of Fe to $Fe_2O_3(cr)$ the precipitate, irrespective of flow conditions or exposure time. Such behaviour yields lower the CR, as Fe_2O_3 has a semi-permeability property.

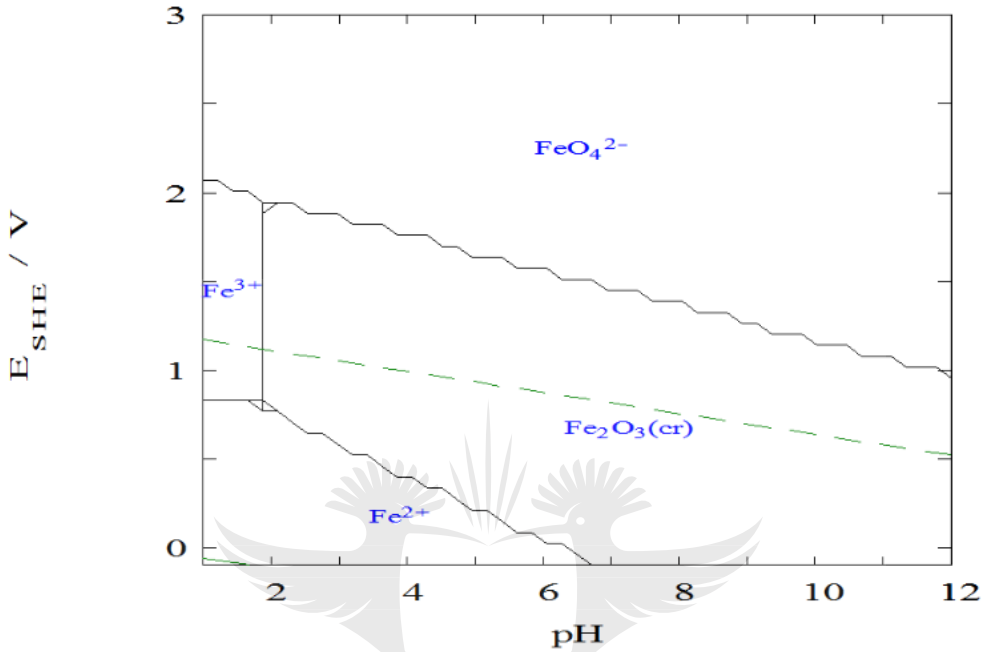

Figure 19: Pourbaix diagram showing the behaviour of mild steel in SSW bulk solution

4.3.3. Leachate Characteristics

The dissolution tests were conducted on the MME and SSW solutions after corrosion exposure, to determine the kinetics of the dissolution during PSS and PFL conditions. Figure 20 summarises the dissolution of Fe and Ca in the MME/SSW electrolyte.

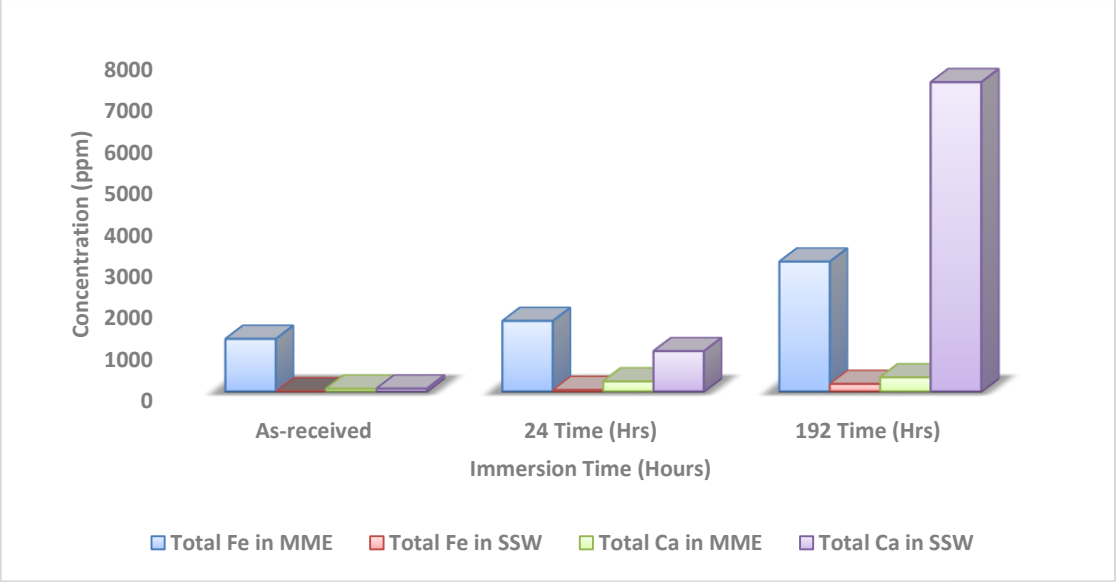

Figure 20: The kinetic behaviour of Fe and Ca dissolution under pipeline flow loop (PFL).

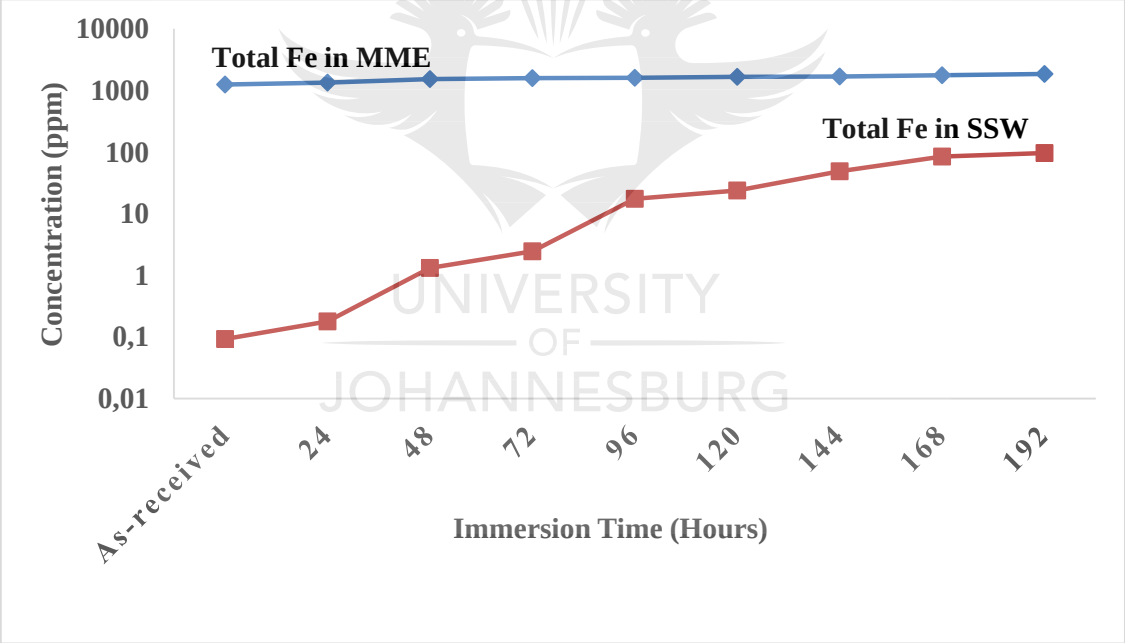

Figure 21: The kinetic behaviour of Fe dissolution under the pseudo-steady state (PSS)

Figure 20 and Figure 21 supported the thermodynamical behaviour in Section 4.3.1 by firstly showing that Fe dissolves more in MME solution than in SSW solution. Secondly, by showing a high concentration of Ca^{2+} ion with exposure time for SSW solution. Because Ca^{2+} ions, together with Mg^{2+} ions promote a rapid formation of a protective corrosion film. Based on the Fe dissolution results, the precipitation kinetics

which facilitates the formation of the multi-layered corrosion film favours bulk solution with high pH levels.

4.4. Conclusion

The following conclusion has been obtained from the pre-and post-test evaluation characterization of mild steel and the chemical properties of MME/SSW electrolyte.

1. SSW bulk solution is characterized as a flow-non-sensitive condition, which will favour low CR because of a pseudo-passive scale film on the surface.

    - The fact that CR was inversely proportional to pH indicates that the H^+ ions in SSW solution directly influenced the kinetics of the electrochemical reaction. The ions, however, did not facilitate corrosion mechanism through mass-transfer.

2. MME bulk solution is characterized as flow-sensitive conditions, which will encourage high CR.

3. The presence of Cl^- and SO_4^{2-} ion will exacerbate the CR by lowering the electrical resistivity of the corrosion cell, which resulted in the breakdown of the pseudo-passivation film. Ca^{2+}ion and Mg^{2+} ion, on the other hand, is expected to increase the formation of the surface corrosion film in SSW solution.

4. The reduction of oxygen in solution is another major reaction governing corrosion mechanism. At high concentration, the oxygen tends to polarize the Fe, which lowers CR by forming iron oxide corrosion film on the surface. Whilst at low oxygen concentration the corrosion mechanism dependent on both H^+ion concentration and counter-ions present.

CHAPTER FIVE

SPECTROSCOPIC CHARACTERIZATION

5.1. Spectroscopic Characterization

To support this study, a series of surface spectroscopic test, which included Optical micrography, SEM, EDX, XRF and XRD were performed according to specifications highlighted in Chapter Three, to study the surface morphology of the working electrode (mild steel) before and after corrosion exposure, together with their respective corrosion product. Gwyddion software was used to interpret SEM/EDX results.

5.1.1. Surface Analyses

5.1.1.1. Optical micrography of as-received mild steel sample

(a)

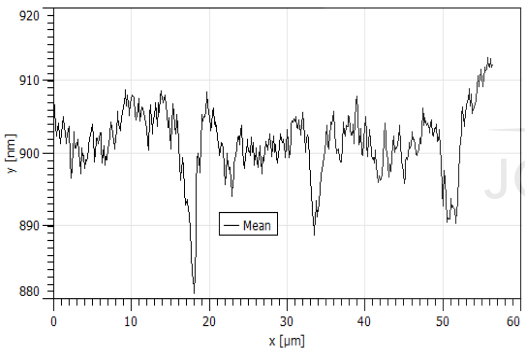

(b)

(c)

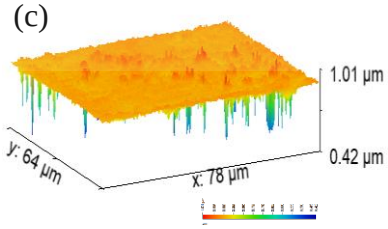

(d)

Element	Weight%	Atomic%	Compd%	Formula
Al K	0.30	0.40	0.57	Al2O3
Si K	0.24	0.31	0.52	SiO2
S K	0.80	0.88	1.99	SO3
Cl K	3.01	3.00	0.00	
Fe K	65.91	41.73	84.79	FeO
Cu K	7.28	4.05	9.12	CuO
O	22.45	49.63		
Totals	100.00			

Figure 22: Metallography of the as-received mild steel sample, with a topographical overview. 100X Magnification.

In the as-polished condition, the mild steel coupon sample showed evidence of non-metallic inclusions (gas – and - solidification inclusions) on the substrate, which are harmful to the mechanical integrity of the steel and corrosion properties, profile from multiple images is shown in Figure 22. The presence of such surface inclusions are

documented by Ozhigov, et al. (2017) to instigate pit corrosion. Figure 22 (a) and (c) shows the topographical results of the as-received specimen, generated from Gwyddion software. The average surface roughness was recorded as 0.902 ± 0.007 µm, with a surface thickness profile of ~ 912 nm. Such high roughness was attributed to the heavy presence of non-metallic inclusions of which some propagated to ~ 890 ~ 880 nm depth.

5.1.1.2. Micrographic characterization of mild steel immersed in MME solution for 192 hours under Stagnant Flow conditions.

(a)

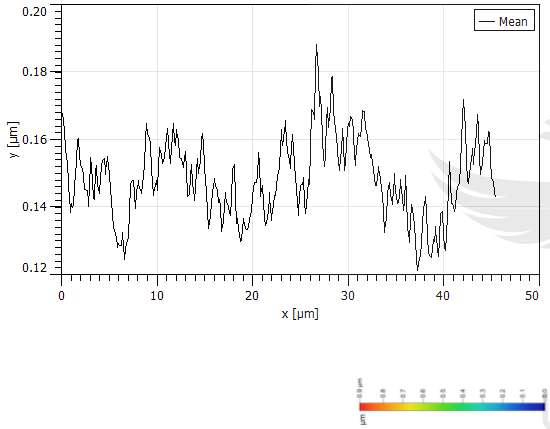

(b)

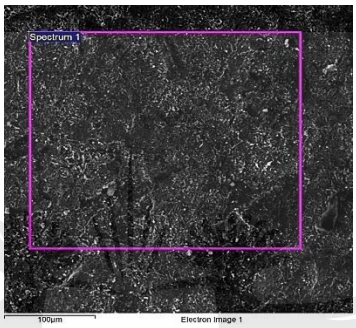

(c)

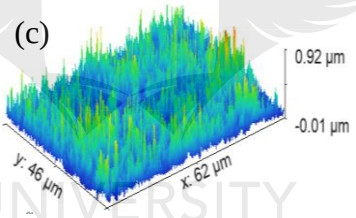

(d)

Element	Weight%	Atomic%
O K	21.810	48.920
Mg K	0.610	0.900
Al K	0.340	0.460
S K	3.100	3.470
Cl K	0.570	0.580
Ca K	0.400	0.360
Mn K	0.310	0.200
Fe K	51.050	32.800
Cu K	21.810	12.320
Total	100.000	

Figure 23: Microstructure characterization of mild steel with multi-layered corrosion film after 192 hours in PSS MME solution shows (a) Surface profile (thickness); (b) Corrosion product layer on the surface; (c) 3D SEM/EDX image; (d) Elemental composition of the corroded surface.

Figure 23 shows a surface profile from multiples image of 192H MME study on a coupon sample having distinct loose granules of corrosion product layer consisting mainly of iron oxide and, iron sulphides. This multifaceted phenomenon is characterized by a high corrosion current density (I_{corr}). The average surface roughness decreased to 148.400 ± 11.600 nm because the surface was submerged with loose corrosion layer. Surface thickness is recorded as ~ 0.140 µm, with protrude reaching the heights of 0.920 µm.

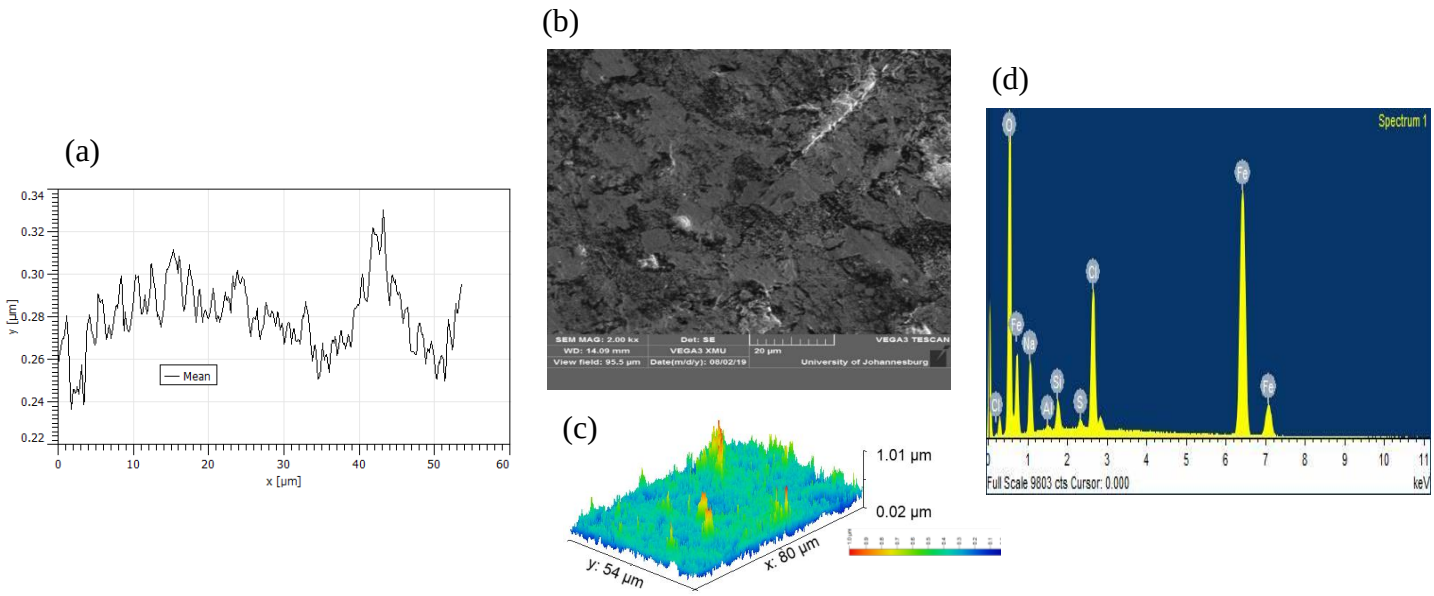

Figure 24: Microstructure characterization of mild steel without corrosion film after 192 hours in PSS MME solution shows (a) Surface profile (thickness); (b) Corrosion product layer on the surface; (c) 3D SEM/EDX image; (d) Elemental composition of the corroded surface.

Figure 24 shows a surface profile from multiples image of 192H MME study after the specimen was washed and dried (to remove the multi-layered corrosion film). In the as-cleaned condition, a predominance of multiple wear tracks - grooves, gullies, waves, and pinholes are evident on the surface. The average surface roughness slightly increased to 279.800 ± 16.010 nm once the loose corrosion film was removed. Surface thickness was ~ 0.280 µm, with detached metal wearing to ~ 0.240 µm surface level. The 3D SEM/EDX image shows a higher stress concentration, with protrusions of 1.010 µm. The EDX results showed evidence of chloride, oxide, sodium and sulfide element on the corroded surface.

5.1.1.3. Micrographic characterization of mild steel immersed in SSW solution for 192 hours under Stagnant Flow conditions.

(a)

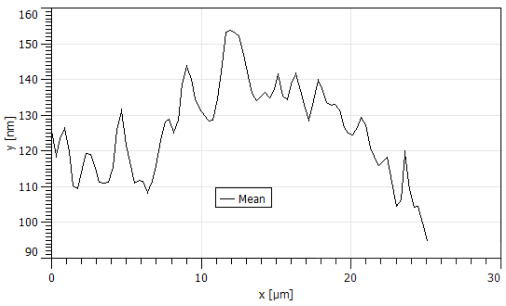

(b)

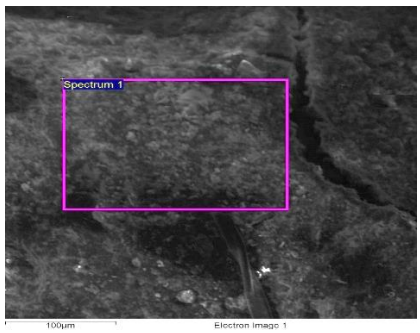

(c)

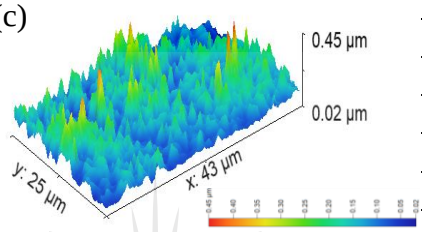

(d)

Element	Weight%	Atomic%
Na K	12.550	15.610
Mg K	1.710	2.020
Al K	0.220	0.230
Si K	5.600	5.710
S K	0.280	0.250
Cl K	14.360	11.580
K K	0.270	0.200
Ca K	1.540	1.100
Mn K	2.920	1.520
Fe K	33.540	17.170
Cu K	0.610	0.270
Zn K	2.120	0.930
O	24.290	43.420
Total	100.000	

Figure 25: Microstructure characterization of mild steel with multi-layered corrosion film after 192 hours in PSS SSW solution shows (a) Surface profile (thickness); (b) Corrosion product layer on the surface; (c) 3D SEM/EDX image; (d) Elemental composition of the corroded surface.

Figure 25 shows a surface profile from multiples image of 192H SSW study on a coupon sample having a semi-permeable compact coral-like corrosion film, which impedes CR. Observation of a cracked corrosion product film (release stored energy) is most likely to have resulted from the interaction between the surface and the Ca^{2+}ions in some area resulted in precipitation calcium carbonate ($CaCO_3$) which is known to breakdown the corrosion film with immersion time, especially in the presence of aggressive ions such as Cl^-, SO_4^{2-} and other inhibiting HCO_3^- ions (Tlili, et al., 2006; Parakala, 2005). Such reaction governs a growing competition between existing corrosion product and newly precipitated corrosion product, compressively stressing the layer as the two crystals pushing against one another. The breakdown of the multi-layered corrosion film is likely to instigate localized corrosion. However, in an H_2CO_3 system, the semi-passive layer will be restored sometime after breaking down. At this point, the undermining corrosion rate (CR) was low, and the precipitation rate or scale formation rate was relatively high. Hence a low average surface roughness of 126.800

± 12.700 nm. The surface thickness was ~ 155 nm, whilst the depth of the cracked film (pores) was < 95 nm. The 3D SEM/EDX image shows a lower stress concentration, with protrusions of 0.450 µm.

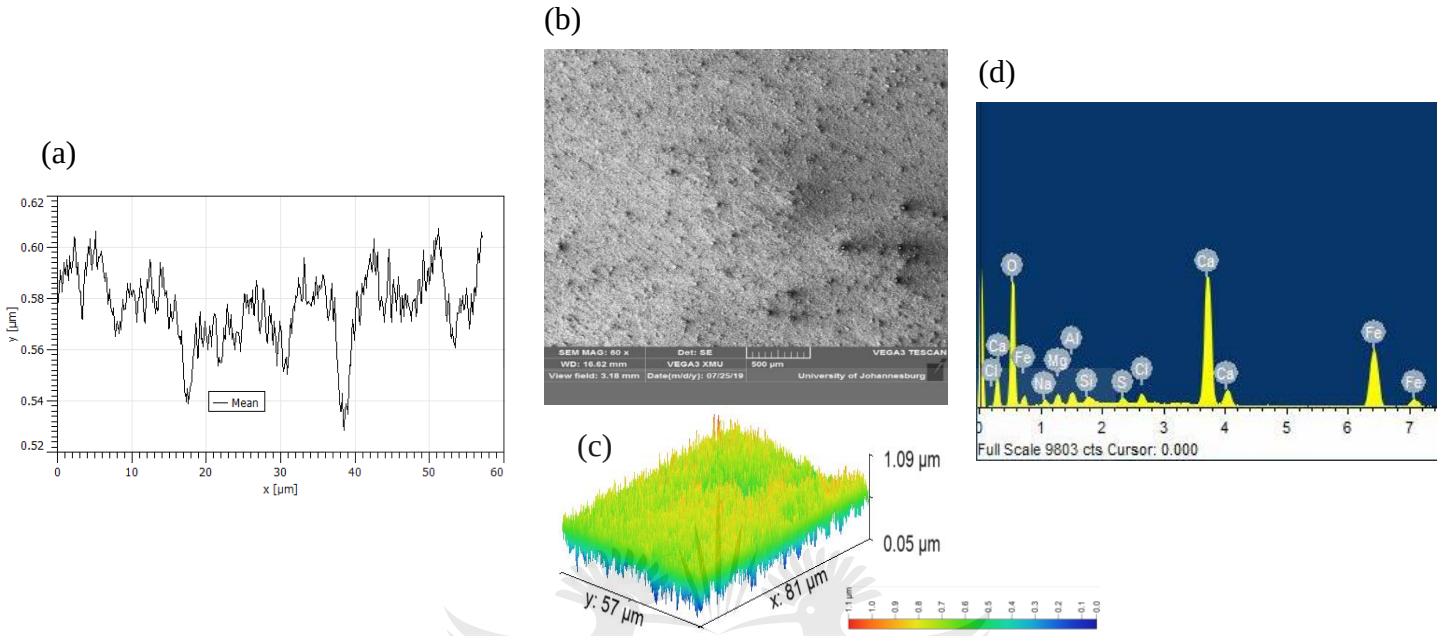

Figure 26: Microstructure characterization of mild steel without corrosion film after 192 hours in PSS SSW solution shows (a) Surface profile (thickness); (b) Corrosion product layer on the surface; (c) 3D SEM/EDX image; (d) Elemental composition of the corroded surface

Figure 26 shows a surface profile from multiples image of 192H SSW study after the specimen was washed and dried. In the as-cleaned condition, a predominance of coarsening surface and pinhole like inclusion was observed. Such occurrence resulted in 0.584 ± 0.014 µm average surface roughness. The surface thickness decreased to ~ 0.600 µm, with pinhole like inclusions propagating as deep as ~ 0.530 µm. The 3D SEM/EDX image shows a moderate stress concentration, with protrusions as high as 1.090 µm. The EDX results showed evidence of chloride, oxide, calcium, silicon, magnesium, aluminium and sulfide element on the corroded surface.

5.1.1.4. Micrographic characterization of mild steel in MME/SSW solution during PFL conditions.

The surface profile from multiples image of MME/SSW bulk flow study before and after the specimen was washed and dried are shown in Appendix B from Figure 38 to Figure 61.

For 24H MME study, the multi-layered corrosion film appeared to dissolve by flow and the development of hydrostatic pressure acting at that point. The average surface roughness increased to 194.700 ± 10.140 nm (with corrosion film) after the surface was washed the average surface roughness increased to 288.900 ± 18.370 nm. Significant material detachment (wear track) was observed at position 2 (bend) – surface thickness decreased from 0.300 µm to 0.210 µm. Cu, Cl, S, O, Fe and Al were the bulk elements observed on the corroded surface. At position 3, the coupon sample was disintegrated by what appears to be layer-type corrosion.

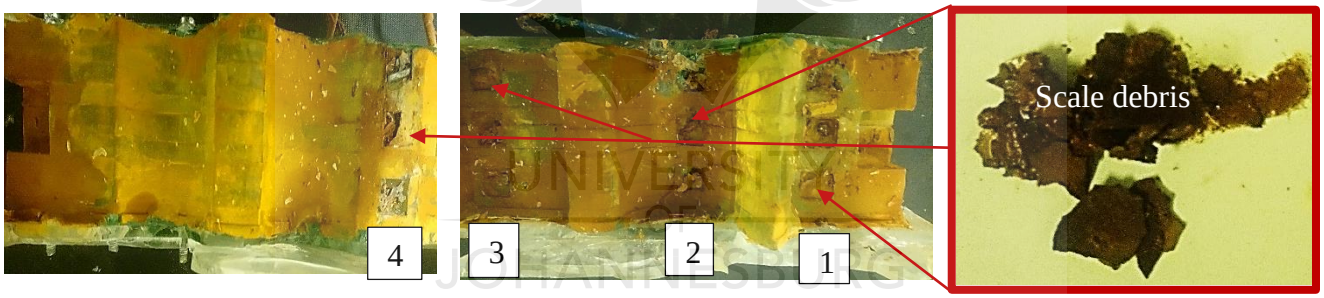

Figure 27: Disintegration of mild steel coupon sample during 192H MME bulk flow

Visual observation of 192H MME study is shown in Figure 27. As shown, there were no samples found inside the test-rig at all four positions. However, there was a heavy presence of scale debris in the form of large corrosion scale layers inside the reservoir. And as such, no results were obtained for 192H MME bulk flow.

For flow non-sensitive condition, the average surface roughness appeared to coincide with the flow. Pit growth is another anomaly that might have resulted in much higher roughness. Accept at the bent were the high average surface roughness was as a result of what is hypothesized to be direct impingement. Nonetheless, the average surface roughness decreased with exposure time, such occurrence is suspected to be as a result

of pit arrest. Ca, Mn, Cl, S, O, Cu, Fe, Al, P and Si were the bulk elements observed on the corroded surface.

5.2. XRF Results

Table 4: Bulk elemental composition of corrosion product produced when mild steel interacts with MME solution

Elemental Composition	Fe_2O_3	CaO	K_2O	Cl	SO_3	SiO_2	Al_2O_3	C	H_2
Concentration (ppm)	877510	5250	480	260	107500	3120	2240	1647	38609

Table 4 shows the chemical composition of the corrosion product collected in the MME solution after 192 hours of exposure.

Table 5: Bulk elemental composition of corrosion product produced when mild steel interacts with SSW solution

Elemental Composition	Fe_2O_3	CaO	MnO	Cl	SO_3	SiO_2	Al_2O_3	C	H_2
Concentration (ppm)	954220	8680	2560	1340	5050	6010	7450	48239	14800

Table 5 shows the chemical composition of the corrosion product collected in the SSW solution after 192 hours of exposure.

5.3. XRD Results

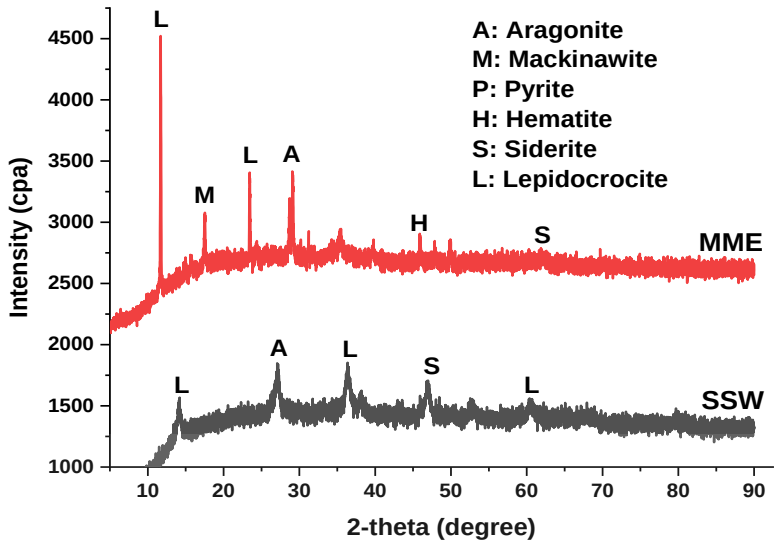

Figure 28: XRD pattern of corrosion product collected from MME/SSW solution

Figure 28 shows the XRD patterns for mild steel sample during 192H MME/SSW bulk flow study. The elemental composition of the corrosion products collected after 192H MME bulk flow show that the corrosion crystal's orientation is isotropic. The XRD pattern indicates the diffraction peak of mainly Fe_2O_3, FeS_2, FeO(OH) and FeS. The presence of FeO(OH) in the corrosion product suggest that H_2S has a significant effect on the redox reaction. The variety of iron sulphide corrosion product indicates the superiority of H_2S to precipitate on the surface as compared to $FeCO_3$.

The SSW figure shows a peak pattern for 192H SSW corrosion product. The XRD pattern indicates the diffraction peak of mainly $FeCO_3$, and FeO(OH). The multiple peaks could probably be due to the density of the corrosion products on the steel surface. Alongside MME/SSW corrosion product, an agglomeration of $CaCO_3$ (aragonite) crystal was found blended with the corrosion film. According to Möller (2007) presence of Mg^{2+}ions in solution cause $CaCO_3$ to precipitate on the surface as aragonite. The aragonite crystal momentarily reduced the CR by physically separates the metal surface from the electrolyte until the weak crystal influence the breakdown of the multi-layered corrosion film.

CHAPTER SIX

COMPARISON OF CORROSION EVALUATION DURING PSEUDO-STEADY STATE AND PIPELINE FLOW LOOP CONDITIONS

6.1. Introduction

The following chapter respectively discusses the behaviour of mild steel in MME and SSW solutions, during pseudo-steady state (PSS) and pipeline flow loop (PFL) conditions. This section starts by discussing the gravimetric results (baseline test), then followed by an electrochemical study of mild steel during PFL, and lastly a flow parameter, to validate the PDP and EIS findings during FIC.

6.2. Gravimetric Characterization

Figure 29 shows the gravimetric results respectively obtained from MME/SSW during a PSS flow. As predicted by the pre-and post-test assessment in Chapter Four, gravimetric results showed that MME solution had a high CR as compared to the SSW solution. The MME curve showed a constant increase in the CR with immersion time, as a result of Fe precipitating as $FeSO_4^{\dagger}$ by-product. This corrosion mechanism is characterized by a lack of corrosion film to polarize the surface.

The SSW curve in Figure 29 shows a decrease in CR with immersion time. This corrosion mechanism indicates that there was a physical layer separating the metal surface from the electrolyte. For the reason that carbon steel does not passivate, the semi-porous corrosion film grows with immersion time. Figure 29 further shows that the SSW CR exhibited four distinct stages. The CR decreases quickly at the beginning, and changes slowly, and then gains momentum, before finally slows down. According to Jasinski (1987) and de Moraes, et al (2000) such behaviour is attributed to the evolution of carbonic corrosion film such as iron carbonate (siderite, $FeCO_3$) and lepidocrocite FeO(OH) on the surface with time.

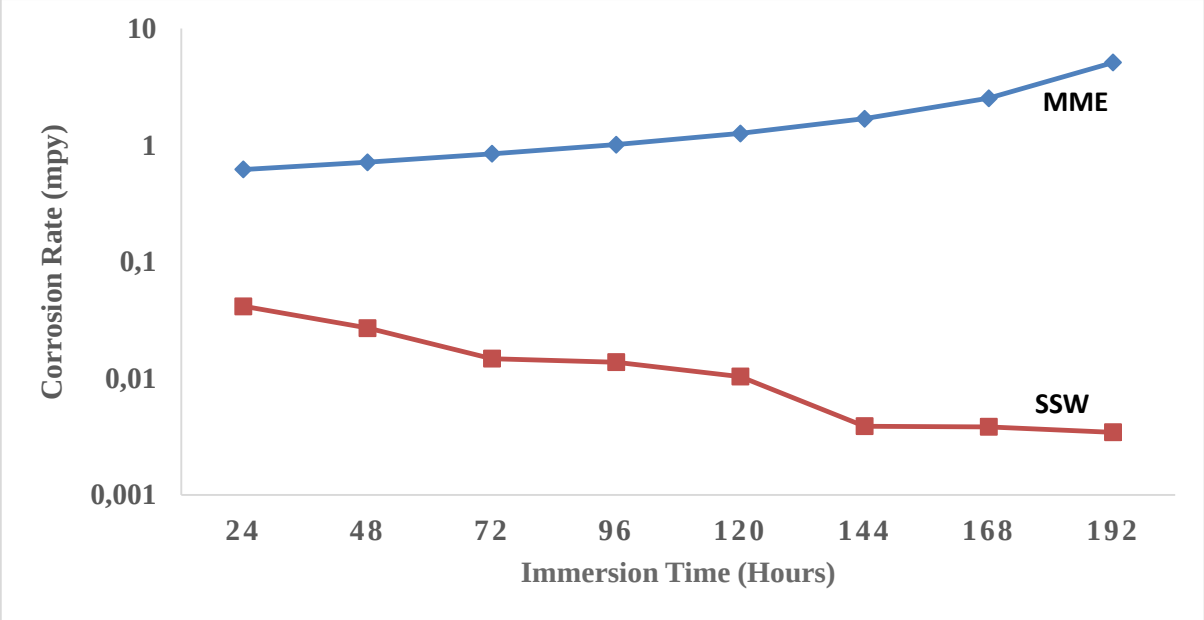

Figure 29: The gravimetric experiment showing corrosion rate plotted against immersion time for mild steel in MME/SSW during PSS.

6.2.1. Immersion Time

Table 6 shows the behaviour of mild steel with immersion time. The obtained immersion results showed that metal loss increased with immersion times due to MME/SSW solution conductivity increase. This phenomenon increases the flow resistance of the solution, which in turn lowers the SSW CR at the high concentration by decreasing ion(s) mobility. The immersion time results coincide with gravimetric results, Equation 46 shows the mathematical method used to determine gravimetric trials.

The MME immersion results showed that the steel substrate was unprotected throughout the 192 hours, especially after the 144 hours. The inferior corrosion product (siderite ($FeCO_3$), lepidocrocite (FeO(OH)), hematite (Fe_2O_3), mackinawite (FeS), and pyrite (FeS_2)) associated with MME solution are semi-conductive and have insubstantial adhesion properties (Malik, 1995). The steep peak observed on the MME curve in Figure 29 is hypothesized to be evidence of the breakdown of the multi-layered corrosion film which is most likely to occur when the multi-layer film reaches a critical value.

Table 6: The metal loss behaviour during immersion test

	MME		SSW	
Hours	Weight Loss (g)	Corrosion Rate (mpy)	Weight Loss (g)	Corrosion Rate (mpy)
24	0,101	0,621	0,049	0,042
48	0,200	0,715	0,062	0,027
72	0,300	0,844	0,074	0,015
96	0,348	1,011	0,083	0,014
120	0,417	1,262	0,099	0,010
144	0,458	1,690	0,124	0,004
168	0,561	2,530	0,318	0,004
192	0,675	5,129	0,590	0,003

6.3. Electrochemical Results

Potentiodynamic polarization (PDP) and Electrochemical impedance spectroscopy (EIS) were studied to gain insight into the corrosion behaviour of mild steel during MME/SSW pipeline flow loop. The polarization curves for MME 192H flow were, however, not generated because the coupon samples disintegrated entirely sometime after 24 hours. All the potential measurements were quantified in agreement to Saturated Calomel Electrode (SCE). The Nyquist plot, on the other hand, was used to study the scaling behaviour during FIC.

6.3.1. Electrochemical results for the mild steel coupon samples at position 1 within the test rig

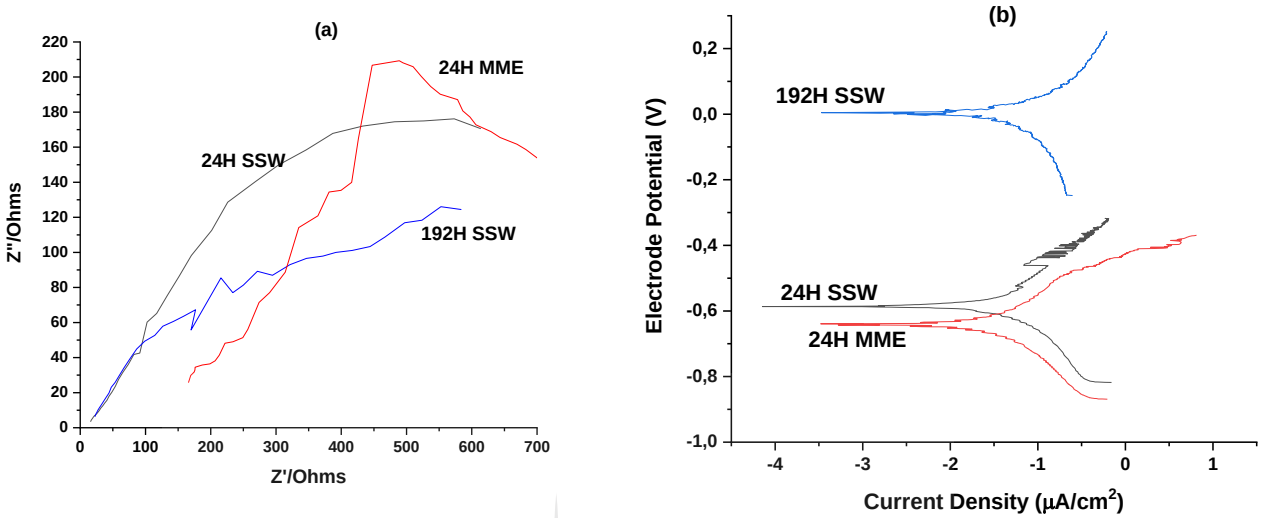

Figure 30: Nyquist (a) and Tafel (b) behaviour of mild steel at position 1 during MME/SSW bulk flow

Figure 30 (a) shows Nyquist plot results for mild steel at position 1 - characterized by 0.062 m/s flow rate and hydrostatic pressure of 0.027 bar. From the Figure, it can be observed that the Nyquist plot was a depressed semicircle for all tests conducted at position 1. The higher the electrical impedance (Z) the denser the corrosion film (the higher the ability of the electrochemical cell to resist current flow). The excessive solution resistance (the point where the curve meets the X-axis at the high frequency) and the small charge transfer resistance (the area under the curve characterized by low frequency) limits polarization resistance, and hence the MME solution is expected to experience high CR, even at high impedance. The polarization resistance which accounts for the kinetics of the electrochemical reaction is mathematically expressed as $R_p = R_3 + R_2$. Hence,

- The 24H SSW experiment showed an R_p value of 949.41 Ohm with 7.758 mpy corrosion rate.
- The 24H MME experiment showed an R_p value of 721.6 Ohm with 10.404 mpy corrosion rate, and
- 3.542 mpy for 192H SSW experiment with an R_p value of 1459.800 Ohms.

The change in corrosion mechanism from charge to mass transfer or diffusion-controlled can be comprehended by the change in the shape of the Nyquist plot. As proven by gravimetric results such behaviour was encouraged by the formation of Fe_2O_3, FeS_2, FeO(OH) and FeS multi-layer film which facilitates flow-sensitive condition due to poor adhesive properties. And thus, resulting in a 0.363 ± 0.021 µm surface roughness. The decrease in electrical impedance (Z) with SSW exposure time was attributed to an increase in corrosion product charge transfer (a_3). Unfortunately, the slight increase in constant phase element (Q_3) from $0.607e^{-3}$ F to $2.314e^{-3}$ F with time means that the multi-layered corrosion film was semi-permeable. Hence, the CR decreased to 3.542 mpy.

Table 7: Nyquist parameters for the dissolution of mild steel at position 1 during MME/SSW bulk flow

Sample	R_1 (Ohm)	Q_1 F. s^(a · 1)	a_1	R_2 (Ohm)	Q_3 F. s^(a · 1)	a_3	R_3 (Ohm)
24H SSW	10.970	$0.232e^{-3}$	0.461	40.910	$0.607e^{-3}$	0.465	908.500
24H MME	144.300	$0.137e^{-3}$	0.406	614.800	$51.260e^{-6}$	1	106.800
192H SSW	14.180	$0.247e^{-3}$	0.425	311.800	$2.314e^{-3}$	0.854	1148

Because the equivalent electrode circuit (EEC) corresponds to the electrochemical properties of the coupon sample during corrosion attack, an EEC was used to interpret the EIS measurement; results are shown in Table 7. The slight change in SSW charge transfer resistance (R_1) with exposure time substantiates for the stability of this test. The Nyquist parameters (Table 7) showed that the charge transfer resistance (R_3) increased with SSW exposure time. The high R_3 value indicates that the dissolution of mild steel occurred at a lower rate. The (a) factor was near unity, hence the formed semi-permeable corrosion film behaved like a capacitor - CR decreased with exposure time. The 154.100 ± 16.640 nm average surface roughness, inhomogeneous surface

reaction rates and non-uniform current distribution were supported by Figure 30 (b) which showed a noisy part adjacent to the end of the 24H SSW polarisation curves. Thus, the current fluctuations were evidence of pitting, which obstructed the charge transfer during the experiment.

For MME study, the EIS results did not give an obvious reason for the high CR. The EIS results did, however, show that the (a) factor did not act as a capacitor. The behaviour was attributed to a low polarization resistance and low Q_3 of $51.260e^{-6}$ F which resulted in clustering of loose granules corrosion film ($FeCO_3$, FeO(OH), $CaCO_3$, Fe_2O_3, FeS, and FeS_2), with weak adhesive properties. An a_3 value of 1 suggests that the surface electrode capacitance (SEC) was equivalent to the ideal capacitance, which was not the case, considering that the there was substantial corrosion rate (CR) during 24H MME/SSW experiments.

Table 8: Tafel parameters for the dissolution of mild steel at position 1 during MME/SSW bulk flow

Sample	E_{corr} (mV)	I_{corr} ($\mu A/cm^2$)	β_a (mV)	β_c (mV)	CR (mpy)
24H SSW	-586.705	17.191	93.400	77.300	7.758
24H MME	2.194	23.054	78.800	107.300	10.404
192H SSW	-642.249	7.849	47.600	44.900	3.542

Figure 30 (b) shows anodic and cathodic polarization behaviour of mild steel coupons at Position 1. The dominance of anodic Tafel slope (β_a) - 93.400 mV during 24H SSW study shows that the corrosion mechanism was governed through mass transfer. With lengthier exposure time, β_a decreased to 47.600 mV (which is not far from cathodic Tafel slope (β_c)), such behaviour signifies that the corrosion mechanism has now controlled through mass-charge transfer. Hence, the SSW PDP results showed an increase in the magnitude of corrosion potential (E_{corr}) with time from - 586.705 mV (SCE) to - 642.249 mV (SCE), which increased the metal resistance (R_2). And thus, decreasing the corrosion current density (I_{corr}) from 17.191 $\mu A/cm^2$ to 7.849 $\mu A/cm^2$, results shown in Table 7. The dominance of β_c during 24H MME PDP study shows that the corrosion mechanism was controlled through charge transfer. Because the R_p

value was low (evident by localized corrosion film), the E_{corr} value was low - 2.194 mV. Hence, the high I_{corr}.

6.3.2. Electrochemical results for the mild steel coupon samples located in position 2 within the test rig

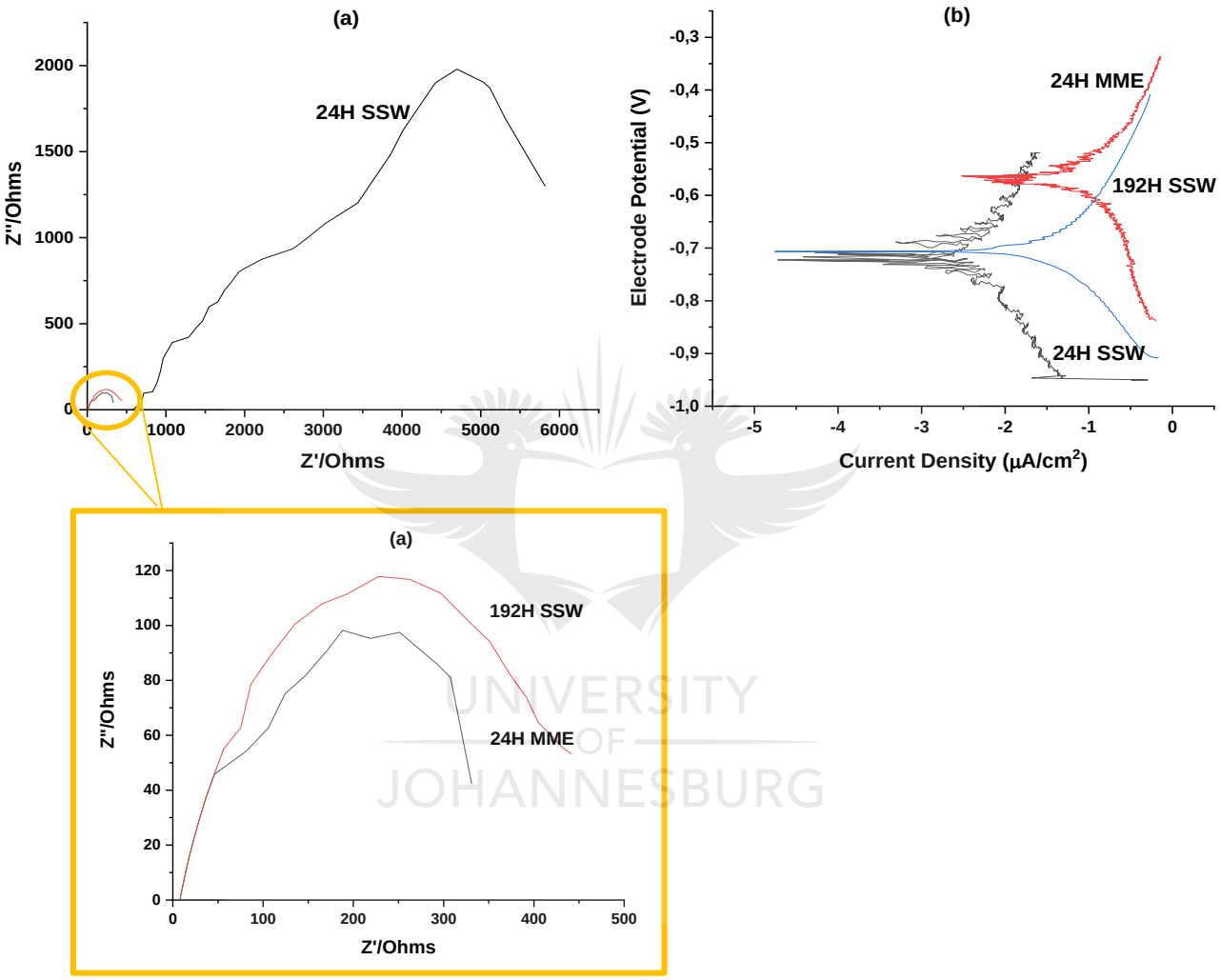

Figure 31: Nyquist (a) and Tafel (b) behaviour of mild steel at position 2 during MME/SSW bulk flow

Figure 31 (a) shows the results of the Nyquist plot for mild steel at position 2, characterized by 0.018 m/s flow rate and hydrostatic pressure of 0.026 bar. Similar to Figure 30 (a), the Nyquist plot at 180^{o} pipe return bend (position 2) was a depressed semicircle which decreased with exposure time. Polarization resistance (accumulation

of the frequency read from the X-axis) appeared to decrease with exposure time, hence, corrosion rate (CR) increased with time.

Table 7 showed that R_3 decreased with SSW exposure time which explains the increase in CR with exposure time. The constant phase element (Q_3) was determined to increase from $64.390e^{-6}$ F to $0.307e^{-3}$ F, which characterized the stored charge during corrosion. Thus, the higher the Q_3 value, the porous the corrosion film which subsequently increases corrosion rate (CR). This behaviour is supported by a drastic increase in a_1 with exposure time demonstrations a significant metal loss on the steel surface. Factor (a) did not behave like a capacitor because of the vortex generated at the bent. Such behaviour is associated with direct impingement corrosion (DIC) or erosion of the multi-layered film during bulk flow, as shown by a decreasing a_3 value.

The small, depressed 24H MME curve showed a low R_3 value, which explains the high CR. Although the (a) factor was not far from unity, the formed weak corrosion film did not behave like a capacitor. As a result of low polarization resistance and high porosity of the multi-film (as shown by high Q_3 value) – localized weak corrosion film.

Table 9: Nyquist parameters for the dissolution of mild steel at position 2 during MME/SSW bulk flow

Sample	R_1 (Ohm)	Q_1 F.s^(a · 1)	a_1	R_2 (Ohm)	Q_3 F.s^(a · 1)	a_3	R_3 (Ohm)
24H SSW	710	$0.119e^{-3}$	0.419	18597	$-64.390e^{-6}$	0.756	1080
24H MME	47.080	$0.645e^{-6}$	0.708	312	$0.482e^{-3}$	0.600	265.100
192H SSW	7.906	$12.340e^{-6}$	0.879	3.367	$0.307e^{-3}$	0.563	463.300

Table 10 showed an increase in I_{corr} with exposure time from 4.094 $\mu A/cm^2$ to 9.917$\mu A/cm^2$, due to a decrease in R_1. The low 24H SSW CR of 1.848 mpy was caused by a high impedance of < 2000 ohm and high polarization resistance of 19677 ohms. This behaviour resulted in a high E_{corr} and a relatively low i_{corr}, as indicated by a high

charge transfer (R_3). The dominance of 378.900 mV (SCE) cathodic Tafel slope (β_c) over 85.100 mV (SCE) anodic Tafel slope (β_a) during 24H SSW indicates that the corrosion mechanism was governed through a charge transfer. After 192 hours in SSW solution, the decrease in β_c facilitated the change in corrosion mechanism from charge transfer to mass-charge transfer. Hence, the decrease in a_1 with SSW exposure time, charge transfer (R_3) which was in proximity to polarization resistance and inturn increasing CR to 4.476 mpy. Such an effect increased the average surface roughness to 326.100 ± 35.290 nm.

The coupon samples exposed to MME bulk flow for 24 hours generated excessive CR of 18.068 mpy because of moderate polarization resistance (577.100 ohms) having a high porosity of $0.482e^{-3}$ F. This behaviour was governed by the dominance of β_c during 24H MME study which facilitated hydrolysis through charge transfer. Hence, the E_{corr} was low - 558.477 mV (SCE) and the I_{corr} was high - 40.035 $\mu A/cm^2$. This phenomenon resulted in 312.700 ± 26.390 nm increase in average surface roughness. The angle at which the MME/SSW bulk flow strikes the coupon sample was also found to limit polarization resistance on the surface. Therefore, the formation of the pseudo-passivation film through a vortex created when the bulk solution change directly which erodes the multi-layered corrosion film. Such effect inhibits the development of the corrosion film.

Table 10: Tafel parameters for the dissolution of mild steel at position 2 during MME/SSW bulk flow

Sample	E_{corr} (mV)	I_{corr} ($\mu A/cm^2$)	β_a (mV)	β_c (mV)	CR (mpy)
24H SSW	-692.838	2.271	85.100	378.900	1.848
24H MME	-558.477	40.035	85.700	105.500	18.068
192H SSW	-705.866	9.917	58.200	47.200	4.476

6.3.3. Electrochemical results for the mild steel coupon samples located in position 3 within the test rig

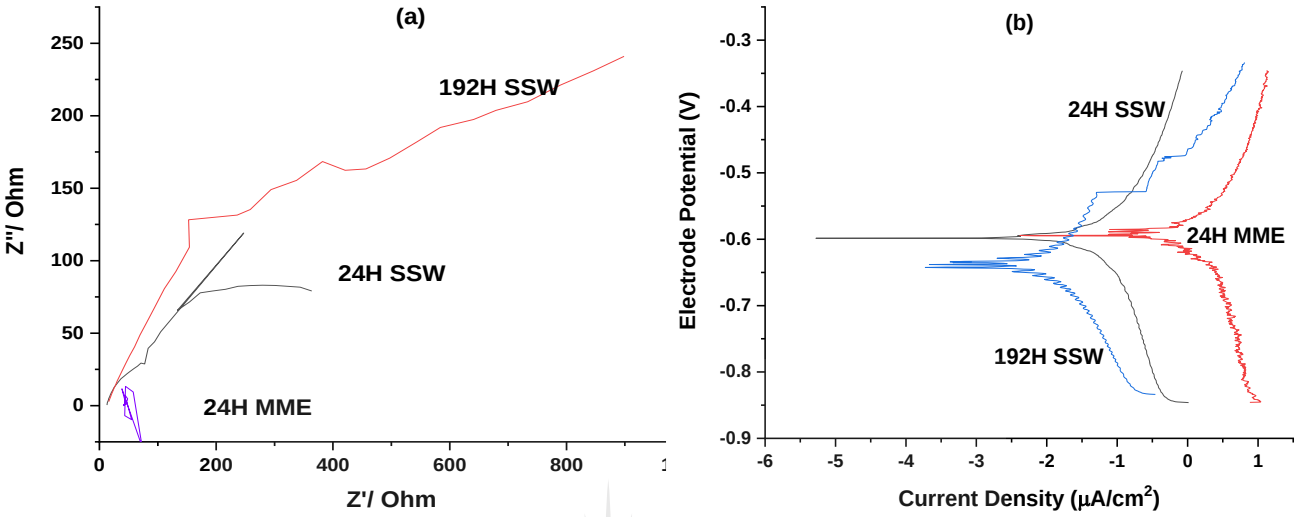

Figure 32: Nyquist (a) and Tafel (b) behaviour of mild steel at position 3 during MME/SSW bulk flow

Figure 32 (a) shows the results of the Nyquist plot for mild steel at position 3, characterized by 0.116 m/s flow rate and hydrostatic pressure of 0.028 bar. From the figure, it can be observed that the Nyquist plot at position 3 was a depressed semicircle which increased with SSW exposure time. The reason(s) for such behaviour is discussed along the following sections. The Nyquist plot for 24H MME was erratic because the coupon sample disintegrated during flow, and the Potentiostat reading (EIS and PDP) was picking up the electrochemical activities of a worn-out sample, the evidence is shown in Figure 51.

The EIS results showed that with time R_3 increased from 300.900 Ohm to 555.300 Ohm which decreased CR with SSW exposure time. The increase in a_3 with SSW time signifies that there was a barrier which hindered the movement of the ion between the metal and the electrolyte. The significant decrease in Q_3 from $0.526e^{-3}$ F to $22.210e^{-15}$ F shows impermeability of the multi-layered corrosion film. Hence, a significant decrease in dissolution rate with time. The impermeability of this multi-layered film was supported by an (a) Factor which was not too far from unity, such behaviour indicates that corrosion film acted as a capacitor. The high dissolution rate

experienced during the 24H SSW experiments was attributed to the excessive flow rate; results are shown in Table 11. This behaviour results in a 0.423 ± 0.013 µm average surface roughness.

Table 11: Nyquist parameters for the dissolution of mild steel at position 3 during MME/SSW bulk flow

Sample	R_1 (Ohm)	Q_1 F.s^(a · 1)	a_1	R_2 (Ohm)	Q_3 F.s^(a · 1)	a_3	R_3 (Ohm)
24H SSW	10.550	$4.854e^{-18}$	0.140	0.752	$0.526e^{-3}$	0.469	300.900
24H MME	41.790	0.018	0.512	$0.325e^{-15}$	$54.350e^{-87}$	1	6.874
192H SSW	12.970	$0.212e^{-3}$	0.499	780.700	$22.210e^{-15}$	0.724	555.300

Figure 32 and Table 12 shows the PDP results for mild steel at position 3. The results of the 192H SSW PDP curves shows the polarization of a tenacious coral-like FeO(OH) and $FeCO_3$ corrosion film(s) on the steel surface at - 0.530 v (SCE) and - 0.470 v (SCE) potential (E). The formation of the tenacious multi-layered corrosion film during SSW study is demonstrated by an increase in polarization resistance (from 301.652 ohms to 1336 ohm) and electrical impedance (Z) with time. The high 24H SSW CR was governed by the dominance of β_c - charge transfer limit. Whilst a low 192H SSW CR was facilitated by the dominance of electrical impedance (β_a) – mass transfer. The evolution of β_c and β_a with time increased the magnitude of the E_{corr} from -597.625 mV (SCE) to -641.310 mV (SCE). Hence, I_{corr} decreased from 29.685 $\mu A/cm^2$ to 3.187$\mu A/cm^2$.

Table 12: Tafel parameters for the dissolution of mild steel at position 3 during MME/SSW bulk flow

Sample	E_{corr} (mV)	I_{corr} ($\mu A/cm^2$)	β_a (mV)	β_c (mV)	CR (mpy)
24H SSW	-597.625	29.685	90.900	105.300	13.397
24H MME	-593.487	407.602	56.300	64.900	183.947
192H SSW	-641.310	3.187	50.900	33.800	1.438

The 24H MME Tafel curve showed a significant I_{corr} of 407.602 $\mu A/cm^2$, with 183.947 mpy CR. The high CR during 24H MME flow was attributed to a high flow rate at a pressurized area, which in term facilitated the below-listed behaviour;

- A low polarization resistance which was equal to charge transfer resistance (R_3) – having 6.874-ohm value.
- Mass-charge transfer governed the corrosion mechanism, such a reaction is recognised by β_a and β_c being in proximity.
- A very low Q_3 value of $54.350e^{-87}$ F which indicated that the surface was not protected (or the depletion of the coupon sample during corrosion).

6.3.4. Electrochemical results for the mild steel coupon samples located in position 4 within the test rig

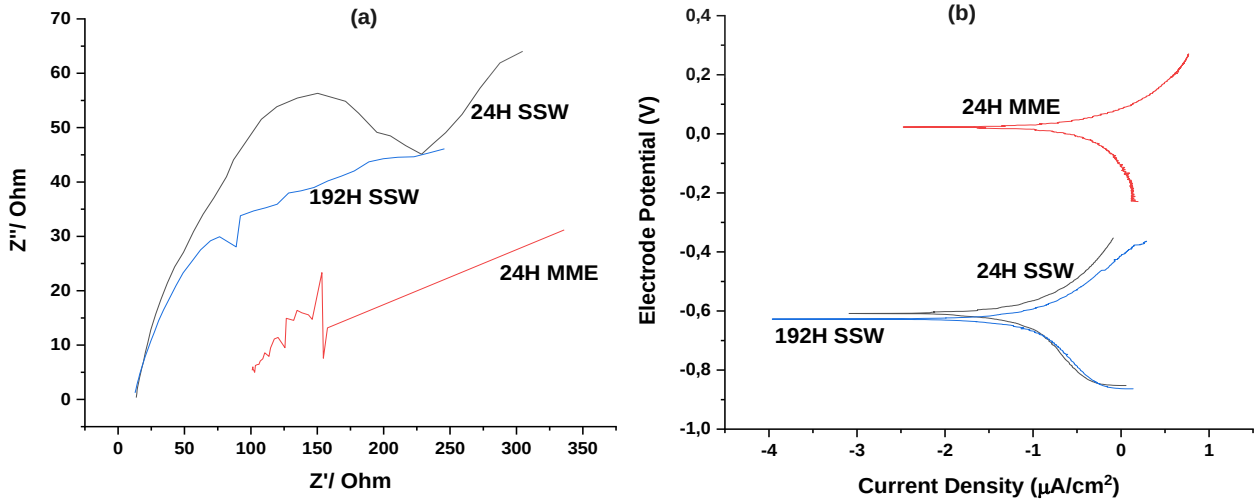

Figure 33: Nyquist (a) and Tafel (b) behaviour of mild steel at position 4 during MME/SSW bulk flow

Figure 33 (a) shows the Nyquist plot results of mild steel at position 4, characterized by 0.107 m/s flow rate and hydrostatic pressure of 0.029 bar. From Figure 33 (a), it can be observed that the Nyquist plot was a depressed semicircle as a result of fractal roughness and non-uniform distribution of current density on the corroded surface.

The Nyquist parameters (Table 13) showed that the charge transfer resistance (R_3) decreased with SSW exposure time, due to a decrease in a_3. This behaviour was further exacerbated by an increase in Q_3 from $0.433e^{-3}$ F to $0.987e^{-3}$ F which indicate that the multi-layered corrosion film was porous. Hence, there was an increase in CR with time. The decrease in a_3 value with SSW exposure time indicated erosion-corrosion synergy. Because of porosity, the (a) factor was far from unity, which implies that the minimal film formed between the metal solution interface did not behave like a capacitor. The high 192H SSW corrosion rate further supported by a decreasing polarization resistance from 13782.100 Ohm to 827.861 Ohm, after 192 hours of SSW exposure. The high 24H MME CR was attributed to low impedance and polarization resistance which lowered the charge resistance (R_3). Although the (a) factor was not far from unity, the high porosity (identifiable by the high Q_3 value) resulted in a low steel charge transfer resistance (R_2) and R_P which was in proximity to the corrosion film's charge transfer resistance (R_3).

Table 13: Nyquist parameters for the dissolution of mild steel at position 4 during MME/SSW bulk flow

Sample	R_1 (Ohm)	Q_1 F.s^(a · 1)	a_1	R_2 (Ohm)	Q_3 F.s^(a · 1)	a_3	R_3 (Ohm)
24H SSW	108.700	$0.106e^{-3}$	0.495	725.100	$0.433e^{-3}$	0.454	13057
24H MME	97.840	$0.482e^{-3}$	0.451	80.850	0.400	0.545	$3.141e^{-3}$
192H SSW	8.599	$2.516e^{-3}$	$1.130e^{-3}$	0.261	$0.987e^{-3}$	0.384	827.600

The Tafel parameters (Table 14) coincided with the results from the Nyquist parameters (Table 13). The relationship between β_c and β_a showed that the corrosion mechanism was controlled by a mass-charge transfer reaction throughout the experiment. The behaviour of the PDP curves showed an increase in SSW corrosion potential (E_{corr}) (from -608.211 mV to -627.852 mV) with immersion time was relative to an increase in corrosion current density (i_{corr})from 19.460 $\mu A/cm^2$ to 34.150 $\mu A/cm^2$. Hence the high CR. Contrary, the 24H MME corrosion mechanism was controlled through a charge transfer (as recognized by dominance of β_c). Such behaviour facilitated a low E_{corr} value of 22.636 mV and a high i_{corr} value of 148.646 $\mu A/cm^2$ which resulted in a high CR of 67.083 mpy. The corrosion film's charge transfer resistance (R_3) appeared to be in proximity with polarization resistance

Table 14: Tafel parameters for the dissolution of mild steel at position 4 during MME/SSW bulk flow

Sample	E_{corr} (mV)	I_{corr} ($\mu A/cm^2$)	β_a (mV)	β_c (mV)	CR (mpy)
24H SSW	-608.211	19.460	56.700	64.500	8.782
24H ARD	22.636	148.646	69.100	92.600	67.083
192H SSW	-627.852	34.150	76.100	89	15.412

6.4. Flow Parameters

In this section, the study focuses on the effect of MME/SSW bulk flow through the test rig. Of interest is the involvement of Mass-transfer Coefficient, Hydromechanical load and Erosion-corrosion synergy during flow-induced corrosion (FIC).

6.4.1. Mass Transfer Coefficient

The mass transfer coefficient was calculated using Equation 48.

Figure 34: Average Mass Transfer Coefficient during Flow Loop

A bulk concentration of $7.237e^{-3}$ mol/m^3 SSW solution and $4.802e^{-3}$ mol/m^3 MME solution was used to study the mass transfer coefficient at each position during bulk flow, results shown in Figure 34. The 24H SSW curve showed a proportional behaviour in mass transfer coefficient with flow rate. Such corrosion behaviour is controlled by charge transfer with oxygen absorption (molecular diffusion) at the steel surface as a driving force of the corrosion mechanism. The high 24H MME mass transfer coefficient confirms the high metal loss, consequent to the high current density and electron transfer when MME electrolyte was used. Therefore convective-mass-transfer-control corrosion (CMTCC). The 192H SSW mass transfer coefficient curve showed a peak at position 2 and 4, which indicates a significant mass removal from the surface. Whilst at position 1 and 3, the 192H SSW mass transfer coefficient favoured phase-transfer-control corrosion (PTCC) which resulted in the formation of a carbonic pseudo-passive film. The mass loss at position 2 was influenced by the angle at which flowing SSW bulk solution strikes the coupon sample, as the solution changes direction inside the duct. Whilst the 192H SSW mass loss at position 4 was much higher, due to CMTCC which results from the high flow rate at a pressurized region.

6.4.2. Hydromechanical Examination

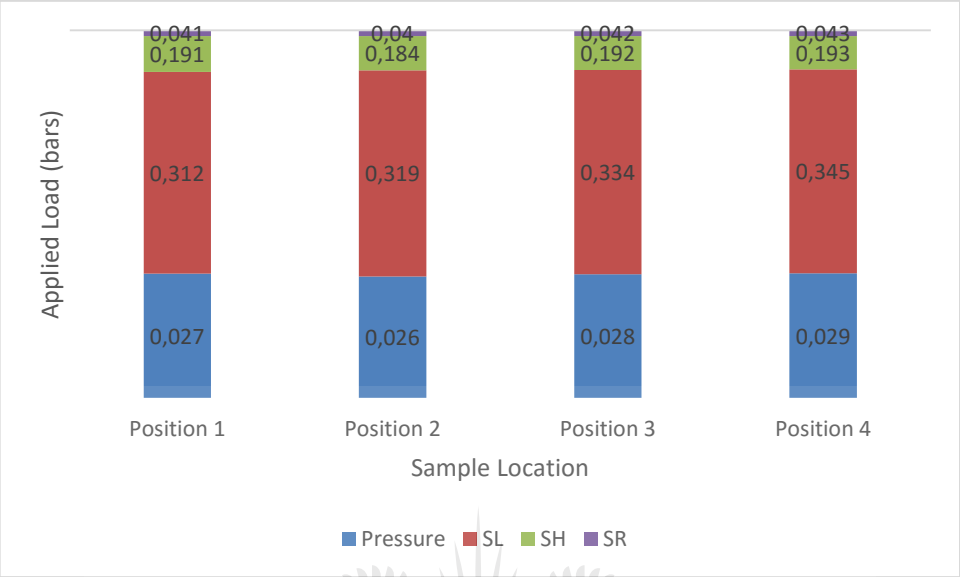

Figure 35: Hydromechanical properties of mild steel during flow

The hydromechanical properties in Figure 35 indicate a significant increase of hydrostatic pressure which resulted in high axial stresses (S_L) of 0.345 bar, a high hook's stress (S_H) of 0.193 bar and high radial stress (S_R) of 0.043 bar at position 4. Because hydrostatic pressure accelerates dissolution kinetics which is not favourable for the polarization of the multi-layered corrosion film (Yang, et al., 2017), only fundamental forces acting at position 4 were discussed. Moreover, hydrostatic pressure facilitated the susceptibility of pitting corrosion experienced at all four positions. Thus, high hydrostatic pressure encourages the adsorption of Cl^- and SO_4^{2-} ion on the inclusion nucleation site (on the steel surface) which lowers the electrical resistivity of the corrosion circuit.

6.4.3. Erosion-corrosion synergy

Figure 36: Erosion-corrosion synergy profile of mild steel when MME/SSW bulk flows over the coupon samples for 24-and 192-hours.

ASTM G119 (2009) and ASTM G102 (2004) standards were used in this study to investigate the effect of erosion-corrosion synergy during MME/SSW bulk flow. Figure 36 shows a negative erosion-corrosion synergy path at position 1, 3, and 4. The negative erosion-corrosion synergy indicates the presence of active shear stress on the surface. A positive erosion-corrosion synergy was however experienced for MME/SSW bulk flow at the bent (position 2). According to Pasha, et al. (2015) such behaviour is controlled by a synergy of erosion and corrosion mechanisms, which accelerates the susceptibility of corrosion attack through tribocorrosion. The value(s) of erosion-corrosion synergy was proportional to that of the CR and coincided with the behaviour of the (a) factor - porosity of the multi-layer film.

6.5. Summary of the Electrochemical Evaluations

6.5.1. Analyses for the 24H SSW bulk flow

Table 15: Summary of the 24H SSW electrochemical assessment at position 1

Position 1 (Flow Parameter)	**Electrochemical Behaviour**	**Findings**
Flow Rate of 0.062 m/s	The limitations of the multi-layered corrosion film were as a result of a polarization resistance of 949.410 Ohm	The electrochemical behaviour resulted in a CR of 7.758 mpy, which was facilitated by a moderate - corrosion potential (E_{corr}) and - corrosion current density (I_{corr})
Hydrostatic Pressure of 0.027 bar	Hence a low corrosion product charge transfer (a_3) of 0.465 which signifies a thin corrosion film layer that failed to behave like a capacitor.	
Mass Transfer Coefficient of 0.013 m/s	The occurrence was made worse by a constant phase element (Q_3) of $0.607e^{-3}$ F which exposed the semi-permeability of the corrosion film	
Longitudinal Stress of 0.312 bar	The resulting semi-porous film generated a moderate charge transfer resistance (R_3) of 908.500 ohm	**Corrosion Mode**
Hook's Stress of 0.191 bar	The supremacy of anodic Tafel slope (β_a) during PDP study shows that the mass transfer governed the corrosion mechanism	Flow Accelerated Corrosion (FAC) because of a developing steels charge transfer resistance (R_2) of 40.910 ohms (developing corrosion film)
Radial Stress of 0.041 bar		
Active Shear Stress of 0.059 g/m^2		

Table 16: Summary of the 24H SSW electrochemical assessment at position 2

Position 2 (Flow Parameter)	**Electrochemical Behaviour**	**Findings**
Flow Rate of 0.018 m/s	The strength of the multi-layered corrosion film was as a result of a high polarization resistance of 19677 Ohm	The electrochemical behaviour resulted in a CR of 1.848 mpy, which was facilitated by a high corrosion potential (E_{corr}) with a low corrosion current density (I_{corr})
Hydrostatic Pressure of 0.026 bar	Hence a high corrosion product charge transfer (a_3) of 0.756 which represented a thick corrosion film which acted as a capacitor.	
Mass Transfer Coefficient of 0.006 m/s	The low constant phase element (Q_3) of 64.390e^{-6} F showed the slight impermeability of the corrosion film	
Longitudinal Stress of 0.319 bar	The compacted corrosion film resulted in a high charge transfer resistance (R_3) of 1080 ohm	**Corrosion Mode**
Hook's Stress of 0.184 bar	The supremacy of cathodic Tafel slope (β_c) during PDP study shows that the charge transfer controlled the corrosion mechanism	Flow Accelerated Corrosion (FAC) because of an excessive steels charge transfer resistance (R_2) of 18597 ohms (a thin corrosion film)
Radial Stress of 0.040 bar		
Erosion-corrosion synergy of 0.013 g/m^2		

Table 17: Summary of the 24H SSW electrochemical assessment at position 3

Position 3 (Flow Parameter)	**Electrochemical Behaviour**	**Findings**
Flow Rate of 0.116 m/s	The limitations of the multi-layered corrosion film were as a result of a polarization resistance of 301.652 Ohm	The electrochemical behaviour resulted in a CR of 13.397 mpy, which was facilitated by a moderate - corrosion potential (E_{corr}) and - corrosion current density (I_{corr})
Hydrostatic Pressure of 0.028 bar	Hence a low corrosion product charge transfer (a_3) of 0.469 which signifies a thin corrosion film layer that failed to behave like a capacitor.	
Mass Transfer Coefficient of 0.043 m/s	The occurrence was worsened by a constant phase element (Q_3) of $0.526e^{-3}$ F which exposed the semi-permeability corrosion film	
Longitudinal Stress of 0.334 bar	The resulting semi-porous film generated a moderate charge transfer resistance (R_3) of 300.900 ohm which was in proximity with polarization resistance	**Corrosion Mode**
Hook's Stress of 0.192 bar	The dominance of cathodic Tafel slope (β_c) during PDP study shows that the charge transfer governed the corrosion mechanism	Shear Impingement Corrosion because $R_3 \approx R_p$, which resulted in a low steels charge transfer resistance (R_2) of 0.752 ohm
Radial Stress of 0.042 bar		
Active Shear Stress of 0.168 g/m^2		

Table 18: Summary of the 24H SSW electrochemical assessment at position 4

Position 4 (Flow Parameter)	**Electrochemical Behaviour**	**Findings**
Flow Rate of 0.107 m/s	The multi-layered corrosion film had a high polarization resistance of 13782.100 Ohm	The electrochemical behaviour resulted in a CR of 8.782 mpy, which was facilitated by a moderate - corrosion potential (E_{corr}) and - corrosion current density (I_{corr})
Hydrostatic Pressure of 0.029 bar	Nonetheless the low corrosion product charge transfer (a_3) of 0.454 which indicates that the thin corrosion film layer failed to behave like a capacitor.	
Mass Transfer Coefficient of 0.028 m/s	The occurrence was exacerbated by a constant phase element (Q_3) of 0.433e^{-3} F which exposed the semi-porous corrosion film	
Longitudinal Stress of 0.345 bar	The resulting semi-porous film generated a high charge transfer resistance (R_3) of 13057 ohm	**Corrosion Mode**
Hook's Stress of 0.193 bar	The correspondence between β_c and β_a during PDP study shows that the mass-charge transfer controlled the corrosion mechanism	Random Impingement Corrosion as a result of harsh flow parameters which resulted in a high steels charge transfer resistance (R_2) of 725.100 ohm
Radial Stress of 0.043 bar		
Active Shear Stress of 0.097 g/m^2		

6.5.2. Analyses for the 192H SSW bulk flow

Table 19: Summary of the 192H SSW electrochemical assessment at position 1

<table>
<tr><th>Position 1
(Flow Parameter)</th><th>Electrochemical Behaviour</th><th>Findings</th></tr>
<tr><td>Flow Rate of 0.062 m/s</td><td>The supremacy of the multi-layered corrosion film was attributed to a 1459.800-ohm increase in polarization resistance</td><td rowspan="3">The electrochemical behaviour resulted in a CR of 3.542 mpy, which was facilitated by a high corrosion potential (E_{corr}) and low corrosion current density (I_{corr})</td></tr>
<tr><td>Hydrostatic Pressure of 0.027 bar</td><td>With exposure time, the corrosion film grew. Hence the increase of corrosion product charge transfer (a_3) by 0.389.</td></tr>
<tr><td>Mass Transfer Coefficient of 0.012 m/s</td><td>The slight increase in constant phase element (Q_3) to $2.314e^{-3}$ F showed that the corrosion film was semi-permeability</td></tr>
<tr><td>Longitudinal Stress of 0.312 bar</td><td>The resulting semi-porous film generated a higher charge transfer resistance (R_3) of 1148 ohm</td><td>Corrosion Mode</td></tr>
<tr><td>Hook’s Stress of 0.191 bar</td><td rowspan="3">The relationship between β_c and β_a during PDP study shows that the corrosion mechanism had changed to mass-charge transfer</td><td rowspan="3">Shear Impingement Corrosion because of the wearing of the corrosion film which resulted in a high steels charge transfer resistance (R_2) of 311.800 ohm</td></tr>
<tr><td>Radial Stress of 0.041 bar</td></tr>
<tr><td>Active Shear Stress of 0.038 g/m^2</td></tr>
</table>

Table 20: Summary of the 192H SSW electrochemical assessment at position 2

Position 2 (Flow Parameter)	**Electrochemical Behaviour**	**Findings**
Flow Rate of 0.018 m/s	There was a significant decrease in polarization resistance at the bend with time	The electrochemical behaviour resulted in a CR of 4.476 mpy, which was facilitated by a high corrosion potential (E_{corr}) with a low corrosion current density (I_{corr})
Hydrostatic Pressure of 0.026 bar	Hence a decrease in corrosion product charge transfer (a_3) by 0.830	
Mass Transfer Coefficient of 0.020 m/s	The substantial decrease in constant phase element (Q_3) shows that the corrosion film has become semi- permeability	
Longitudinal Stress of 0.319 bar	The charge transfer resistance (R_3) significantly decreased to 463.300 ohm which is slightly lower but in the proximity of the polarization resistance	**Corrosion Mode**
Hook's Stress of 0.184 bar	The relationship between β_c and β_a during PDP study shows that the corrosion mechanism had changed to mass-charge transfer	Direct Impingement Corrosion (DIC) because of the high volume of material loss on the surface which resulted in low metal resistance (R_2) of 3.367 ohms
Radial Stress of 0.040 bar		
Erosion-corrosion synergy of 0.050 g/m^2		

Table 21: Summary of the 192H SSW electrochemical assessment at position 3

Position 3 (Flow Parameter)	**Electrochemical Behaviour**	**Findings**
Flow Rate of 0.116 m/s	The tenacious multi-layered corrosion film was attributed to a 1336 ohm increase in polarization resistance	The electrochemical behaviour resulted in a CR of 1.438 mpy, which was facilitated by a higher corrosion potential (E_{corr}) and a low corrosion current density (I_{corr})
Hydrostatic Pressure of 0.028 bar	The significant increase in charge transfer (a_3) indicates the growth of the corrosion film.	
Mass Transfer Coefficient of 0.005 m/s	However, the constant phase element (Q_3) had a noteworthy decrease of $22.210e^{-15}$ F which made the corrosion film impermeable	
Longitudinal Stress of 0.334 bar	The resulting compacted corrosion film generated a higher charge transfer resistance (R_3) of 555.300 ohm	**Corrosion Mode**
Hook's Stress of 0.192 bar	The omnipotence of anodic Tafel slope (β_a) during PDP study shows that the low mass transfer controlled the corrosion mechanism	Flow Accelerated Corrosion (FAC) because of high metal resistance (R_2) of 780.700 Ohm
Radial Stress of 0.042 bar		
Active Shear Stress of 0.018 g/m^2		

Table 22: Summary of the 192H SSW electrochemical assessment at position 4

Position 4 (Flow Parameter)	**Electrochemical Behaviour**	**Findings**
Flow Rate of 0.107 m/s	The multi-layered corrosion film had a lower polarization resistance of 827.861 Ohm	The electrochemical behaviour resulted in a CR of 15.412 mpy, which was facilitated by a high - corrosion potential (E_{corr}) and - corrosion current density (I_{corr})
Hydrostatic Pressure of 0.029 bar	A lower corrosion product charge transfer (a_3) of 0.384 which indicates that the slim corrosion film layer failed to behave like a capacitor.	
Mass Transfer Coefficient of 0.049 m/s	The occurrence was worsened by an increase in the constant phase element (Q_3) of $0.987e^{-3}$ F which exposed the semi-permeable corrosion film	
Longitudinal Stress of 0.345 bar	The resulting semi-porous film generated a low charge transfer resistance (R_3) of 827.600 ohm which was in proximity to the polarization resistance	**Corrosion Mode**
Hook's Stress of 0.193 bar	The correspondence between β_c and β_a during PDP study shows that the mass-charge transfer controlled the corrosion mechanism	Random Impingement Corrosion as a result of harsh flow parameters which resulted in a low steels charge transfer resistance (R_2) of 0.261 ohm
Radial Stress of 0.043 bar		
Active Shear Stress of 0.193 g/m^2		

6.5.3. Analyses for the 24H MME bulk flow

Table 23: Summary of the 24H MME electrochemical assessment at position 1

Position 1 (Flow Parameter)	**Electrochemical Behaviour**	**Findings**
Flow Rate of 0.062 m/s	The limitations of the multi-layered corrosion film were as a result of a polarization resistance of 721.600 Ohm and poor adhesion properties	The electrochemical behaviour resulted in a CR of 10.404 mpy, which was facilitated by a low corrosion potential (E_{corr}) and a high corrosion current density (I_{corr})
Hydrostatic Pressure of 0.027 bar	The constant phase element (Q_3) of $51.260e^{-6}$ F shows that the corrosion film was supposed to be semi-impermeability	
Mass Transfer Coefficient of 0.050 m/s		
Longitudinal Stress of 0.312 bar	The charge transfer resistance (R_3) was 106.800 ohm	**Corrosion Mode**
Hook's Stress of 0.191 bar	The supremacy of cathodic Tafel slope (β_c) during PDP study shows that the charge transfer governed the corrosion mechanism	Visual examination (Figure 39) showed the predominance of multiple wear tracks on the surface, which had the researcher conclude that corrosion mechanism was governed by an erosion-corrosion procedure (tribocorrosion).
Radial Stress of 0.041 bar		
Active Shear Stress of 0.130 g/m^2		

Because an a_3 value of 1 suggests that the surface electrode capacitance (SEC) was equivalent to the ideal capacitance, which was not the case, considering that the there was substantial corrosion rate (CR) during 24H MME/SSW experiments. Henceforward, a visual observation was the preferable approach to diagnose the corrosion mechanism.

Table 24: Summary of the 24H MME electrochemical assessment at position 2

Position 2 (Flow Parameter)	**Electrochemical Behaviour**	**Findings**
Flow Rate of 0.018 m/s	The short comes of the multi-layered corrosion film was as a result of a low polarization resistance of 577.100 Ohm	The electrochemical behaviour resulted in a CR of 18.068 mpy, which was facilitated by a low corrosion potential (E_{corr}) having a high corrosion current density (I_{corr})
Hydrostatic Pressure of 0.026 bar	Hence a moderate corrosion product charge transfer (a_3) of 0.600 which represented a thick of the weak corrosion film which did not act like a capacitor.	
Mass Transfer Coefficient of 0.065 m/s	The low constant phase element (Q_3) of 0.482e^{-3} F showed the semi-permeability of the corrosion film	
Longitudinal Stress of 0.319 bar	The porous corrosion film resulted in a lower charge transfer resistance (R_3) of 265.100 ohm	**Corrosion Mode**
Hook's Stress of 0.184 bar	The supremacy of cathodic Tafel slope (β_c) during PDP study shows that the charge transfer controlled the corrosion mechanism	Direct Impingement Corrosion (DIC) because of the high volume of material loss on the surface which resulted in moderate metal resistance (R_2) of 40.035 ohms
Radial Stress of 0.040 bar		
Erosion-corrosion synergy of 0.213 g/m^2		

Table 25: Summary of the 24H MME electrochemical assessment at position 3

Position 3 (Flow Parameter)	**Electrochemical Behaviour**	**Findings**
Flow Rate of 0.116 m/s	The limitations of the multi-layered corrosion film were as a result of a low polarization resistance of 6.874 Ohm	The electrochemical behaviour resulted in a CR of 183.947 mpy, which was facilitated by a moderate corrosion potential (E_{corr}) and high corrosion current density (I_{corr})
Hydrostatic Pressure of 0.028 bar	The occurrence was deteriorated by a constant phase element (Q_3) of $54.350e^{-87}$ F which exposed the impermeability of the corrosion film	
Mass Transfer Coefficient of 0.880 m/s		
Longitudinal Stress of 0.334 bar	The resulting impermeability film generated a low charge transfer resistance (R_3) of 6.874 ohm which was in proximity with polarization resistance	**Corrosion Mode**
Hook's Stress of 0.192 bar	The relationship between β_c and β_a during PDP study shows that the corrosion mechanism had changed to mass-charge transfer	The ultra-low steels charge transfer resistance (R_2) of $0.325e^{-15}$ F and constant phase element (Q_3) of $54.350e^{-87}$ F shows that the steel exhibited a layer-type corrosion
Radial Stress of 0.042 bar		
Active Shear Stress of 2.000 g/m^2		

Table 26: Summary of the 24H MME electrochemical assessment at position 4

Position 4 (Flow Parameter)	**Electrochemical Behaviour**	**Findings**
Flow Rate of 0.107 m/s	The multi-layered corrosion film had a moderate polarization resistance of 80.850 Ohm	The electrochemical behaviour resulted in a CR of 67.083 mpy, which was facilitated by a low corrosion potential (E_{corr}) and high corrosion current density (I_{corr})
Hydrostatic Pressure of 0.029 bar	A corrosion product charge transfer (a_3) of 0.545 which indicates that the moderate corrosion film layer failed to act as a capacitor.	
Mass Transfer Coefficient of 0.321 m/s	The occurrence experienced a high constant phase element (Q_3) of 0.400 which exposed the porosity of the corrosion film	
Longitudinal Stress of 0.345 bar	The resulting porous film generated a low charge transfer resistance (R_3) of 3.141e^{-3} ohm	**Corrosion Mode**
Hook's Stress of 0.193 bar	The supremacy of cathodic Tafel slope (β_c) during PDP study shows that the charge transfer controlled the corrosion mechanism	Erosion-Corrosion as a result of harsh flow parameters which resulted in a high steels charge transfer resistance (R_2) of 80.850 ohm
Radial Stress of 0.043 bar		
Active Shear Stress of 0.492 g/m^2		

CHAPTER SEVEN

CONCLUSION AND RECOMMENDATIONS

7.1. Introduction

The following chapter summarises the experimental findings, as elaborated in chapter 3. This research aimed to build a rig that can account for the corrosion mechanism in a pipe during a flow loop. Subsequently, this section focuses on the electrochemical behaviour and parameters governing the mild steel corrosion rate during a continuous MME/SSW bulk flow. The chapter concludes with a recommendation for future work concerning flow-induced corrosion.

7.2. Conclusion

In conclusion, the study has shown that internal pipeline corrosion rate has much to do with the science and behaviour (permeability and adhesion properties) of corrosion product on the surface. The presence of a corrosion film on the surface will act as a barrier that impedes the corrosion rate (CR). However, depending on the kinetics governing solubility of the surface corrosion film, the streaming solution can interfere with the integrity of the film to act as a capacitor. Thus, the corrosion film can either be eroded entirely or partially or even damaged to an extent that the film becomes permeable. The rig configuration/flow trajectory was another factor which influenced the behaviour of hydrodynamic parameters such as Mass-transfer Coefficient, Hydromechanical load and Erosion-corrosion synergy by altering the performance of the surface corrosion product film. As demonstrated in Section 6.5 and Table 27, the random impingement corrosion was only observed at position 4. Random impingement corrosion is mostly due to a combination of high flow rate and hydrostatic pressure which led to the dominance of a weak porous $FeCO_3$ corrosion product, which was easily dissolved by the flow. Hence, high hydrostatic pressure was marked by an (a) factor that was far from unity and a high E_{corr} which resulted in a high CR. This shows that at low hydrostatic pressure the corrosion products kinetic reaction governs the dominance of a stable semi-porous FeO(OH) corrosion product. Hence, a large (a)

factor that behaved like a capacitor, which led to a low corrosion rate (CR). Similar, corrosion mechanism at position 3 - 24H SSW and position 1 – 192H SSW, experienced shear impingement corrosion as a result of high shear stress which wore the multi corrosion film. Direct Impingement Corrosion (DIC) were only observed at the bend (at position 2 – 24H MME and 192H SSW). And Flow Accelerated Corrosion (FAC) was observed where the corrosion film was tenacious and lower CR. Considering the scales left behind at position 3 - 24H MME, the high flow rate appeared to have resulted in layer-type corrosion.

Table 27: Evolution of corrosion mechanism within the test-rig

Sample	Position 1	Position 2	Position 3	Position 4
24H SSW	Flow Accelerated Corrosion (FAC)	Flow Accelerated Corrosion (FAC)	Shear Impingement Corrosion	Random Impingement Corrosion
24H MME	Erosion-Corrosion	Direct Impingement Corrosion (DIC)	Layer-type Corrosion	Erosion-Corrosion
192H SSW	Shear Impingement Corrosion	Direct Impingement Corrosion (DIC)	Flow Accelerated Corrosion (FAC)	Random Impingement Corrosion

For low pH solution such as metal mine effluent (MME), the corrosion system did not promote surface corrosion film. Moreover, in the instance were iron sulphide corrosion products are formed, the adhesion properties are weak, and the flowing stream exacerbated the situation by eroding the corrosion film. In such conditions, CR was characterized to be proportional to flow velocity, but not at position 2 (bent) which experienced DIC as a result of marginal turbulence. Thus, the study demonstrated the dominance of corrosion impingement over FAC and the supremacy of flow rate over hydrostatic pressure during flow-sensitive conditions.

Hitherto, scientifical explanation has been explored to account for pipeline corrosion behaviour during MME/SSW solution, and now that the pipeline corrosion rate (CR) has been determined, that data can be used to predict or design the pipe lifespan, including monitoring the thickness and condition location. According to NORSOK M-DP-001-1994 material selection standard, carbon steel with less than 10 mm annual CR can be used as pipelines. Thus, technically making the mild steel used in this study suitable for MME/SSW pipeline construction. Nonetheless, the 0.800 mm thick mild steel coupon samples appear to have exaggerated the corrosion result, but, at the time the size of the coupon (thickness) appeared suitable for the test rig design. Although a thicker mild steel coupon (> 3 mm) of the same material would have given similar corrosion results, it could have further been a better sample size selection for both rig design and experimental purposes (seeing that the 192H MME results were inconclusive because the 0.800 mm coupon sample disintegrated entirely sometime after the 24-hour exposure). Corrosion Allowance (CA) which is the extra thickness added to the steel to corrode without affecting the integrity of the steel, was standardized by ASME B 31.3 to be 3 mm (118.110 mils) for carbon steel pipe and 10 mm (393.701 mils) for carbon steel in harsher environments such as in MME solutions. Nonetheless, because CA is determined from uniform corrosion, the assumption made for the study was that the worse corrosion affected coupon represented the general pipeline corrosion. The CA standard for carbon steel seems to suggest that pipes with $\leq$ 3 mm thickness will have a zero life expectancy, in most cases such pipe standards apply to corrosion-resistant alloys (CRA) for example nickel, copper and stainless steel. In a scenario were the life expectancy is zero, the actual wall thickness corrodes below the minimum required thickness. ASME B 31.3 based on Hoop stress with a safety factor of 1.5 is the most recognizable design method to determine pipe wall thickness. For pressure vessels (such as carbon steel used in pseudo-steady state (PSS) environment) the inversely proportional relationship between wall thickness and diameter should be $\leq$ 0.050. This study shows bare mild steel to be susceptible to corrosion and without any corrosion protection measure, an occurrence that will become hazardous. Although not advisable (because corrosion product can lead to contamination and harm to human health) this study seems to suggest that at ambient temperature a > 3 mm thick bare mild steel installed for an MME/SSW pseudo-steady state (PSS) or pipeline flow loop (PFL) conditions can respectively withstand the corrosion attacks for a lifetime in SSW - PSS conditions and ~ 23 years in MME – PSS

conditions, before compromising the mechanical integrity. Thus, because the corrosion product film partially protects the surface only 0.010 mm of metal is lost every ~ 10 years – for mild steel pressure vessels storing SSW solution or saline solution with a pH ~ 8.020. In an MME - PSS environment (or low pH ≤ 2 bittern solution), the > 3 mm bare mild steel will only last for ~ 23 years before the corrosion attack fully disintegrates the pressure vessels. In contrast, the study further indicates that in a long run, it will be uneconomical to commission bare mild steel for transient operating at a high flow rate. The flow parameters used in this study reveals that the SSW flow-induced corrosion rate is complex and unique to every system (situation). For instance, at first glance, the mild steel at position 3 appears to have a significant dissolution rate, but, because of oxygen absorption; the same > 3 mm (wall thickness) mild steel sample which was initially predicted to loss 0.340 mm per year can end up with 0.037 mm per year. Thus, as a result of corrosion mechanism changing from shear impingement corrosion to FAC, the polarization of a tenacious corrosion film on the surface increased the lifespan of the bare mild steel pipeline from ~ 8 years to ~ 81 years. The opposite is true for erosion-corrosion, impingement corrosion, and layer-type corrosion. Because of this, a > 3 mm bare mild steel pipeline lifespan will be reduced from ~ 63 years to 26 years at a bent (position 2), and ~ 13 years to ~ 7 years at position 4 before the steels integrity can be threatened. Unfortunately, the study further showed that ≤ 10 mm wall thickness bare mild steel should not be used for pipelines made to transport high aqueous sulphur concentration such as MME in mine industries, sulphuric acid in chemical industries and low pH aqueous effluent from power-generation industries. This observation is encouraged by the fact that at low pH, the aqueous solution does not generate protective corrosion product. In cases where mild steel is commissioned to transient high sulphur concentration, it is recommended that the flow rate is kept below 0.062 m/s and a coated thicker wall (> 10 mm) is required. At 0.062 m/s flow rate, MME solution is predicted to corrode 0.264 mm of metal per year (for a flat pipe), meaning that it will take 11 years for the steel to lose its integrity. Unless maintained every ~ 6 years, bare mild steel components are not recommended to be used as bends or in uneven geometry aimed to direct high aqueous sulphur content. Increasing the steel thickness will not prevent steel integrity challenges but will however prolong the mild steel's lifespan. Thus, inhibitors are an efficient mechanism for mitigating internal pipeline corrosion.

7.3. Recommendations for future work

Suggestions for future work are provided below:

1. Since the multi specimen electrochemical test-rigs prototype is designed to be generic, the model can be used to test different materials in either erosion-corrosion synergy, impingement corrosion and flow accelerated corrosion (FAC) conditions.

2. Studies can be done by varying parameters such as temperature, different positions setting (vertical and up -and -downslope inclination flow), akin, propose experimental set-ups for monitoring corrosion mechanism in Top-of-the-line corrosion (TLC) and sidewall corrosion phenomena.

3. More experiments should be performed on corrosion inhibitors for both corrosion performance and adhesion integrity test.

4. There are various types of iron sulphide films, and iron carbonates films, of which the mechanism of formation of these films remains unclear and requires further investigations. The interaction between siderite ($FeCO_3$), lepidocrocite (FeO(OH)), aragonite ($CaCO_3$), hematite (Fe_2O_3), mackinawite (FeS), and pyrite (FeS_2) is of great interest; researchers are recommended to study the mechanism in which this corrosion product affects the kinetics of corrosion rate, moreover, the conversion mechanism from Fe_2O_4 to Fe_2CO_3 or FeS.

5. Study the effects of $FeCO_3$ layers in longer test duration, to see how exposure time for high shear stress conditions affects $FeCO_3$ layer, considering that the film is time-dependent.

6. Respectively study effects of Cl^- ions and SO_4^{2-} ions on localized corrosion in an H_2S/H_2CO_3 mixed systems, at a higher temperature and in a more extended test duration.

7. To date, Africa does not have a large-scale corrosion flow loop testing facility to achieve higher velocities with similar conditions to field operations, thus large-scale corrosion flow loop needs to be built to perform more experiments which will solve corrosion problems unique to Africa.

CHAPTER EIGHT

REFERENCES

Addis, J. F., Nesic, S. & Irwin, D., 2008. *Erosion-Corrosion in Disturbed Liquid/Particle Flow.* Ohio: The Russ College of Engineering and Technology of Ohio University.

Anderko, A., McKenzie, P. & Young, R. D., 2000. Computation of rates of general corrosion using electrochemical and thermodynamic models. *Corrosion,* Volume 00479.

Andrew, R. H., 2013. Corrosion problems and their solutions in South African deep-level gold mines. *British Corrosion Journal,* 29(3), pp. 219-225.

ASTM D1141-98, 2013. *Standard Practice for the Preparation of Substitute Ocean Water.* West Conshohocken: ASTM International.

ASTM G102, 1994. *Standard Practice for Calculation of Corrosion Rates and Related Information from Electrochemical Measurements.* Philadelphia, Patent No. 19103.

ASTM G102, 2004. *Standard Practice for Calculation of Corrosion Rates and Related Information from Electrochemical Measurements.* USA: ASTM international.

ASTM G1-03, 2017. *Standard Practice for Preparing, Cleaning and Evaluating Corrosion Test Specimens.* West Conshohocken: ASTM International.

ASTM G119, 2009. *Standard Guide for Determining Synergism Between Wear and Corrosion.* USA: ASTM international.

ASTM G73 - 98, 1998. *Standard Practice for Liquid Impingement Erosion Testing.* West Conshohocken: ASTM International.

Bazhenova, L. A. & Semenov, A. G., 2013. On the Influence of the Reynolds Number on the Intensity of Vortex Sound Flow around a Cylindrical Profile. *Acoustical Physics,* 59(5), pp. 539-547.

Behpour, M., Ghoreishi, S. M. & Soltani, N., 2009. The inhibitive effect of some bis-N, S-bidentate Schiff bases on corrosion behaviour of 304 stainless steel in hydrochloric acid solution PA. *Corrosion Science,* 51(5), p. 1073–1082.

Benabdellah, M., Khaled, K. F. & Hammouti, B., 2010. Kinetic investigation of C38 steel corrosion in concentrated perchloric acid solution. *Materials Chemistry and Physics,* 120(1), pp. 61-64.

Bockris, J. O., Drazic, D. & Despic, A. R., 1961. Electrochimica Acta. *The Electrode Kinetics of the Deposition and Dissolution of Iron,* Volume 4, pp. 325-361.

Boger, D. V., 1987. Viscoelastic Flow-Through Contraction. *Annual Review of Fluid Mechanics,* Volume 19, pp. 157-82.

Brett, C. M. & Melo, P. I., 1997. Influence of anions on the corrosion of high-speed steel. *Journal of Applied Electrochemistry,* Volume 27, pp. 959-964.

Briano, F. O., Wojtas, N. & Herold, C., 2012. *Design, Fabrication and Testing of a Large-area Micro Heat Transfer System for Power Cube Application.* Zurich: Swiss Federal Institute of Technology (ETH) Zurich.

Brodkey, R. S., 1967. The Phenomena of Fluid Motion. In: *Fluid dynamics.* s.l.:Addison-Wesley, p. 737.

Brown, B. N., Alam, K. & Irwin, D., 2013. *The Influence of Sulfides on Localized Corrosion of Mild Steel.* Ohio: The Russ College of Engineering and Technology of Ohio University.

Brytan, Z., Niagaj, J. & Reiman, L., 2016. Applied Surface Science Corrosion studies using potentiodynamic and EIS electrochemical techniques of welded lean duplex stainless steel UNS S82441. *Applied Surface Science,* Volume 388, p. 160–168.

Chen, T. Y., Moccari, A. & MacDonald, D. D., 1992. The development of controlled hydrodynamic techniques for corrosion testing. *Corrosion,* 48(3), pp. 239-255.

Chhabra, R. P. & Richardson, J. F., 1999. Non-Newtonian Flow in the Process Industries. *Science Direct,* 79(3), pp. 1-36.

Chilton, T. H. & Colburn, A. P., 1934. Mass Transfer (Absorption) Coefficients Prediction from Data on Heat Transfer and Fluid Friction. *Industrial & Engineering Chemistry,* Volume 26, pp. 1183-1187.

Climax Molybdenum Company, 1953. Alloy steels pay off. In: U. o. Michigan, ed. *Steel alloys.* New York: Empire Press, p. 67.

Clover, D. et al., 2005. The influence of microstructure on the corrosion rate of various carbon steels. *Journal of Applied Electrochemistry,* Volume 35, p. 139–149.

Collins, R. E., 1991. *Pseudo-Steady-State Flow and the Transient Pressure Behavior of Fractured Wells: A New Analytical Technique for Complex Wellbore Configurations. Presented at the SPE Annual Technical Conference and Exhibition.* [Online]

Available at: http://dx.doi.org/10.2118/22660-MS

[Accessed 1 October 2019].

Combrink, G. A., 1995. Cathodic Disbonding in Flowing Sea Water. In: C. a. P. Centre, ed. *Master of Science Mini Dissertation.* Manchester England: The University of Manchester Institute of Science and Technology, pp. 1-110.

Copson, H. R., 1960. Effects of Velocity on Corrosion. *Corrosion,* 16(2), p. 86.

CorrISA, 2019. *201981 CorrosionExclusively V5E2 0719.indd.* [Online]
Available at: http://www.corrosioninstitute.org.za/wp-content/uploads/2019/08/CorrosionExclusively-Volume-5-Edition-2.pdf
[Accessed 8 January 2020].

Cubicciotti, D., 1988. Flow assisted corrosion of steel and the influence of Cr and Cu additions. *Journal of Nuclear Materials,* Volume 152, p. 259–64.

Darowicki, K., 1995. Corrosion rate measurements by Non-linear Electrochemical Impedance Spectroscopy. *Corrosion Science,* Volume 37, p. 913.

Davies, J. T., 1972. *Turbulence Phenomena: An Introduction to the Eddy Transfer of Momentum, Mass, and Heat, Particularly at Interfaces.* New York: Academic Press.

Davies, M. & Scott, P. J. B., 2006. *Oilfield Water Technology.* Houston Texas: NACE - National Association of Corrosion Engineers.

de Moraes, F. D., Shadley, J. R., Chen, J. & Rybicki, E. F., 2000. Characterization of CO2 corrosion product scales related to environmental conditions. *Corrosion,* Volume 0030.

de Waard, C. & Milliams, D. E., 1975. Carbonic acid corrosion of steel. *Corrosion,* 31(5), pp. 177-181.

Dexter, S. C., Duquette, D. J., Siebert, O. W. & Videla, H. A., 1991. Use and Limitations of Electrochemical Techniques for Investigating Microbiological Corrosion. *Corrosion,* 47(4), pp. 308-318.

Döner, A., Solmaz, R., Özcan, M. & Kardaş, G., 2011. Experimental and theoretical studies of thiazoles as corrosion inhibitors for mild steel in sulphuric acid solution. *Corrosion Science,* 53(9), p. 2902–2913.

DPI Plastics, 2013. *Pressure Pipe System.* [Online]
Available at: https://www.incledon.co.za/Documents/DPI%20PVC-U%20_%20PVC-M%20pressure%20pipe%20brochure%202013.pdf
[Accessed 10 January 2021].

Dugstad, A., 1998. Mechanism of protective film formation during CO2 corrosion of carbon steel. *Corrosion/1998,* p. 9831.

Dugstad, A., 2006. Fundamental aspects of CO2 metal loss corrosion-part I: Mechanism. *Corrosion,* Volume 06111.

Dugstad, A. & Lunde, L., 1994. Influences of low alloying elements upon the CO2 corrosion rate. *NACE Corrosion,* Volume 473.

Dugstad, A., Lunde, L. & Videm, K., 1994. Parametric study of CO2 corrosion of carbon steel. *Corrosion,* Volume 99014.

Duncan, R., n.d. Material Performance in Khuff Gas Service. *Material Performance,* 19(7), pp. 45-53.

Efird, K. D., 2000. Flow-induced corrosion. In: *Uhlig's Corrosion Handbook.* New York: John Wiley & Sons Inc, pp. 233-247.

Eldik, R. & Palme, D. A., 1982. Effects of pressure on the kinetics of the dehydration of carbonic acid and the hydrolysis of CO2 in aqueous solution. *Journal of Solution Chemistry,* 11(5), pp. 339-346.

Ellison, B. T. & Wen, C. J., 1981. Hydrodynamic Effects on Corrosion, Tutorial lectures in Electrochemical Engineering and Technology. *AIChE Symposium,* 77(204), pp. 161-169.

Favelas, F. et al., 2010. Evolution of dissolution processes at the interface of carbon steel corroding in a CO2 environment studied by EIS. *Corrosion Science,* 52(2), pp. 509-517.

Featherstone, R. E. & Nalluri, C., 1995. *Civil Engineering Hydraulics.* 6 ed. Oxford: Blackwell Science.

Fekry, A. M. & Ameer, M. A., 2011. Electrochemical investigation of corrosion and hydrogen evolution rate of mild steel in sulphuric acid solution. *International Journal of Hydrogen Energy,* Volume 36, pp. 11207-11215.

Fester, V. G. & Slatter, P. T., 2009. Dynamic Similarity for non-Newtonian Fluids in Globe Valves. *Chemical Engineering Research and Design,* Volume 87, pp. 291-297.

Fontana, M. D. & Green, N. D., 1978. *Corrosion Engineering.* 2 ed. s.l.:McGraw-Hill.

Freund, J. B., Goetz, J. G., Vermont, J. & Hill, K. L., 2012. Fluid Flow and Forces in Development: Functions, Features and Biophysical Principle. *dev.biologists.org,* 139(16), p. 3063.

Gavrilakis, S., 1992. Numerical simulation of low-Reynolds-number turbulent flow through a straight square duct. *Journal of Fluid Mechanics,* Volume 244, p. 101–129.

Gerischer, H. & Mehl, W. Z., 1959. Some Abnormal Hydrogen Electrode Reactions. *Chemical,* Volume 37, pp. 213-221.

Gray, L. G. S., Anderson, B. G., Danysh, M. J. & Tremaine, P. R., 1990. Effect of pH and temperature on the mechanism of carbon steel corrosion by aqueous carbon dioxide. *Corrosion,* Volume 40.

Guo, J. et al., 2008. Influence of carbon content and microstructure on corrosion behaviour of low alloy steels in a Cl containing environment. *Corrosion Science,* 51(1), pp. 242-251.

Haldenwang, R., Slatter, P. T. & Chhabra, R. P., 2010. An Experimental Study of non-Newtonian Fluid Flow in Rectangular Flumes in Laminar, Transition and Turbulent Flow Regimes. *Journal of the South African Institution of Civil Engineering,* 52(1), pp. 11-19.

Han, H. & Gabriel, K. S., 2007. A Numerical Study of Entrainment Mechanism in Axisymmetric Annular Gas-Liquid Flow. *Journal of Fluids Engineering, Transactions of the ASME,* Volume 129, pp. 293-301.

Han, J., Yang, Y., Nesic, S. & Brown, B. N., 2008. Roles of passivation and galvanic effects in localized CO2 corrosion of mild steel. *Corrosion Science,* Volume 08332.

Han, J., Young, D. & Nesic, S., 2008. Characterization of the passive film on mild steel in CO2 environments. *Corrosion Science,* Volume 2511.

Hao, X. H. et al., 2012. Influence of Microstructure Of AH32 Corrosion Resistant Steel on Corrosion Behavior. *Acta Metallurgica Sinica,* 48(5), pp. 534-540.

Heitz, E., 1991. Chemo-mechanical effects of flow on corrosion. *Corrosion Science,* 47(2), pp. 135-145.

Hewitt, G. F., 2005. Three-phase gas-liquid-liquid flows in the steady and transient states. *Nuclear Engineering and Design,* 235(10-12), pp. 1303-1316.

Hubner, W. & Leitel, E., 1996. Peculiarities of erosion-corrosion processes. *Tribology International,* 29(3), p. 199.

Husseini, T., 2018. *Transporting oil and gas: the world's longest pipelines.* [Online] Available at: https://www.offshore-technology.com/features/worlds-longest-pipelines/ [Accessed 18 December 2020].

Igwemezie, V. C. & Ovri, J. O., 2013. An investigation into the Effects of Microstructure on the Corrosion Susceptibility of Medium Carbon Steel. *The International Journal Of Engineering And Science (IJES),* 2(6), p. 2319 – 1813.

Ishii, M. & Grolmes, M. A., 1975. Inception Criteria for Droplet Entrainment in Two-Phase Concurrent Film Flow. *AIChE Journal,* Volume 21, pp. 308-318.

Jahn, A. P., 1954. Report of Committee A-5 on Corrosion of Iron and Steel, in Proceedings ASTM. *American Society for Testing and Materials,* Volume 54.

Jasinski, R., 1987. Corrosion of N80-type steel by CO2 water mixtures. *Corrosion Science,* 43(4), pp. 214-218.

Jawarneh, A. M. & Vatistas, G. H., 2006. Jawarneh, A.M. & Vatistas, G.H. 2006. Reynolds stress model in the prediction of confined turbulent swirling flows. *Journal of Fluids Engineering,* 128(1), pp. 1377-1382.

Jeong, J., Hussain, F., Schoppa, W. & Kim, J., 1997. Coherent structures near the wall in a turbulent channel flow. *Journal of Fluid Mechanics,* Volume 332, p. 185–214.

Jianfu, Z. & Gabriel, K. S., 2004. Two-phase flow patterns in a 90-degree bend in microgravity. *The Chinese Society of Theoretical and Applied Mechanics,* 20(3), p. 207.

Jimenez, J. & Moin, P., 1991. The minimal flow unit in near-wall turbulence. *Journal of Fluid Mechanics,* Volume 225, pp. 213-240.

Kataoka, I., Ishii, M. & Mishima, K., 1983. Generation and Size Distribution of Droplet in Annular Two-Phase Flow. *Journal of Fluids Engineering, Transactions of the ASME,* Volume 105, pp. 230-238.

Kinsella, B., Tan, Y. J. & Bailey, S., 1998. EIS and Surface Characterisation Techniques to Study Carbon dioxide Corrosion Product Scales. *Corrosion.*

Krivenko, A. G., Manzhos, R. A. & Protasova, S. G., November 2018. Effect of impulse high voltage anodic and cathodic electrochemical treatment of a glassy carbon electrode on the oxygen reduction reaction in alkaline media. *Electrochemistry Communications,* Volume Volume 96, pp. 57-60.

Larrabee, C. P., 1953. Corrosion Resistance of High Strength Low Alloy Steels as Influenced by Composition and Environment, Corrosion, Vol 9 (No. 8), 1953, p 259-271. *Corrosion,* 9(8), pp. 259-271.

Larrabee, C. P. & Coburn, S. K., 1962. *The Atmospheric Corrosion of Steels as Influenced by Changes in Chemical Composition.* C.P. Larrabee and S.K. Coburn, The Atmospheric Corrosion of Steels as Influenced by Changes in Chemical CoButterworths, First International Congress on Metallic Corrosion.

Lee, K. L., 2003. *EIS Investigation of CO2 / H2S Corrosion.* Oklahoma: Institute for Corrosion and Multiphase Technology, Ohio University.

Li, H., Nesic, S. & Irwin, D., 2011. *A Mechanistic Model for CO2 Localized Corrosion of Carbon Steel.* Ohio: The Russ College of Engineering and Technology of Ohio University.

Lin, G., Zheng, M., Bai, Z. & Zhao, X., 2006. Effect of temperature and pressure on the morphology of carbon dioxide corrosion scales. *Corrosion,* 62(6), pp. 501-507.

Linter, B. R. & Burstein, G. T., 1999. Reactions of pipeline steels in carbon dioxide solutions. *Corrosion Science,* 41(1), pp. 117-139.

Liu, S., African, A., Nasr-El-Din, H. A. & Masliyah, J., 1994. An experimental study of pressure drop in helical pipes. *Mathematical and Physical Sciences,* 444(1921), p. 307.

Lotgering, F., 1959. Topotactical Reaction with Ferrimagnetic Oxides having Hexagonal Crystal. *Journal of Organic and Nuclear Chemistry,* 9(2), pp. 113-123.

Lu, J. & Tiab, D., 2008. Productivity equations for an off-centre partially penetrating vertical well in an anisotropic reservoir. *Journal of Petroleum Science and Engineering,* 60(1), p. 18–30.

Lu, J. & Tiab, D., 2009. *Productivity Equations for Oil Wells, VDM, Saarbrucken,*. Saarbrucken Germany: VDM.

Ma, H. et al., 2000. The Influence of Hydrogen Sulfide on Corrosion of Iron under Different Conditions. *Corrosion Science,* 42(10), pp. 1669-1683.

Mahmoodian, M., 2018. Introduction. In: 1, ed. *Reliability and Maintainability of Inservice Pipeline.* s.l.: Gulf Professional Publishing, pp. 1-48.

Malik, H., 1995. Influence of C16 quaternary amine on surface films and polarization resistance of mild steel in carbon dioxide-saturated 5% sodium chloride. *Corrosion,* 51(4), pp. 321-328.

Malka, R., Gulino, D. & Irwin, D., 2005. *Erosion Corrosion and Synergistic Effects in Disturbed Liquid-Particle Flow*. Ohio: Fritz J. and Dolores H. Russ College of Engineering and Technology of Ohio University.

Marcus, P. & Maurice, V., 2004. *"Fundamental aspects of corrosion of metallic materials" material science and engineering.* [Online]

Available at: http://www.eolss.net/samplechapters/c05/e6-36-02-04.pdf.

[Accessed 10 12 2019].

Martins, J. D. N. & Freire, E., 2009. Applications and Market of PVC for Piping Industry. *Polimeros: Ciencia e Tecnologia,* 19(1), pp. 58-62.

Mazumder, Q. H., 2004. *Development and Validation of a Mechanistic Model to Predict Erosion in Single-Phase and Multiphase Flow*. Oklahoma: The University of Tulsa.

Meng, H. S. & Ludema, K. C., 1995. Wear models and predictive equations: their form and content. *Wear*, 181(183), pp. 443-457.

Misawa, T., Hashimoto, K. & Shimodaira, S., 1974. The mechanism of formation of iron oxide and oxyhydroxides in aqueous solutions at room temperature. *Corrosion Science,* Volume 14, pp. 131 - 149.

Mofu, T. G., Makhatha, E. M. & Arotiba, A. O., 2017. *Corrosion Inhibition of Mild Steel in 1 M HCL using Synthesized Eco-Friendly Polymer Composites.* Johannesburg: Faculty of Built Environment & the Build Engineering University of Johannesburg.

Mohyaldinn, M. E., Hamzah, R. & Ismail, M. C., 2016. *Prediction of Sand Erosion in Elbows and Tees Using Direct Impingement Model.* [Online]
Available at: https://www.researchgate.net
[Accessed 25 March 2018].

Moiseeva, L. S. & Rashevskaya, N. S., 2002. Effect of pH value on corrosion behaviour of steel in CO2-containing aqueous media. *Russian Journal of Applied Chemistry*, 75(10), pp. 1625-1633.

Möller, H., 2007. The influence of Mg2+ on the formation of calcareous deposits on a freely corroding low carbon steel in seawater. *Corrosion Science,* 49(4), pp. 1992-2001.

NaturalGas.org, 2013. *The Transportation of Natural Gas.* [Online]
Available at: http://naturalgas.org/naturalgas/transport/
[Accessed 5 March 2020].

Nesic, S., 1994. A Working Party Report on Predicting CO2 Corrosion in the Oil and Gas Industry. In: *Prediction of transport processes in CO2 corrosion.* London: The Institute of Materials, pp. 120-133.

Nešić, S., 2007. Key issues related to modelling of internal corrosion of oil and gas pipelines – A review. *Corrosion Science,* 49(12), p. 4308–4338.

Nesic, S., 2011. Uhlig's Corrosion Handbook. In: 3, ed. *Carbon dioxide corrosion of mild steel.* New Jersey: A John Wiley and Sons Inc, pp. 229-245.

Nesic, S., 2012. Effects of multiphase flow on internal CO2 corrosion of mild steel pipelines. *Energy Fuels,* 26(7), pp. 4098-4111.

Nešić, S., Nordsveen, M. & Stangeland, A., 2001. A mechanistic model for CO2 corrosion with protective iron carbonate scale films. *Corrosion,* Volume 01040.

Nešić, S., Postlethwaite, J. & Olsen, S., 1996. An electrochemical model for prediction of corrosion of mild steel in aqueous carbon dioxide solutions. *Corrosion,* 52(12), p. 280–294.

Nesic, S., Postlethwaite, J. & Vrhovac, M., 1997. CO2 corrosion of carbon steel-from mechanistic to empirical modelling. *Corrosion Reviews,* 15(1-2), pp. 211-240.

Nesic, S., Pots, B. F., Postlethwaite, J. & Thevenot, N., 1995. Superposition of Diffusion and Chemical Reaction Controlled Limiting Currents-Applications to CO2 Corrosion. *Journal of Corrosion Science and Engineering,* 1(3).

Nesic, S., Solvi, G. T. & Enerhaug, J., 1995. Comparison of the rotating cylinder and pipe flow tests for flow-sensitive CO2 corrosion. *Corrosion,* 51(10), pp. 773-787.

Nesic, S. & Sun, W., 2009. Corrosion in acid gas solutions. In: *Shreir's Corrosion.* Elsevier: s.n., pp. 1270-1298.

Nesic, S., Thevenot, N., Crolet, J. L. & Drazic, D. M., 1996. Electrochemical properties of iron dissolution in the presence of CO2 - basics revisited. *Corrosion,* Volume 9603.

Nesic, S. & Vrhovac, M., 1999. A neural network model for CO2 corrosion of carbon steel. *Journal of Corrosion Science and Engineering,* 1(4), pp. 1-13.

Neville, A., Hodgkiess, T. & Dallas, J. T., 1995. A study of the erosion-corrosion behaviour of engineering steels for marine pumping applications. *Wear,* 186(187), pp. 497-507.

Nor, A. M., Nesic, S. & Irwin, D., 2013. *The Effect of Turbulent Flow on Corrosion of Mild Steel in High Partial CO2.* Ohio: the Russ College of Engineering and Technology of Ohio University.

Nordsveen, M., Nesic, S., Nyborg, R. & Stangelan, A., 2003. A mechanistic model for carbon dioxide corrosion of mild steel in the presence of protective iron carbonate films - Part 1: Theory and verification. *Corrosion,* 59(5), pp. 443-456.

Ogazi, A. C., Afolabi, A. S. & AbdulkareeM, A. S., 2015. *Comparative studies of electrochemical corrosion behaviour of mild steel in some agro-fluids.* Florida: Unisa.

Ozhigov, L. S. et al., 2017. The Effect of non-Metallic Inclusions in Low-Alloyed Carbon Steel on the Service Life of NPP Pipe Line. *Thermal and Fast Reactor Materials,* 4(110), pp. 59-64.

Parakala, S. R., 2005. *EIS Investigation of Carbon Dioxide And Hydrogen Sulfide Corrosion Under Film Forming Conditions.* Athens: Ohio University.

Pasha, A., Ghasemi, H. M. & Neshati, J., 2015. Synergistic erosion-corrosion behaviour of X-65 carbon steel at various impingement angles. *Journal of Tribology.*

Pienaar, V., 2004. *Viscous Flow Through Sudden Contractions.* Cape Town: Flow Process Research Centre, Cape Technikon.

Pots, B. F., 1995. Mechanistic models for the prediction of CO2 corrosion rates under multiphase flow conditions. *Corrosion,* Volume 95137.

Pourbaix diagram (stability diagram), n.d. *Pourbaix diagram (stability diagram).* [Online]

Available at: http://www.uobabylon.edu.iq/eprints/publication_12_18276_228.pdf [Accessed 6 December 2020].

Qu, L., Norberg, C., Davidson, L. & Peng, S.-H., 2013. Quantitative Numerical Analysis of Flow past a Circular Cylinder at Reynolds Number between 50 and 200. *Journal of Fluids and Structures,* Volume 39, pp. 347-370.

Rahmani, M. & Strutt, J. E., 1992. *Hydrodynamic Modeling of Corrosion of Carbon Steels and Cast Irons in Sulfuric Acid. Houston: NACE, 1992.* Houston: NACE.

Rahman, M. M. & Biswas, R., 2009. Effects of Beta Ratio and Reynold's Number on Coefficient of Discharge of Orifice Meter. *Journal of Agriculture and Rural Development,* Volume 7, pp. 151-156.

Ramamurthy, A. V. & Boger, D. V., 1971. Developing velocity profiles on the downstream side of a contraction for inelastic polymer solutions. *Transactions of the Society of Rheology,* 15(4), pp. 709-730.

Rani, H. P. et al., 2014. CFD study of flow accelerated corrosion in 3D elbows. *Annals of Nuclear Energy,* Volume 69, pp. 344-351.

Remita, E. et al., 2008. Hydrogen evolution in aqueous solutions containing dissolved CO2: Quantitative contribution of the buffering effect. *Corrosion Science,* 50(5), pp. 1433-1440.

Revie, R. W., 2008. Corrosion and Corrosion Control. In: T. &. Engineering, ed. s.l.: John Wiley & Sons, pp. 96-97.

Roberge, P. R., 2008. *Corrosion Engineering, Principles and Practice.* s.l.: McGraw Hill.

Ruthemann, L., 2011. *Fabrication, characterization and modelling of a micro heat transfer system for power enhancement of thermoelectric generators.* Zurich: Master'sthesis ETH Zurich.

Ruzic, V., Veidt, M. & Nesic, S., 2006. Protective iron carbonate films - Part 1: Mechanical removal in single-phase aqueous flow. *Corrosion,* 62(5), pp. 419-432.

Schmitt, G. & Hörstemeier, M., 2006. Fundamental aspects of CO2 metal loss corrosion – Part II: Influence of different parameters on CO2 corrosion mechanisms. *Corrosion,* Volume 06112.

Schmitt, G. & Rothmann, B., 1977. Corrosion mechanism of unalloyed steel in oxygen-free carbon dioxide solutions - Part 1: Kinetics of the liberation of hydrogen. *Werkst. Korros,* 28(12), pp. 816-822.

Scully, J. R., 2003. The influence of mass transport on the electrochemical process. In: *Electrochemical Techniques in Corrosion Science and Engineering.* New York: Marcel Dekker Inc, pp. 151-175.

Shannon, R. & Ross, R., 1964. Definition of Topotaxy. *Nature,* Volume 202, pp. 1000-1001.

Shoham, O., 2006. *Mechanistic modelling of gas-liquid two-phase flow in pipes.* Richardson: Society of Petroleum Engineers.

Singer, M., 2013. *Study and Modeling of the Localized Nature of Top of the Line Corrosion.* Athens: The Russ College of Engineering and Technology of Ohio University.

Slider, H. C., 1966. *Application of Pseudo-Steady-State Flow to Pressure-Buildup Analysis. Presented at the SPE Amarillo Regional Meeting.* [Online]
Available at: http://dx.doi.org/10.2118/1403-MS
[Accessed 1 September 2019].

Sluyters-Rembach, M. & Sluyters, J. H., 1970. *Electroanalytical Chemistry.* 4 ed. New York: Marcel Dekker.

Smith, S. N., 2001. A Proposed Mechanism for Corrosion in Slightly Sour Oil and Gas. *Corrosion Congress,* Volume 01304.

Stern, M., 1955. The electrochemical behaviour, including hydrogen overvoltage of iron in acid environments. *Journal of the Electrochemical Society,* 102(11), pp. 609-616.

Stringgow, B., 2013. *Field measurement for oxidation-reduction potential (ORP),* Georgia: U.S Environmental protective agency (EPA).

Stuckey, P. E., Zawodzinski, T. A. & Mann, J. A., 2012. *Kinetic Studies and Electrochemical Processes at Fuel Cell Electrodes.* Cleveland, Ohio: Case Western Reserve University.

Sundar, K., 1987. *A Method for Evaluating the Effects of two-phase flow velocity on the performance of oil field corrosion inhibitors.* Oklahoma: the University of Tulsa.

Sun, J. B., Zhang, G. A., Liu, W. & Lu, M. X., 2012. The formation mechanism of corrosion scale and electrochemical characteristic of low alloy steel in carbon dioxide-saturated solution. *Corrosion Science,* Volume 57, pp. 131-138.

Sun, W. & Nesic, S., 2007. A Mechanistic Model of H2S Corrosion of Mild Steel. *Corrosion,* Volume 07655.

Tatsumi, T. & Yoshimura, T., 1990. Stability of the laminar flow in a rectangular duct. *Fluid mechanics,* Volume 212, pp. 437-449.

Tlili, M., Amor, M. B., Gabrielli, C. & Joiret, S., 2006. On the initial stages of calcium carbonate precipitation. *Journal Europeen d'Hydrologie,* 37(1), pp. 89-108.

Tony, W., Shen, H. & Tsai, S. F., 2006. *Vortical flow topology in a curved duct with 900 bends. Proceedings of the 4th WSEAS International Conference on Fluid Mechanics and Aerodynamics.* Elounda, National Taiwan University.

Trethewey, K. R. & Chamberlain, J., 1988. *Corrosion for Students of Science and Engineering.* England: Longman Scientific and Technical.

Ts'oeuntane, G. M., Makhatha, E. M. & Arotiba, A. O., 2017. *Corrosion inhibition of mild steel in 1 M HCL using synthesized eco-friendly polymer composites.* 1 ed. Johannesburg: University of Johannesburg.

United Fire Protection, 2020. *Actual corrosion found during an NFPA 25 Internal Pipe Inspection.* [Online]

Available at: https://unitedfiresystems.net/nitrogenpac/all-about-corrosion

[Accessed 20 December 2020].

Van Rossum, J. J., 1959. Experimental Investigation of Horizontal Liquid Films: Wave Formation, Atomization, Film Thickness. *Chemical Engineering Science,* Volume 11, pp. 35-52.

Van Sittert, F. P., 1999. *The Effect of Pipe Roughness on Non-Newtonian Turbulent Flow*. Cape Town: Cape Technikon.

Videm, K., 1993. Fundamental studies aimed at improving models for prediction of CO2 corrosion. In: *Understanding and Prevention of Corrosion.* London: Institute of Materials, pp. 504-512.

Videm, K. & Dugstad, A., 1989. Corrosion of carbon steel in an aqueous carbon dioxide environment - Part 1: Solution effects. *Mater. Perform,* 28(3), pp. 63-67.

Villien, B., Zheng, Y. & Lister, D. H., 2001. *Proceedings of the twenty-sixth annual CNS-CNA student conference.* Toronto, s.n.

Wallis, G. B., 1969. *One-dimensional two-phase flow*. New York: McGraw-Hill: McGraw-Hill.

Wang, H., 2002. *CO2 Corrosion Mechanistic Modeling in Horizontal Slug Flow.* Ohio: Fritz J and Dolores H. Russ College of Engineering and Technology at Ohio University.

Wang, X., Duan, J., Zhang, J. & Hou, B., 2008. Alloy elements' effect on anti-corrosion performance of low alloy steels in different sea zones. *Materials Letters,* 62(8-9), pp. 1291-1293.

Wang, Z. F. et al., 2009. The corrosion resistance of ultra-low carbon bainitic steel. *Corrosion Science,* 51(5), pp. 954-961.

Watson, S. W., Friedersdorf, F. J., Madsen, B. W. & Cramer, S. D., 1995. Methods of measureing wear-corrosion synergism. *Wear,* 181(183), pp. 387-394.

Withers, P. J. & Bhadeshia, H. K., 2001a. Residual Stress. Part 1 - Measurement Techniques. *Materials Science and Technology,* 17(4), pp. 355-365.

Woodmansee, D. E. & Hanratty, T. J., 1969. The mechanism for Removal of Droplets from Liquid Surface by Parallel Air Flow. *Chemical Engineering Science,* Volume 24, pp. 299-307.

Xi, Y. & Xie, Z., 2002. *Corrosion effects of magnesium chloride and sodium chloride on automobile components.* Colorado: the University of Colorado, Department of Civil Environmental and Architectural Engineering. Boulder.

Xu, Y., Huang, Y., Wang, X. & Lin, X., 2016. Experimental study on pipeline internal corrosion based on a new kind of electrical resistance sensor. *Sensors and Actuators B: Chemical,* Volume 224, pp. 37 - 47.

Yaakob, N., 2015. *Top of the Line Corrosion in CO2/H2S Environments.* Oklahoma: the Russ College of Engineering and Technology of Ohio University.

Yang, Z. et al., 2017. A Statistical Study on the Effect of Hydrostatic Pressure on Metastable Pitting Corrosion of X70 Pipeline Steel. *Multidisciplinary Digital Publishing Institute,* 10(1307), pp. 1-14.

Zhang, G., Lu, M., Chai, C. & Wu, Y., 2006. Effect of HCO3- concentration on CO2 corrosion in oil and gas fields. *Journal of University of Science and Technology Beijing Mineral Metallurgy Material,* 13(1), pp. 44-49.

Zhao, L., Yan, Y. & Yan, X., 2020. A semi-empirical model for CO2 erosion-corrosion of carbon steel pipelines in wet gas-solid flow. *Journal of Petroleum Science and Engineering,* Volume 196, pp. 107-992.

Zheng, Y., 2015. *Electrochemical Mechanism and Model of H2S Corrosion of Carbon Steel.* Oklahoma: Russ College of Engineering, Dept of Chemical Engineering, Ohio University.

Zhou, S., Stack, M. M. & Newman, R. C., 1996. Characterization of synergistic effects between erosion and corrosion in an aqueous environment using electrochemical techniques. *Corrosion Science*, 52(12), p. 934.

APPENDIX A

Bubble free SSW in a rectangular test rig duct

Inlet measurement: It takes 6.31 seconds to fill 1 litre

Outlet measurement: It takes 30.4 seconds to fill 1 litre

Calculating inlet flow rate

$$\text{Flow rate} = \frac{Bucket\ Size\ (Litre)}{Time\ Taken\ to\ Fill\ Bucket\ (Seconds)}$$

$$\text{Flow rate} = \frac{1\ L}{6.31\ s}$$

$$= 0.158478605\ L/s$$

divid by 1000 to get m^3

$$\therefore\ Flow\ rate_{\ inlet} = 0.000158479\ m^3/s$$

$$R_e = \frac{Dv\rho}{\mu} = 16421.182 \text{ (turbulent Flow)}$$

$$\text{Friction Factor} = \frac{64}{R_e} = 0.0038974$$

9.1. The Eulerian approach was used to characterize fluid mechanics at position 1

Flow Dynamics from a Circular Pipe to a Rectangular Test Rig Duct

Area of the straight rectangular duct

$A_D =$ 2 x (Width + Height) x Length

$=$ 0.002565 m^2

Hydraulic Diameter

$D = \frac{4\,ab}{2(a+b)} = \frac{2}{(\frac{1}{0.052} + \frac{1}{0.005})} =$ 0.009122807 m

Continuity Law

$A_P V_P = A_D V_D$

$V_D =$ 0.061785031 m/s

$Q = V_D A_D =$ 0.000158479 m^3/s

Head loss due to sudden enlargement

$he_D = \frac{(V_P - V_D)^2}{2g} =$ 0.065333679 m

Eddie Current Cross-Sectional = $P'(A_D + A_P)$

5800.958489 m

Bernoulli Equation

$$\frac{(P_D - P_P)}{\rho g} = \frac{(V_P - V_D)^2}{2g} + he_D$$

$$\frac{(P_D - 2385000\ g/ms^2)}{1024100\ g/m^3 \cdot 9.81\ m/s^2} = \frac{(1.19397176\ \text{m/s} - 0.061785031\ \text{m/s})^2}{2.9.81\ m/s^2} + 0.065333679\ m = P_D = 3697739.297\ g/ms^2$$

Net Force $(F_x) = P_P A_D - P_D A_D$

$=$ -3367.176296 gm/s^2

$R_e = \frac{Dv\rho}{\mu} =$ 596.319166 (Laminor Flow)

Friction Factor $= \frac{96}{R_e} =$ 0.160987614

Hydraulic Radius (R) $= \frac{ab}{b + 2a} =$ 0.004193548 m

9.2. The Eulerian approach was used to characterize fluid mechanics at position 2

Forces Exerted by the fluid in a circular segment

Information

$$A_{D3} = r^2 \cos^{-1}\frac{(r-h)}{r} - (r-h)\sqrt{2rh - h^2}$$

r = 0.013 m

h = 0.005 m

$$A_{D3} = (0.013\ m)^2 \cos^{-1}\frac{(0.013m - 0.005\,m)}{0.013\ m} - (0.013\,m - 0.005\,m)\sqrt{2(0.013\ m)(0.005\,m) - (0.005\,m)^2}$$

A_{D3} = 0.008697135 m^2

$$V_{D3} = \frac{Q}{A_{D3}} = 0.018221932\ m/s$$

Bernoulli Equation

$$\frac{(P_{D3} - P_{D2})}{\rho g} = \frac{(V_{D2} - V_{D3})^2}{2g} + he_{D3} + Z_{D2} - Z_{D3}$$

Head Loss Due to Bend Diffuser

$$he_{D3} = \frac{(V_{D2} - V_{D3})^2}{2g} = 1.02088\text{E-}05\ m$$

$$\frac{(P_{D3} - 3760352.992\ \ g/ms^2)}{1024100\ g/m^3 \,.9.81\ m/s^2} = \frac{(0.032374551\ \text{m/s} - 0.018221932\ \text{m/s})^2}{2.9.81\,m/s^2} + 1.02088\text{E-}05\ m + 0.04451\ m - 0.06068\ m$$

P_{D3} = 3598107.49 g/ms^2

Net Force

$$F_X = P_{D2}A_{D2} - P_{D3}A_{D3}\cos\theta + \rho Q(V_{D2} - V_{D3}\cos\theta)$$

18407.5296 gm/s^2 − 31293.22657 $gm/s^2\cos\theta$ + 162.298 g/m (0.032374551 m/s - 0.018221932 $\cos\theta$) m/s

18412.7839 gm/s^2 + -31296.18395 $gm/s^2\cos\theta$

$$F_Y = -P_{D3}A_{D3}\sin\theta - \rho V_{D3}^2 A_{D3}\sin\theta$$

− 31293.2266 $\sin\theta$ − 2.957382075 $gm/s^2\sin\theta$

-31296.18395 $gm/s^2\sin\theta$

$$\tan\theta = \frac{F_Y}{F_X} = \frac{-31296.18395\ gm/s^2\sin\theta}{18412.78388\ gm/s^2 - 31296.18395\cos\theta\ gm/s^2}$$

θ = 72° 53' 32.06"

$\therefore F_X$ = 9206.391978 gm/s^2 F_Y = -29571.90754 gm/s^2

$$F_R = \sqrt{F_X^2 + F_Y^2} = 30971.848\ gm/s^2$$

$$R_e = \frac{Dv\rho}{\mu} = 175.8692559$$ (Laminor Flow)

Friction Factor = $\frac{96}{R_e}$ = 0.545860045

9.3. The Eulerian approach was used to characterize fluid mechanics at position 3

Kinematic of Fluid Flow in the Horizontal Sector of the Rectangula

Area of the straight rectangular duct

A_{D5} = 2 x (Width + Height) x Length

= 0.00137 m^2

Information

$Length_1$= 0.012 m

Head loss due to sudden enlargement

$V_{D5} = \frac{Q}{A_{D5}}$ = 0.115846934 m^3/s

$he_{D5} = \frac{(V_{D4} - V_{D5})^2}{2g}$ = 0.000343865 m

Bernoulli Equation

$\frac{(P_{D5} - P_{D4})}{\rho g} = \frac{(V_{D4} - V_{D5})^2}{2g} + he_D$

$\frac{(P_{D5} - 3710571.644\ g/ms^2)}{1024100\ g/m^3 \,.\, 9.81\ m/s^2} = \frac{(0.033709098\ \text{m/s} - 0.115846934\ \text{m/s})^2}{2.9.81\, m/s^2} + 0.000343865\ m = P_{D5} =$ 3717480.861 g/ms^2

Net Force (F_x) = $P_{D4}A_{D5} - P_{D5}A_{D5}$

= -9.451809799 gm/s^2

$R_e = \frac{D v \rho}{\mu}$ = 1118.098436 (Laminor Flow)

Friction Factor = $\frac{96}{R_e}$ = 0.08586006

9.4. The Eulerian approach was used to characterize fluid mechanics at position 4

Kinematic of Fluid Flow in the Horizontal Sector of the Rectangular Test I

Area of the straight rectangular duct

A_{D9} = 2 x (Width + Height) x Length

= 0.00148 m^2

Information

$Length_1$= 0.013 m

Head loss due to sudden enlargement

$V_{D9} = \frac{Q}{A_{D9}}$ = 0.106935631 m/s

$he_{D9} = \frac{(V_{D8} - V_{D9})^2}{2g}$ = 0.000328899 m

Bernoulli Equation							
$\frac{(P_{D9}-P_{D8})}{\rho g}=\frac{(V_{D8}-V_{D9})^2}{2g}+he_D$							
$\frac{(P_{D9}-3722308.052\ g/ms^2)}{1024100\ g/m^3\ .9.81\ m/s^2}=\frac{(0.02660511\ \text{m/s}-0.106935631\ \text{m/s})^2}{2.9.81\ m/s^2}+0.000328899\ m=P_{D5}=$							3728916.562
Net Force (F_x) =	$P_{D8}A_{D9}-P_{D9}A_{D9}$				$R_e=\frac{Dv\rho}{\mu}$	1032.090864	
=	-9.79381146 gm/s^2					(Laminor Flow)	
Friction Factor =	$\frac{96}{R_e}=$	0.093015066					

9.5. Hydrodynamic Parameters

	SSW				AMD			
	Region 2	Region 5	Region 7	Region 11	Region 2	Region 5	Region 7	Region 11
Corrosion Rate (24 Hours)	0,130661	0,0187674	0,363642	0,185048	0,51283	0,281751	6,30835	1,86997
Corrosion Rate (192 Hours)	0,0701856	0,203139	1,61E-04	0,029223				Disir
Time	0,364165875	1,097578437	0,10358496	0,12156846	0,364165875	1,097578437	0,10358496	0,12156846
Velocity	0,061785031	0,018221932	0,115846934	0,106935631	0,061785031	0,018221932	0,115846934	0,106935631
he_D	0,065333679	1,02088E-05	0,000343865	0,000328899	0,065333679	1,02088E-05	0,000343865	0,000328899
Pressure	3697739,297	3598107,488	3717480,861	3728916,562	3632457,763	3533682,179	3652029,671	3663367,095
Net Force	-3367,176296	9206,391978	-9,451809799	-9,79381146	-3338,239162	9045,270555	-9,37058201	-9,709644548
R_e	596,3191661	175,8692559	1118,098436	1032,090864	610,7537284	180,126365	1145,163241	1057,073761
Friction Factor	0,160987614	0,545860045	0,085860061	0,093015066	0,157182831	0,532959181	0,083830843	0,090816747
Pressure Gradient	859403,7949	-8112275,191	575768,1407	286839735,5	852018,1755	-8042559,212	570820,0542	281797468,8
Resultant Torque	-0,739730634	-0,009632332	0,055903361	0,054673295	-0,733373473	-0,009549553	0,055422934	0,054203439
Pressure Drop at Head	0,130667359	-0,016149582	0,000687729	0,000657797	0,130667359	-0,016149582	0,000687729	0,000657797
Major Energy Loss	0,000309011	7,75996E-10	0,000309011	0,000309011	0,000301708	7,64223E-10	0,000301708	0,000301708
Power Loss	0,000101573	1,58714E-08	5,34598E-07	5,11331E-07	0,000101573	1,58714E-08	5,34598E-07	5,11331E-07
Shear Stress	244668,256	-34019,21854	2414,511558	2131,777341	242565,6046	-33726,86121	2393,761518	2113,457087
Viscosity Force	627,5740767	-295,8697363	3,303051811	3,159294019	622,1807758	-293,3270651	3,274665756	3,132143403
Shear Force	157,7751149	-19,49991371	0,830402973	0,794261579	156,4192134	-19,33233365	0,823266584	0,787435784
Torque Resistance	0,000734329	0,002489888	0,000391642	0,000424279	0,000716974	0,002431042	0,000382386	0,000414252
Resistance	23332734962	22704058251	23457304234	23529463507	22920808485	22297534550	23044307223	23115846367
Drag Co-efficient	0,002226995	0,007551064	0,001187731	0,001286708	0,002174362	0,007372602	0,00115966	0,001256298
Skin Friction Co-efficient	0,02719122	0,050069484	0,019857659	0,020668507	0,02686798	0,049474275	0,019621598	0,020422807
Drag Force	0,011165691	0,011165691	0,011165691	0,011165691	0,010808112	0,010808112	0,010808112	0,010808112
Water Retardation	3,108986335	0,012894403	-0,792951367	-0,66078423	3,108986335	0,012894403	-0,792951367	-0,66078423
Retarding Force	183,7515735	2,296940798	-13,33080151	-13,03747809	182,1724332	2,277201147	-13,2162381	-12,92543547
Loss of Kinetic Energy	0,112810312	0,029573821	0,112810312	0,112810312	0,111840833	0,029319667	0,111840833	0,111840833
Pressure Intensity	3909,389199	340,0409531	13743,9464	11710,81824	3875,792349	337,1186795	13625,83248	11610,17678
Gain of Strain Energy	1,8847E-10	4,29757E-12	6,62589E-10	5,64573E-10	1,85244E-10	4,22402E-12	6,5125E-10	5,54911E-10
Strain Energy Stored in a Pipe per unit Volume	4,73201E-06	8,95015E-09	1,46215E-05	1,06155E-05	4,65103E-06	8,79697E-09	1,43712E-05	1,04339E-05
Total Strain Energy in a Pipe	2,39484E-11	5,46082E-13	8,41937E-11	7,1739E-11	6,64353E+11	5,36736E-13	8,27528E-11	7,05113E-11
Loss of Kinetic Energy of Water	90092240,43	28208080,94	168922950,8	165539465,6	89704283,83	28086610,87	168195532,2	164826617
Stress Magnitude	11145,18851	969,414998	39182,30334	33386,10462	11049,40801	961,0839548	38845,57504	33099,1882
Froude's Number	0,131509616	0,041138166	0,337644295	0,299444443	0,131509616	0,041138166	0,337644295	0,299444443
Euler's Number	0,032515191	0,009721394	0,060803889	0,056040537	0,032664797	0,009767371	0,061082158	0,056296215
Weber's Number	0,072215151	0,020356087	0,098621756	0,094607315	0,072547421	0,020452359	0,0990731	0,095038949
Mach's Number	6,23763E-05	1,20547E-05	7,66386E-05	7,07434E-05	6,16661E-05	1,20028E-05	7,63086E-05	7,04387E-05
Sh_L	121,8328354	66,16372235	166,8264804	160,2816979	121,8277858	66,1609801	166,8195661	160,2750548
j_D	556,1762015	1885,82437	296,6273075	321,3462498	543,5306857	1842,947271	289,8830324	314,0399517
j_H	0,080493807	0,272930023	0,042930031	0,046507533	0,078591415	0,266479591	0,041915422	0,045408373
Nusselt Number	8,019905548	4,355367766	10,98170794	10,55088371	8,028806861	4,360201799	10,99389657	10,56259416
St	0,013893611	0,025034742	0,010146459	0,010560769	0,0140296	0,024737137	0,010245771	0,010664137

APPENDIX B

10.1. Metallographic Examination

The mild steel coupon sample was prepared and examined in the as-etched condition to investigate the average grain size using the ASTM E 112-12 rating.

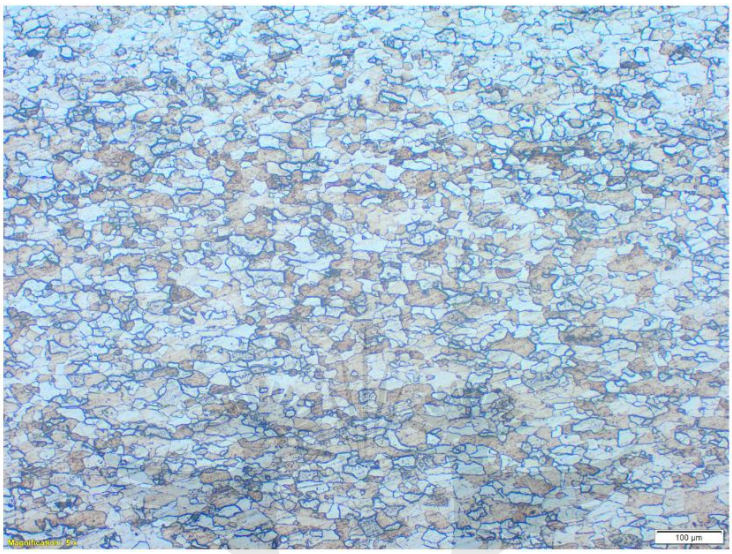

Figure 37: The optical microscope image of the as-received mild steel in the transverse direction, 100X Magnification

Figure 37 shows evidence of equiaxed grain shape with an average ASTM grain size of 8.190 μm (ASTM E 112-12), which in this case indicates a recrystallization process after hot rolling. The microstructure was characterized by a proeutectoid ferrite and eutectoid perlite that contain lamella structure of eutectoid ferrite and cementite (Fe_3C). This microstructure indicates that the hypoeutectoid steel was cooled below the austenitic temperature line (Ae_3) region. Thus, nucleating the ferritic grain at the austenitic grains boundary and growing to form a blocky structure with a faceted interface. With each nucleation site (corner, edge and boundary) having a distinct crystallography potency.

It is well documented that the observable difference in corrosion rate could be attributed to precipitation of ferrite and carbide microstructure (Wang, et al., 2008; Hao, et al., 2012; Sun, et al., 2012). In a manner that micro-galvanic cell is triggered by the ferrite-cementite morphology, with cementite acting as a cathode and ferrite as an anode.

Hence, steel with homogenous microstructure exhibits substantial corrosion resistance (Guo, et al., 2008; Wang, et al., 2009; Sun, et al., 2012). The homogeneity of the grain size decreases with increasing carbon content due to grain growth. Hence, during the heat treatment process such as normalizing, the ferrite (anodic) precipitate and the difference in grain size increases the rate of corrosion.

Consequently, proeutectoid ferrite dissolves preferentially, leaving behind the cementite (Fe_3C) in the eutectoid pearlite to facilitate $FeCO_3$ scales formation between the lamellar structure (Sun, et al., 2012). The occurrence indicates that pearlite (ferrite and cementite) increases with increasing carbon content, which increases the chances of steel corrosion (Clover, et al., 2005). When compared to the martensitic structure, the normalized structure is less susceptible to corrosion attack. This vulnerability is attributed to high metastable martensitic structure, as a result of the combined effect of ferrite precipitation, transformation stress and carbide precipitation. Quenching limits ferrite grain growth, giving rise to allotriomorphic ferrite (proeutectoid ferrite) precipitate at preceding austenite grain boundaries in the pearlite matrix (Igwemezie & Ovri , 2013).

Although various researchers have over the years shown that corrosion is a system property, others have argued that material properties such as the potential difference generated between the microstructure play a vital role in the corrosion mechanism (Van Rossum, 1959; Woodmansee & Hanratty, 1969; Ishii & Grolmes, 1975; Kataoka, et al., 1983; Han & Gabriel, 2007). For instance, the corrosion rate of a binary system decreases with a time of exposure in all active media.

Figure 38 and Figure 61 shows the surface behaviour of mild steel inside the multi specimen electrochemical test-rigs prototype, thus, from position 1 to 4 after 24 hours and 192 hours of a continuously flowing MME/SSW solution.

10.2. Micrographic characterization of mild steel at position 1 during 24H MME bulk flow

(a)

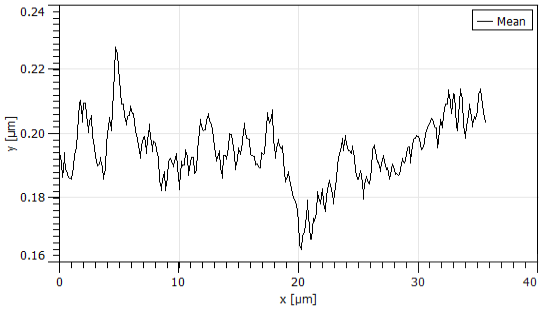

(b)

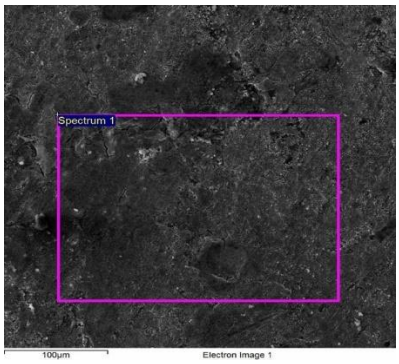

(c)

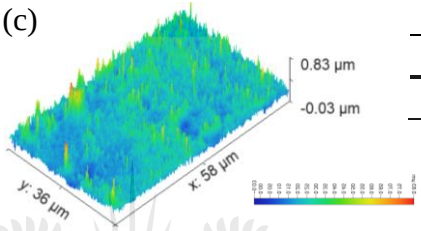

(d)

Element	Weight%	Atomic%
O K	21.810	48.920
Mg K	0.610	0.900
Al K	0.340	0.460
S K	3.100	3.470
Cl K	0.570	0.580
Ca K	0.400	0.360
Mn K	0.310	0.200
Fe K	51.050	32.800
Cu K	21.810	12.320
Total	100.000	

Figure 38: Microstructure characterization of mild steel with multi-layered corrosion film after 24H MME bulk flow; (a) Surface profile (thickness); (b) Corrosion product layer on the surface - having 194.700 ± 10.140 nm average surface roughness; (c) 3D SEM/EDX image; (d) Elemental composition of the corroded surface.

(a)

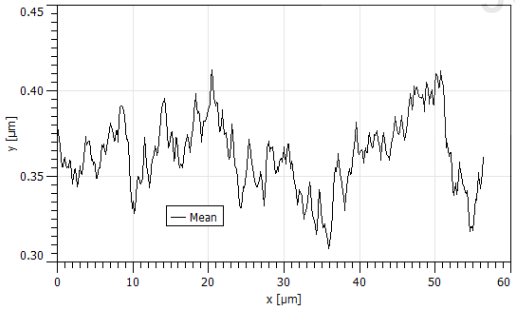

(b)

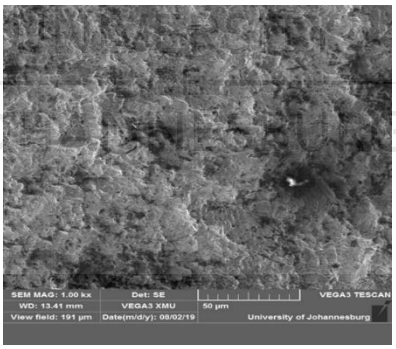

(c)

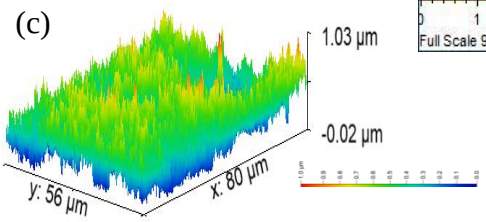

(d)

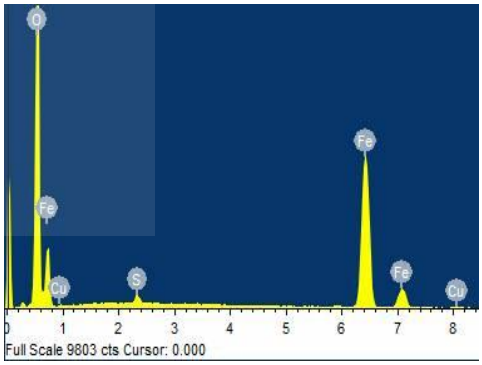

Figure 39: Microstructure characterization of mild steel without corrosion film (after corrosion film was removed); (a) Surface profile (thickness); (b) Multiple wear sites on the surface - having 0.363 ± 0.021 µm average surface roughness; (c) 3D SEM/EDX image; (d) Elemental composition of the corroded surface.

10.3. Micrographic characterization of mild steel at position 1 during 24H SSW bulk flow

(a)

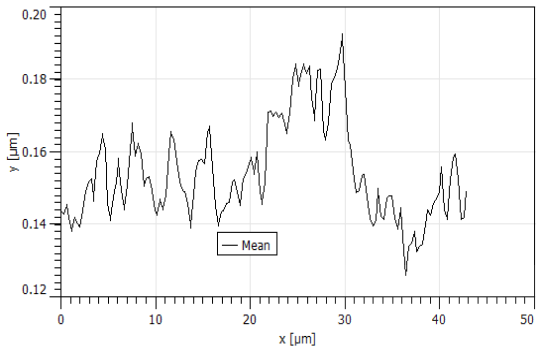

(b)

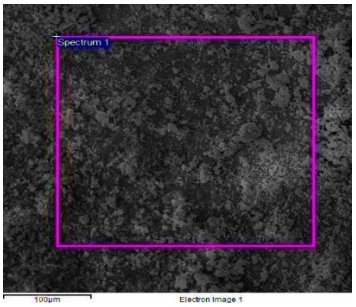

(c)

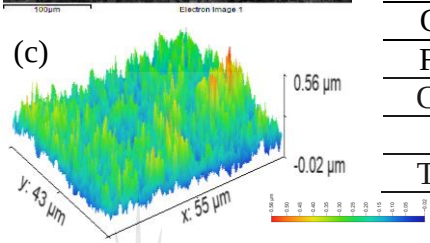

(d)

Element	Weight%	Atomic%
O K	13.740	35.360
Al K	1.230	1.880
Si K	0.520	0.770
S K	1.330	1.700
Cl K	0.300	0.340
Fe K	70.010	51.610
Cu K	12.870	8.340
Total	100.000	

Figure 40: Microstructure characterization of mild steel with multi-layered corrosion film after 24H SSW bulk flow shows (a) Surface profile (thickness); (b) Corrosion product layer on the surface – having 154.100 ± 16.640 nm average surface roughness; (c) 3D SEM/EDX image; (d) Elemental composition of the corroded surface.

(a)

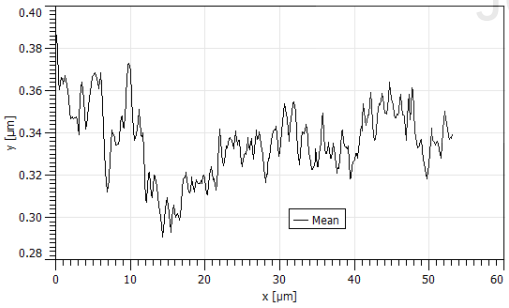

(b)

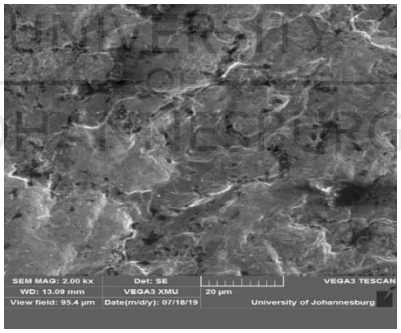

(c)

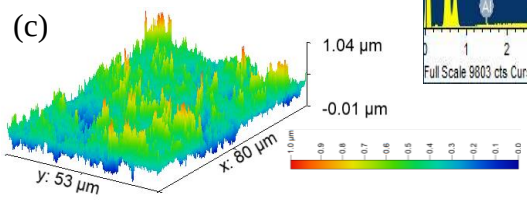

(d)

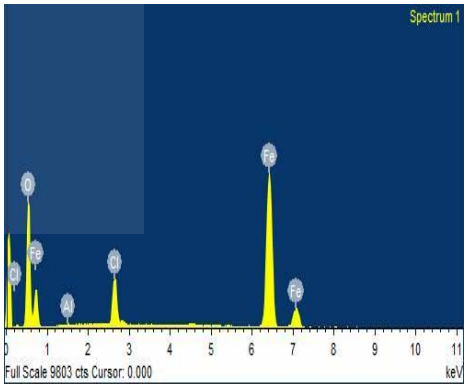

Figure 41: Microstructure characterization of mild steel without corrosion film (after corrosion film was removed); (a) Surface profile (thickness); (b) Material detachment on the surface – having 335.800 ± 16.860 nm average surface roughness; (c) 3D SEM/EDX image; (d) Elemental composition of the corroded surface.

10.4. Micrographic characterization of mild steel at position 1 during 192H SSW bulk flow

(a)

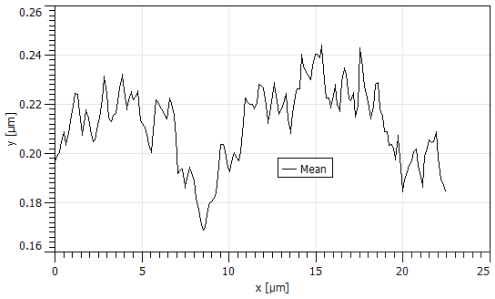

(b)

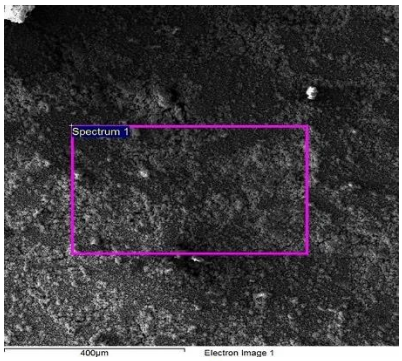

(c)

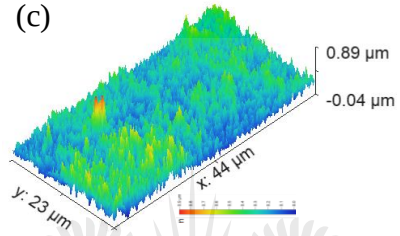

(d)

Element	Weight%	Atomic%
OK	49.950	73.150
Na K	1.000	1.020
Mg K	1.410	1.360
Al K	1.360	1.180
Si K	0.520	0.430
S K	0.580	0.420
Cl K	1.200	0.790
Ca K	19.300	11.280
Fe K	24.680	10.360
Totals	100.000	

Figure 42: Microstructure characterization of mild steel with multi-layered corrosion film after 192H SSW bulk flow shows (a) Surface profile (thickness); (b) Corrosion product layer on the surface – having 211.600 ± 15.660 nm average surface roughness; (c) 3D SEM/EDX image; (d) Elemental composition of the corroded surface.

(a)

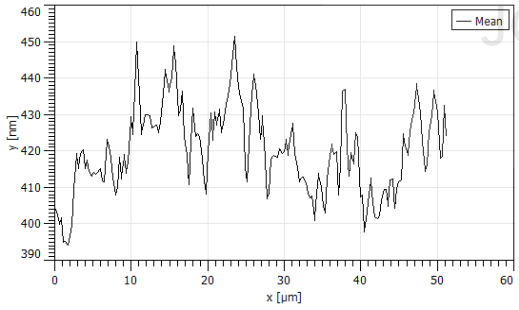

(b)

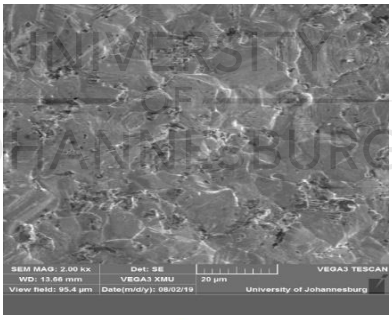

(c)

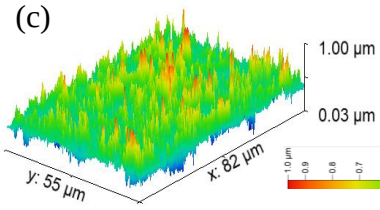

(d)

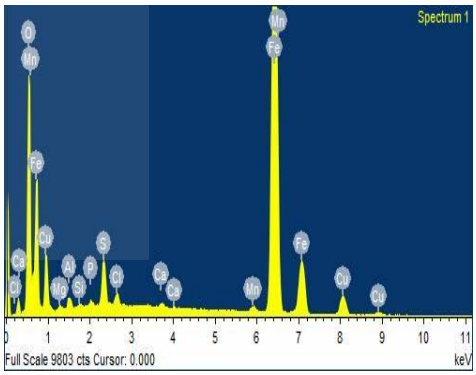

Figure 43: Microstructure characterization of mild steel without corrosion film (after corrosion film was removed); (a) Surface profile (thickness); (b) Material detachment on the surface – having 154.100 ± 16.640 nm average surface roughness; (c) 3D SEM/EDX image; (d) Elemental composition of the corroded surface.

10.5. Micrographic characterization of mild steel at position 2 during 24H MME bulk flow

(a)

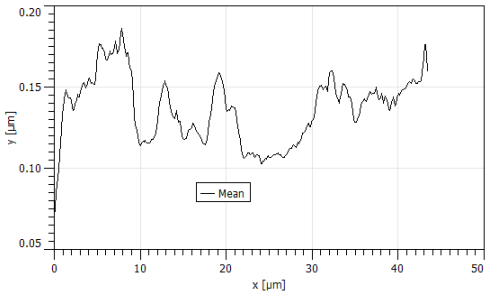

(b)

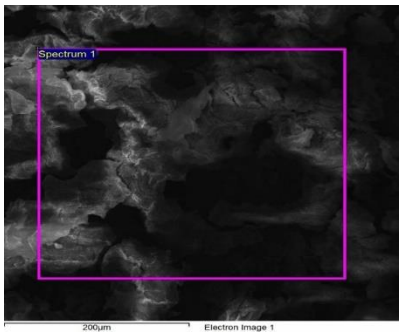

(c)

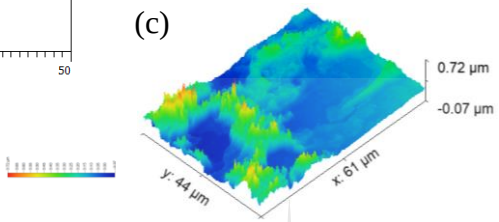

(d)

Element	Weight%	Atomic%
O K	13.740	35.360
Al K	1.230	1.880
Si K	0.520	0.770
S K	1.330	1.700
Cl K	0.300	0.340
Fe K	70.010	51.610
Cu K	12.870	8.340
Total	100.000	

Figure 44: Microstructure characterization of mild steel with multi-layered corrosion film after 24H MME bulk flow; (a) Surface profile (thickness); (b) Corrosion product layer on the surface - having 136.600 ± 20.640 nm average surface roughness; (c) 3D SEM/EDX image; (d) Elemental composition of the corroded surface.

(a)

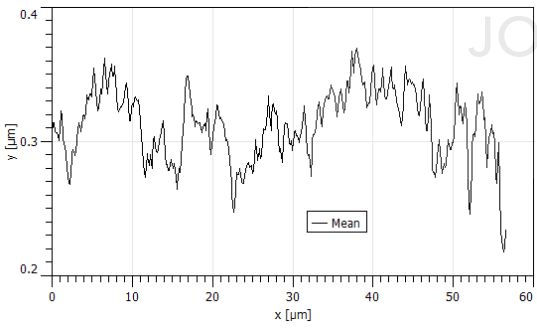

(b)

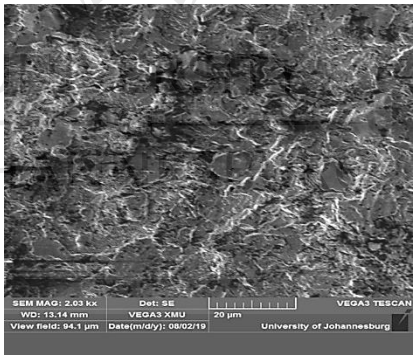

(c)

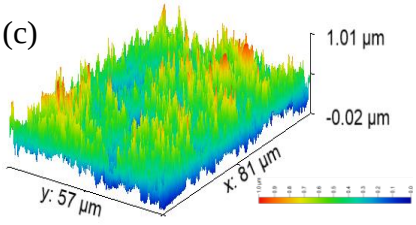

(d)

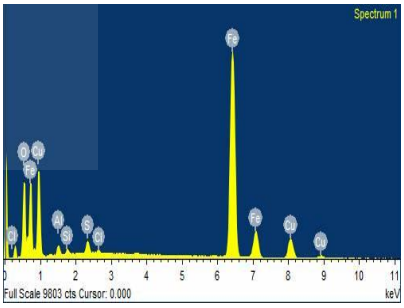

Figure 45: Microstructure characterization of mild steel without corrosion film (after corrosion film was removed); (a) Surface profile (thickness); (b) Multiple wear sites on the surface - having 312.700 ± 26.390 nm average surface roughness; (c) 3D SEM/EDX image; (d) Elemental composition of the corroded surface.

10.6. Micrographic characterization of mild steel at position 2 during 24H SSW bulk flow.

(a)

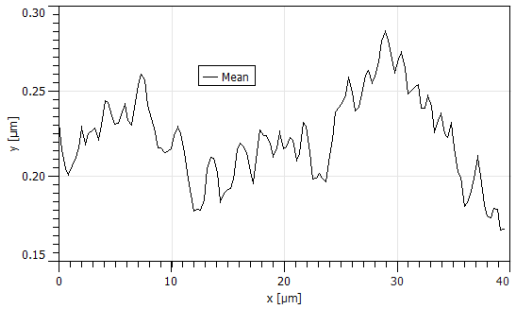

(b)

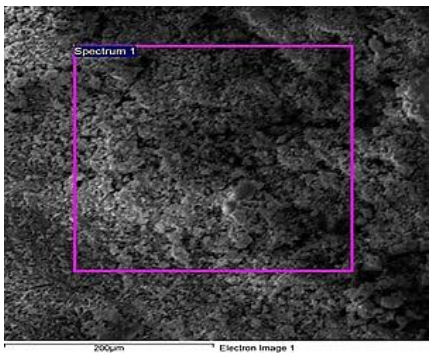

(c)

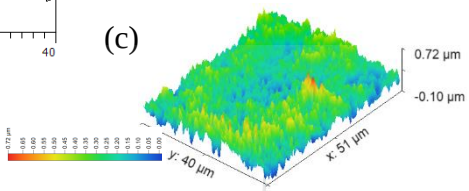

(d)

Element	Weight%	Atomic%
OK	20.750	59.340
Al K	0.160	0.280
Cl K	4.240	5.480
Fe K	42.610	34.910
Total	67.770 (retest required)	

Figure 46: Microstructure characterization of mild steel with multi-layered corrosion film after 24H SSW bulk flow shows (a) Surface profile (thickness); (b) Corrosion product layer on the surface – having 222.500 ± 25.250 nm average surface roughness; (c) 3D SEM/EDX image; (d) Elemental composition of the corroded surface.

(a)

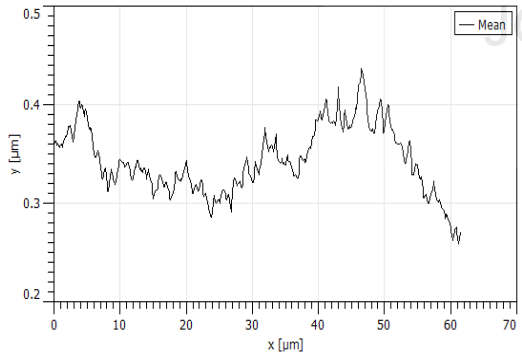

(b)

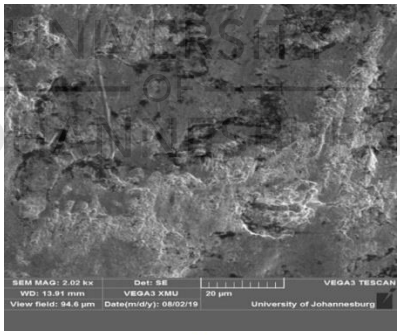

(c)

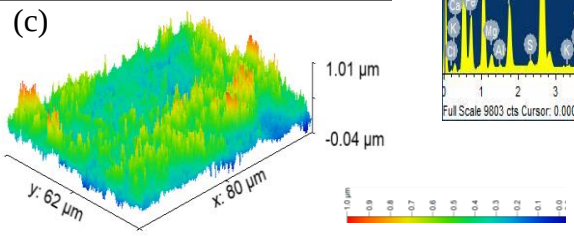

(d)

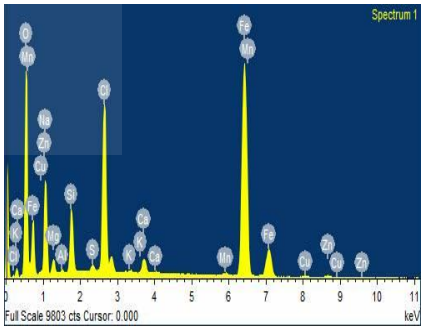

Figure 47: Microstructure characterization of mild steel without corrosion film (after corrosion film was removed); (a) Surface profile (thickness); (b) Material detachment on the surface – having 343.400 ± 34.060 nm average surface roughness; (c) 3D SEM/EDX image; (d) Elemental composition of the corroded surface.

10.7. Micrographic characterization of mild steel at position 2 during 192H SSW bulk flow.

(a)

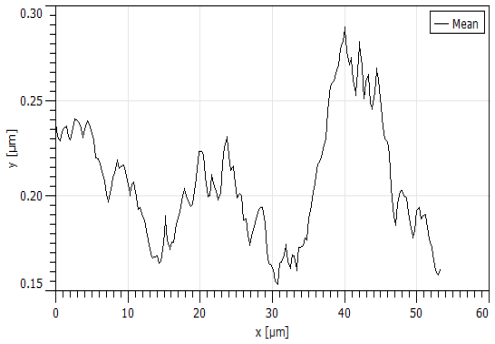

(b)

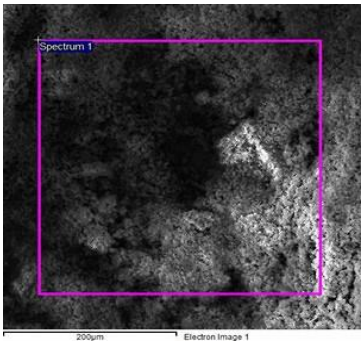

(c)

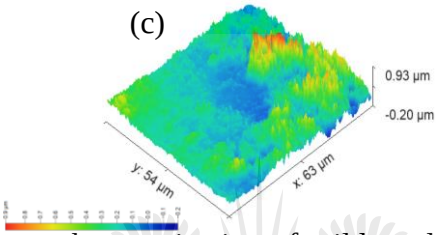

(d)

Element	Weight%	Atomic%
Na K	9.300	11.850
Mg K	1.090	1.310
Si K	6.680	6.970
S K	0.300	0.270
Cl K	11.030	9.120
Ca K	1.100	0.800
Mn K	2.020	1.080
Fe K	41.030	21.530
Zn K	1.530	0.680
Br L	0.760	0.280
O	25.170	46.100
Total	100.000	

Figure 48: Microstructure characterization of mild steel with multi-layered corrosion film after 192H SSW bulk flow shows (a) Surface profile (thickness); (b) Corrosion product layer on the surface – having 207.400 ± 31.460 nm average surface roughness; (c) 3D SEM/EDX image; (d) Elemental composition of the corroded surface.

(a)

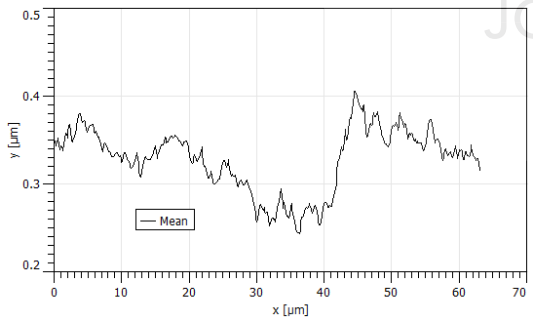

(b)

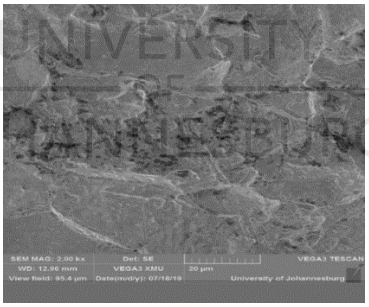

(c)

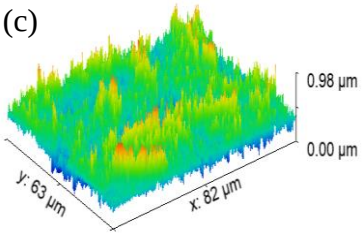

(d)

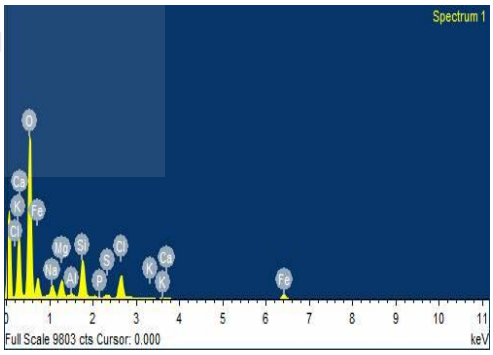

Figure 49: Microstructure characterization of mild steel without corrosion film (after corrosion film was removed); (a) Surface profile (thickness); (b) Material detachment on the surface – having 326.100 ± 35.290 nm average surface roughness; (c) 3D SEM/EDX image; (d) Elemental composition of the corroded surface.

10.8. Micrographic characterization of mild steel at position 3 during 24H MME bulk flow.

(a)

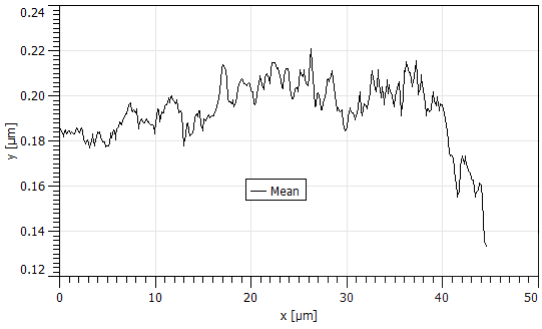

(b)

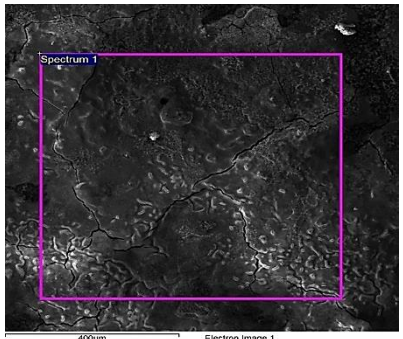

(c)

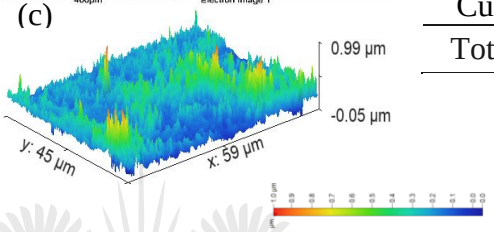

(d)

Element	Weight%	Atomic%
OK	44.160	73.250
S K	0.810	0.670
Fe K	53.990	25.650
Cu K	1.040	0.440
Totals	100.000	

Figure 50: Microstructure characterization of mild steel with multi-layered corrosion film after 24H MME bulk flow; (a) Surface profile (thickness); (b) Corrosion product layer on the surface - having 193.200 ± 13.720 nm average surface roughness; (c) 3D SEM/EDX image; (d) Elemental composition of the corroded surface.

Unfortunately, 24H MME coupon samples were fragile and disintegrated during handling due to layer-type corrosion (exfoliation corrosion). As such, there was no as-cleaned microstructural characterization for 24H MME coupon samples.

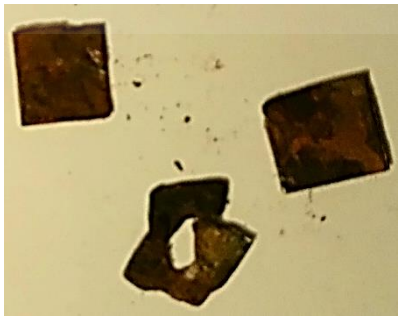

Figure 51: Disintegration of mild steel at position 3

10.9. Micrographic characterization of mild steel at position 3 during 24H SSW bulk flow.

(a)

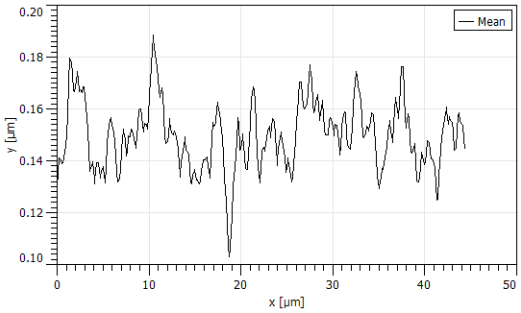

(b)

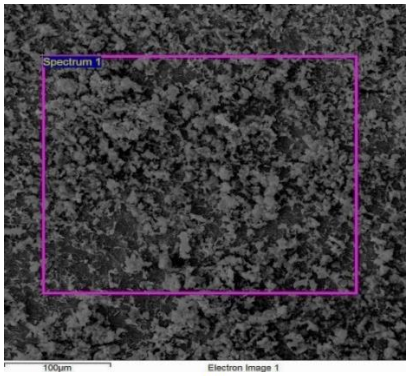

(c)

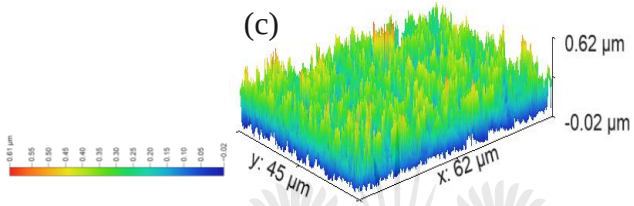

(d)

Element	Weight%	Atomic%
OK	21.350	48.130
Mg K	0.290	0.430
Al K	0.670	0.890
Si K	0.230	0.290
S K	2.240	2.520
Cl K	0.640	0.650
Ca K	0.250	0.220
Mn K	0.510	0.340
Fe K	59.100	38.170
Cu K	14.720	8.360
Total	100.000	

Figure 52: Microstructure characterization of mild steel with multi-layered corrosion film after 24H SSW bulk flow shows (a) Surface profile (thickness); (b) Corrosion product layer on the surface – having 149.300 ± 12.760 nm average surface roughness; (c) 3D SEM/EDX image; (d) Elemental composition of the corroded surface.

(b)

(d)

(a)

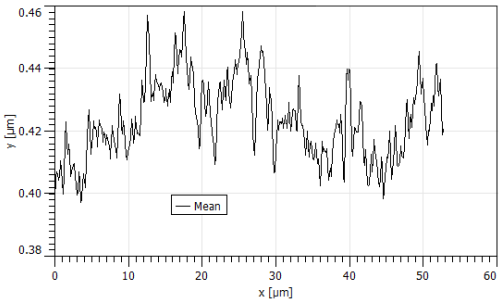

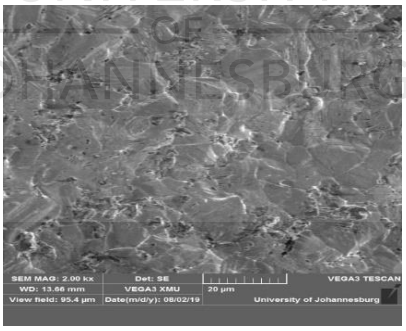

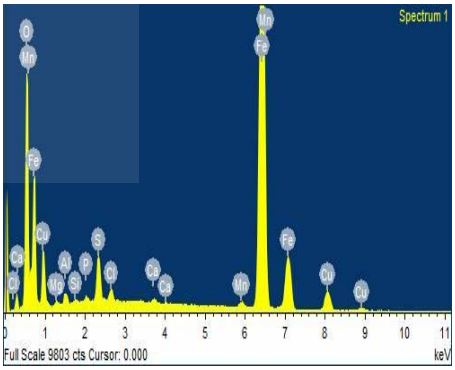

(c)

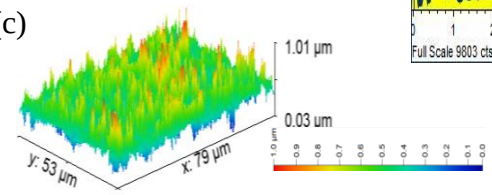

Figure 53: Microstructure characterization of mild steel without corrosion film (after corrosion film was removed); (a) Surface profile (thickness); (b) Material detachment on the surface – having 0.423 ± 0.013 µm average surface roughness; (c) 3D SEM/EDX image; (d) Elemental composition of the corroded surface.

10.10. Micrographic characterization of mild steel at position 3 during 192H SSW bulk flow.

(a)

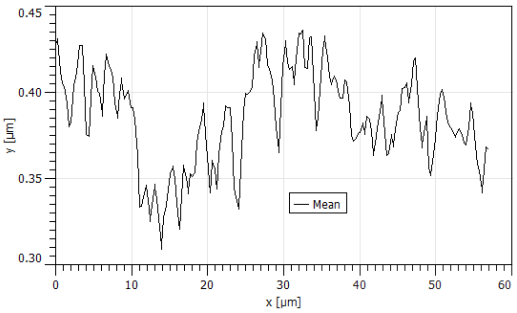

(b)

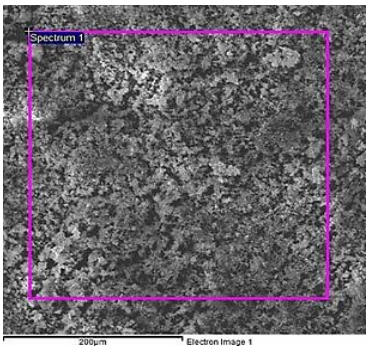

(c)

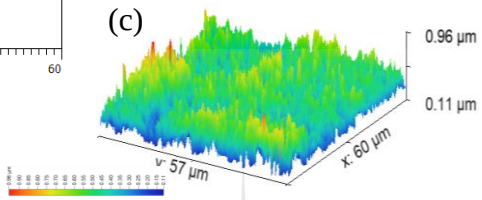

(d)

Element	Weight%	Atomic%
Na K	12.550	15.610
Mg K	1.710	2.020
Al K	0.220	0.230
Si K	5.600	5.710
S K	0.280	0.250
Cl K	14.360	11.580
K K	0.270	0.200
Ca K	1.540	1.100
Mn K	2.920	1.520
Fe K	33.540	17.170
Cu K	0.610	0.270
Zn K	2.120	0.930
O	24.290	43.420
Total	100.000	

Figure 54: Microstructure characterization of mild steel with multi-layered corrosion film after 192H SSW bulk flow shows (a) Surface profile (thickness); (b) Corrosion product layer on the surface – having 0.385 ± 0.028 µm average surface roughness; (c) 3D SEM/EDX image; (d) Elemental composition of the corroded surface.

(a)

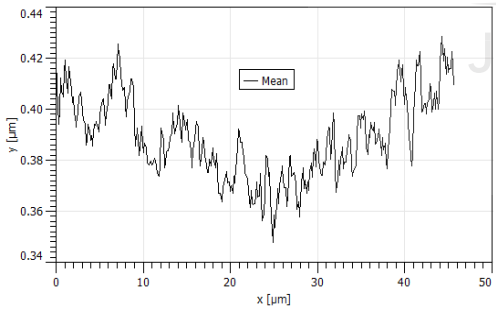

(b)

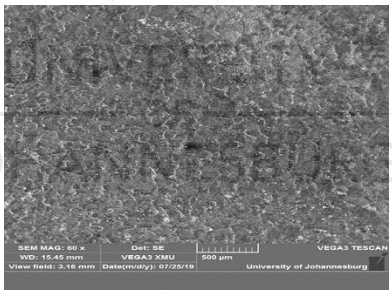

(c)

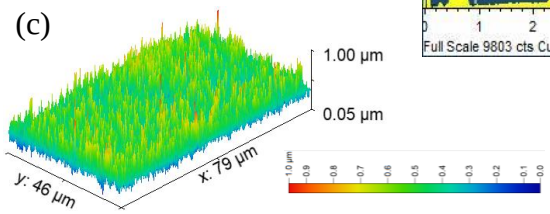

(d)

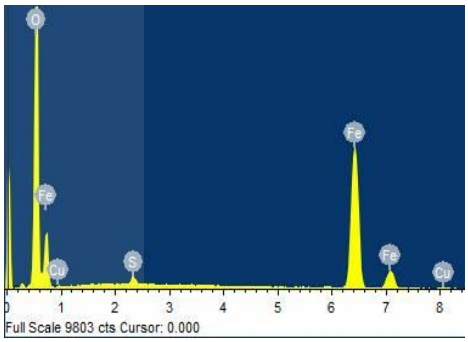

Figure 55: Microstructure characterization of mild steel with multi-layered corrosion film after 192H SSW bulk flow shows (a) Surface profile (thickness); (b) Corrosion product layer on the surface – having 0.390 ± 0.016 µm average surface roughness; (c) 3D SEM/EDX image; (d) Elemental composition of the corroded surface.

10.11. Micrographic characterization of mild steel at position 4 during 24H MME bulk flow.

(a)

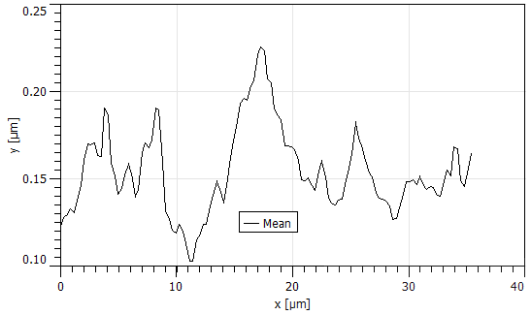

(b)

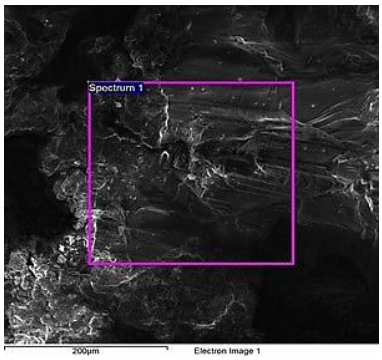

(c)

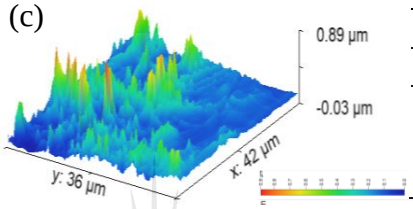

(d)

Element	Weight%	Atomic%
O K	6.810	28.960
Na K	12.860	38.040
Mg K	0.370	1.020
Si K	0.510	1.240
S K	0.110	0.230
Cl K	15.460	29.660
Ca K	0.140	0.230
Fe K	0.500	0.610
Total	36.76 (retest required)	

Figure 56: Microstructure characterization of mild steel with multi-layered corrosion film after 24H MME bulk flow; (a) Surface profile (thickness); (b) Corrosion product layer on the surface - having 154.100 ± 24.420 nm average surface roughness; (c) 3D SEM/EDX image; (d) Elemental composition of the corroded surface.

(a)

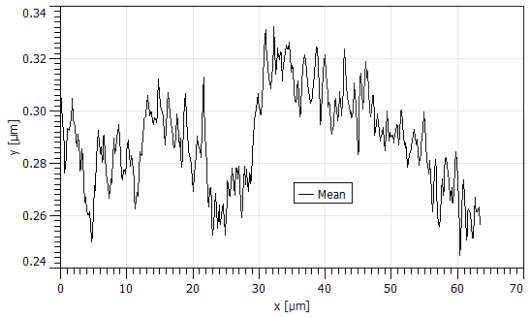

(b)

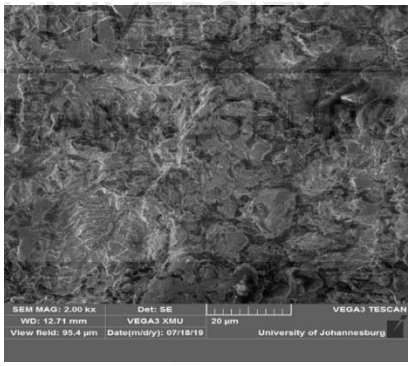

(c)

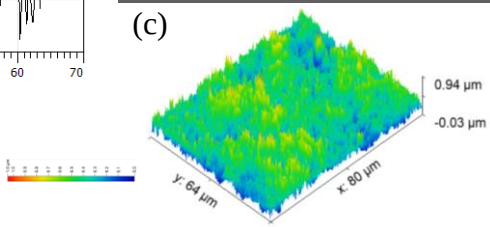

(d)

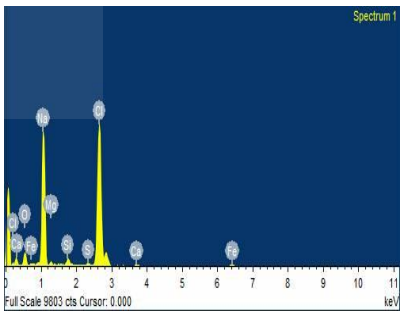

Figure 57: Microstructure characterization of mild steel without corrosion film (after corrosion film was removed); (a) Surface profile (thickness); (b) Multiple wear sites on the surface - having 288.900 ± 18.370 nm average surface roughness; (c) 3D SEM/EDX image; (d) Elemental composition of the corroded surface.

10.12. Micrographic characterization of mild steel at position 4 during 24H SSW bulk flow.

(a)

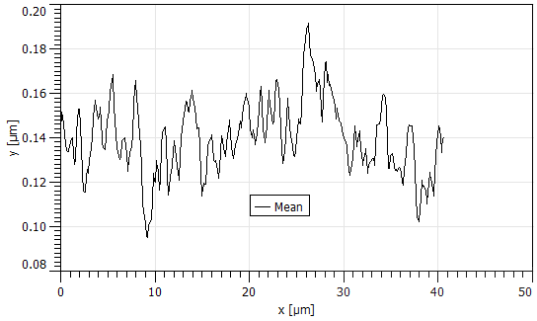

(b)

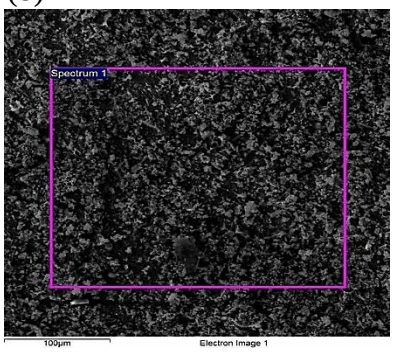

(c)

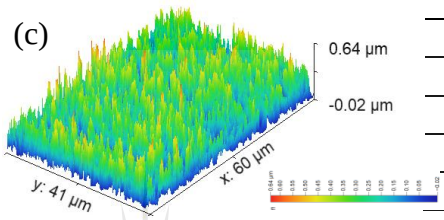

(d)

Element	Weight%	Atomic%
O K	21.350	48.130
Mg K	0.290	0.430
Al K	0.670	0.890
Si K	0.230	0.290
S K	2.240	2.520
Cl K	0.640	0.650
Ca K	0.250	0.220
Mn K	0.510	0.340
Fe K	59.100	38.170
Cu K	14.720	8.360
Total	100.000	

Figure 58: Microstructure characterization of mild steel with multi-layered corrosion film after 24H SSW bulk flow shows (a) Surface profile (thickness); (b) Corrosion product layer on the surface – having 139.900 ± 16.270 nm average surface roughness; (c) 3D SEM/EDX image; (d) Elemental composition of the corroded surface.

(a)

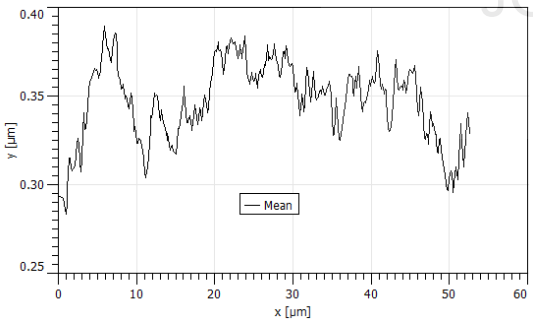

(b)

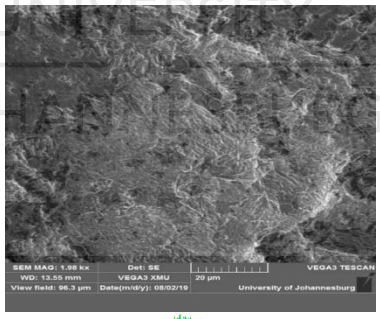

(c)

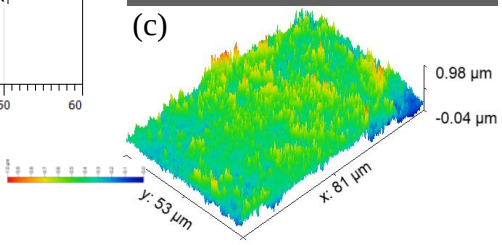

(d)

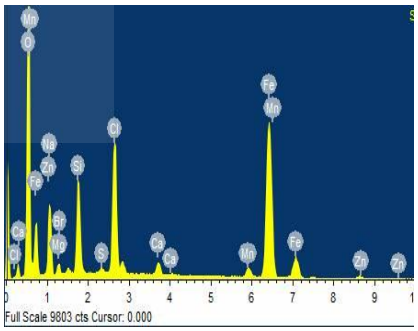

Figure 59: Microstructure characterization of mild steel without corrosion film (after corrosion film was removed); (a) Surface profile (thickness); (b) Material detachment on the surface – having 346.800 ± 22.160 nm average surface roughness; (c) 3D SEM/EDX image; (d) Elemental composition of the corroded surface.

10.13. Micrographic characterization of mild steel at position 4 during 192H SSW bulk flow.

(a)

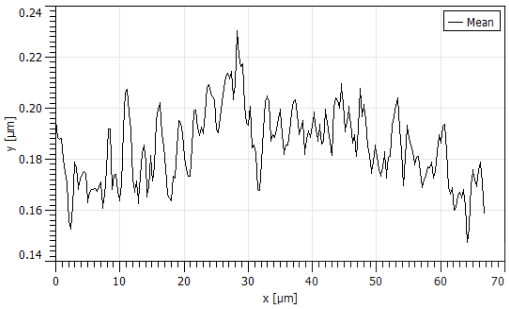

(b)

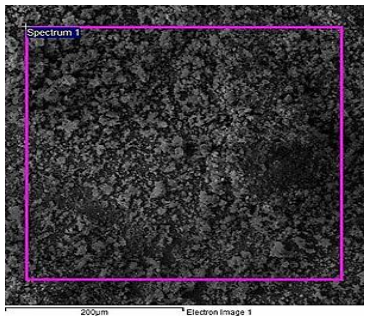

(c)

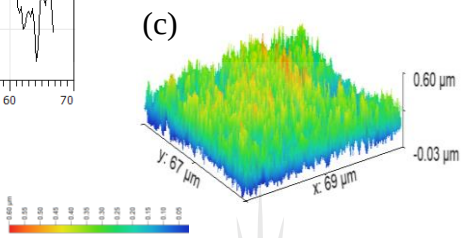

(d)

Element	Weight%	Atomic%
Na K	10.570	13.780
Mg K	1.290	1.590
Al K	0.190	0.210
Si K	3.730	3.980
S K	0.340	0.310
Cl K	11.250	9.510
K K	0.150	0.120
Ca K	1.120	0.840
Mn K	0.380	0.200
Fe K	45.780	24.570
Cu K	0.610	0.290
Zn K	1.020	0.470
O	23.560	44.130
Total	100.000	

Figure 60: Microstructure characterization of mild steel with multi-layered corrosion film after 192H SSW bulk flow shows (a) Surface profile (thickness); (b) Corrosion product layer on the surface – having 184.900 ± 14.420 nm average surface roughness; (c) 3D SEM/EDX image; (d) Elemental composition of the corroded surface.

(a)

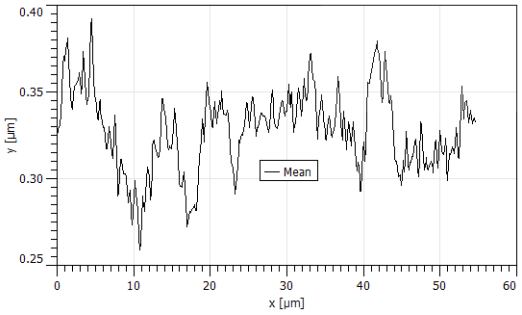

(b)

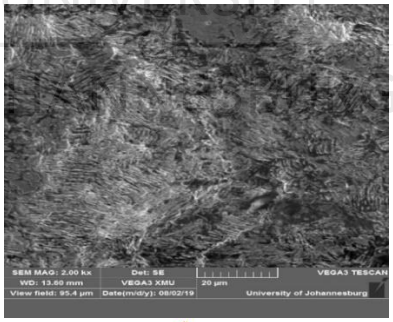

(c)

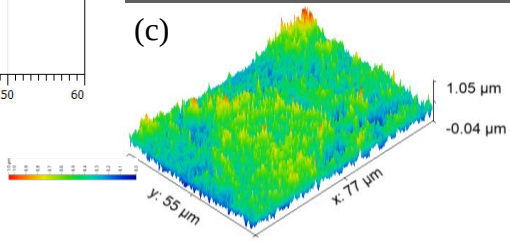

(d)

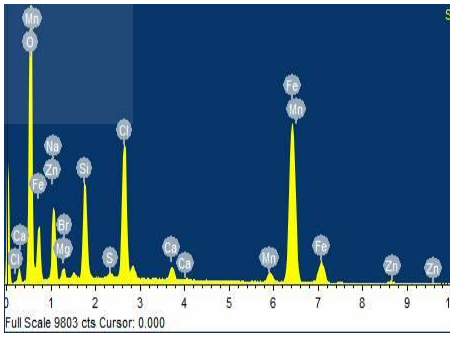

Figure 61: Microstructure characterization of mild steel without corrosion film (after corrosion film was removed); (a) Surface profile (thickness); (b) Material detachment on the surface – having 327.600 ± 23.190 nm average surface roughness; (c) 3D SEM/EDX image; (d) Elemental composition of the corroded surface.